Proceedings of the Eighteenth EGS Users' Meeting in Japan

August 9 - 11, 2011.
KEK, Tsukuba, Japan

Edited by

Y. Namito, H. Hirayama and S. Ban

High Energy Accelerator Research Organization

FOREWARD

The Eighteenth EGS Users' Meeting in Japan was held at High Energy Accelerator Research Organization (KEK) from August 9 to 11. The meeting has been hosted by the Radiation Science Center. More than 100 participants attended the meeting.

The meeting was divided into two parts. Short course on EGS was held at the first half of the workshop using EGS5 code. In the later half, 14 talks related EGS were presented. The talk covered the wide fields, like the medical application and the calculation of various detector responses *etc*. These talks were very useful to exchange the information between the researchers in the different fields.

Finally, we would like to express our great appreciation to all authors who have prepared manuscript quickly for the publication of this proceedings.

Hideo Hirayama
Yoshihito Namito
Syuichi Ban
Radiation Science Center
KEK, High Energy Accelerator Research Organization

CONTENTS

Numerical calculation of the Goudsmit-Saunderson multiple scattering angular distribution 2: Comparison with the small angle approximation

K. Okei[†] and T. Nakatsuka[‡]

[†]*Kawasaki Medical School, Kurashiki 701-0192, Japan*
[‡]*Okayama Shoka University, Okayama 700-8601, Japan*

Abstract

The small angle approximation of the Goudsmit-Saunderson multiple scattering angular distribution has been studied. It was found that the relative error of the small angle approximation is less than 1 % for scattering angles less than about 0.03 radian and the approximation would provide faster computation of the multiple scattering distribution without significant loss of accuracy.

1 Introduction

The theories of Goudsmit-Saunderson [1, 2] and of Lewis [3] give accurate multiple scattering distributions of charged particles passing through matter. However in their theories, the multiple scattering angular distribution $f_{\mathrm{GS}}(\theta)$ has the form of a Legendre series

$$f_{\mathrm{GS}}(\theta) = \frac{1}{2\pi}\sum_{l=0}^{\infty}(l+\tfrac{1}{2})\exp\left[-\frac{t}{\lambda}\left\{1 - \int_0^{\pi} 2\pi\sin\theta f_1(\theta)P_l(\cos\theta)\,\mathrm{d}\theta\right\}\right]P_l(\cos\theta), \qquad (1)$$

and its computation can require thousands of terms to converge (here f_1 is the single scattering cross section and t/λ is the mean number of deflections).

Hence, we have been studying methods for accelerating the numerical computation of the Goudsmit-Saunderson multiple scattering angular distribution. In the seventeenth EGS meeting, we reported that the convergence of the Legendre series can be accelerated with the transformation proposed by Yennie, Ravenhall and Wilson [4, 5]. Although the transformation is efficient for oscillating sequences, it is not effective for high energy particles which are not deflected very much by Coulomb scattering since $P_l(\cos\theta)$ remains almost unity up to very large l for $\theta \ll 1$. On the other hand, in cases where the small angle approximation is appropriate, the multiple scattering angular distribution $f_{\mathrm{SA}}(\theta)$ can be obtained by integration and be computed quicker. Therefore, in this work, we compare f_{GS} and f_{SA} and evaluate the error due to the small angle approximation.

2 Multiple scattering distribution

In the Goudsmit-Saunderson theory, the multiple scattering angular distribution $f_{\mathrm{GS}}(\theta)$ after a path length t is described as

$$\begin{aligned}
f_{\mathrm{GS}}(\theta) &= \frac{1}{2\pi}\sum_{l=0}^{\infty}(l+\tfrac{1}{2})\exp\left[-\frac{t}{\lambda}\left\{1 - \int_0^{\pi} 2\pi\sin\theta f_1(\theta)P_l(\cos\theta)\mathrm{d}\theta\right\}\right]P_l(\cos\theta) \\
&= \frac{1}{2\pi}\sum_{l=0}^{\infty}(l+\tfrac{1}{2})\exp\left[-\frac{t}{\lambda}\left\{1 - F_l\right\}\right]P_l(\cos\theta) \\
&= \frac{1}{2\pi}\sum_{l=0}^{\infty}(l+\tfrac{1}{2})\exp\left[-\frac{t}{\lambda}g_l\right]P_l(\cos\theta)
\end{aligned} \qquad (2)$$

where λ is the mean free path, $f_1(\theta)$ is the single scattering angular distribution and P_l are the Legendre polynomials.

To test the numerical computation, we use the screened Rutherford cross section and f_1, F_l can be written as

$$2\pi f_1(\theta) = \frac{\chi_a^2(\chi_a^2+4)}{8}\bigg/ 4\left(\sin^2\frac{\theta}{2}+\frac{\chi_a^2}{4}\right)^2 = \frac{\chi_a^2(\chi_a^2+4)}{8}\bigg/\left(1-\cos\theta+\frac{\chi_a^2}{2}\right)^2 \tag{3}$$

$$F_l = \frac{\chi_a^2(\chi_a^2+4)}{8}\frac{1}{2}\left(\frac{\chi_a^2}{4}\right)^{-l-2}\frac{\Gamma(l+1)\Gamma(l+2)}{\Gamma(2l+2)}{}_2F_1\left(l+1,l+2;2l+2;-\left(\frac{\chi_a^2}{4}\right)^{-1}\right). \tag{4}$$

Here χ_a is the screening angle [6, 7, 8] and ${}_2F_1$ is the hypergeometric function [3]. The Legendre coefficient F_l calculated from equation (4) is shown in figure 1 for $\chi_a = 10^{-1}, 10^{-2}, 10^{-3}$ and 10^{-4} and figure 2 shows the screening angle χ_a as a function of electron energy for water, iron and lead. From these figures, it can be seen that $F_l \simeq 1$ ($g_l \simeq 0$ and $\exp(-\frac{t}{\lambda}g_l) \simeq 1$) up to large l for high energy electrons and many terms are required for the series (2) to converge.
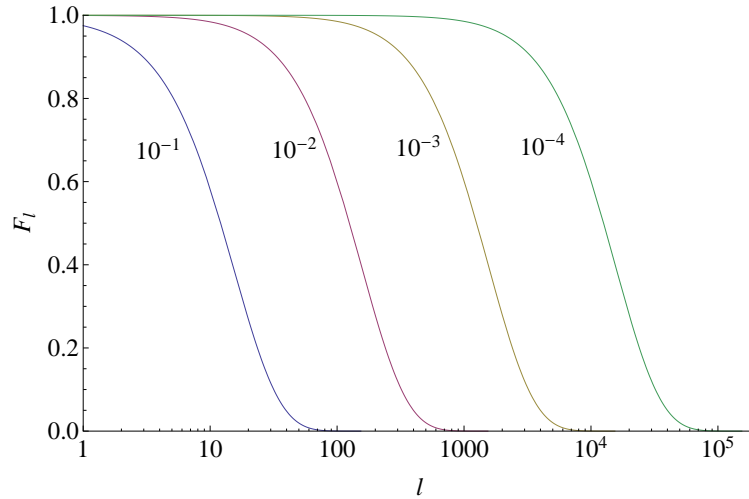

Figure 1: The Legendre coefficient F_l calculated from equation (4) for $\chi_a = 10^{-1}, 10^{-2}, 10^{-3}$ and 10^{-4}.
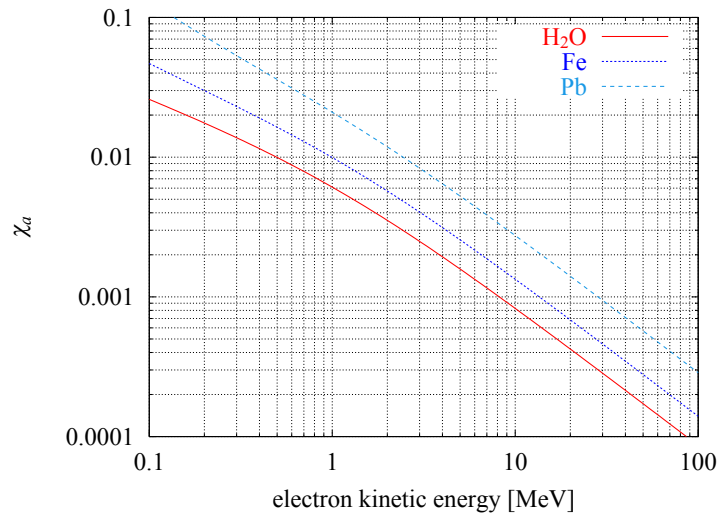

Figure 2: The screening angle χ_a as a function of electron energy for water, iron and lead.

2

3 Small angle approximation

For small θ, $P_l(\cos\theta)$ can be approximated by $P_l(\cos\theta) \approx J_0[(l + \frac{1}{2})\theta]$ (or $\sqrt{\theta/\sin\theta}\,J_0[(l + \frac{1}{2})\theta]$) and the Euler-Maclaurin formula

$$\sum_{l=0}^{\infty} f(l + \tfrac{1}{2}) = \int_0^{\infty} f(x)\,\mathrm{d}x + \frac{1}{24}f'(0) + \cdots \tag{5}$$

gives the small angle approximation of $f_{\mathrm{GS}}(\theta)$,

$$f_{\mathrm{SA}}(\theta) = \frac{1}{2\pi}\sqrt{\theta/\sin\theta}\int_0^{\infty}\eta\exp\left[-\frac{t}{\lambda}\left\{1 - \int_0^{\infty}2\pi\theta f_1(\theta)J_0(\eta\theta)\,\mathrm{d}\theta\right\}\right]J_0(\eta\theta)\,\mathrm{d}\eta \tag{6}$$

where $\eta = l + \frac{1}{2}$ [6, 3, 8, 9] and equations (3) and (4) respectively reduce to

$$2\pi f_1(\theta) = \frac{2\chi_a^2}{(\theta^2 + \chi_a^2)^2} \tag{7}$$

$$\int_0^{\infty}2\pi\theta f_1(\theta)J_0(\eta\theta)\mathrm{d}\theta = \eta\chi_a K_1(\eta\chi_a) \tag{8}$$

where K_1 is the first order modified Bessel function of second kind. Figure 3 shows the absolute relative difference between $\eta\chi_a K_1(\eta\chi_a)$ and F_l as a function of l for $\chi_a = 10^{-1}, 10^{-2}$ and 10^{-3}. The difference is less than one percent for $\chi_a < 0.1$.
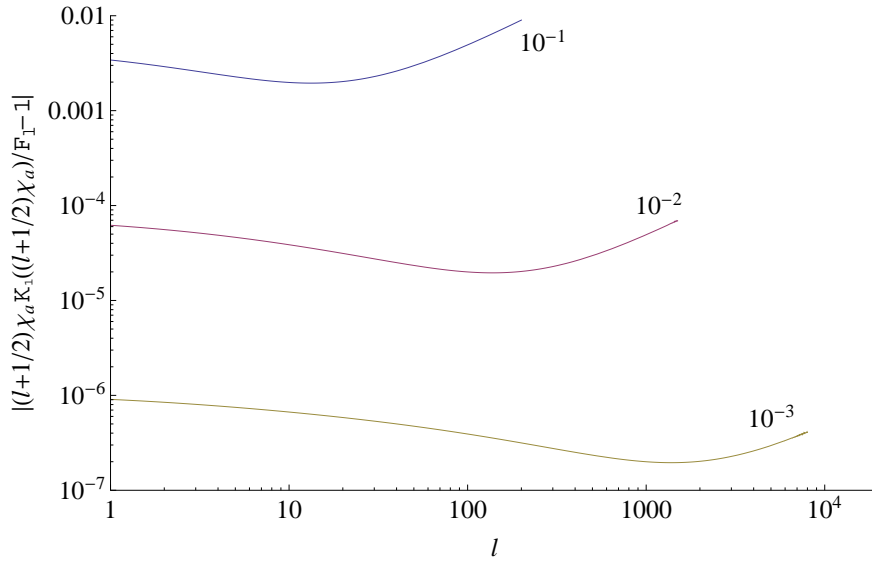

Figure 3: The absolute relative difference between $\eta\chi_a K_1(\eta\chi_a)$ and F_l as a function of l for $\chi_a = 10^{-1}, 10^{-2}$ and 10^{-3}.

3

4 Comparison of f_{SA} and f_{GS}

In this section, we compare f_{SA} and f_{GS} for several conditions to quantify the accuracy of the small angle approximation. For the numerical integration of f_{SA}, we used the double exponential (DE) formula [10, 11, 12] as refs [5, 13]. In the calculation of f_{GS}, we set the maximum number of iterations to be 3000 and the convergence of the series was determined by requiring that the contribution of additional term is less than $\varepsilon = 10^{-8}$ of the sum in magnitude for two consecutive terms. (We observed that the use of $\varepsilon = 10^{-6}$ sometimes resulted in false convergence.)

Figure 4 shows f_{SA} (open circle) and f_{GS} (cross) calculated for $t/\lambda = 1000$ and $\chi_a = 10^{-4}$. In this case, the RMS angle $\sqrt{E(\theta^2)}$ of the central Gaussian region of the distribution is about 0.01. (Here $E(\cdot)$ stands for the expectation operator.) The two distributions agree well except for the region where $\theta \gtrsim 1$. The relative errors of f_{SA} for $\sqrt{E(\theta^2)} \sim 0.1$ ($t/\lambda = 1000$ and $\chi_a = 10^{-3}$) and $\sqrt{E(\theta^2)} \sim 0.01$ ($t/\lambda = 1000$ and $\chi_a = 10^{-4}$) are shown in figure 5. Figure 6 compares the relative errors for the same RMS angle $\sqrt{E(\theta^2)} \sim 0.1$ but different path lengths and electron energies (i.e. different t/λ and χ_a).

These figures show that the relative error of f_{SA} is less than 1 % (10 %) for $\theta \lesssim 0.03$ ($\theta \lesssim 0.1$) and the error in the region $\theta \gtrsim 0.1$ almost depends on θ only.
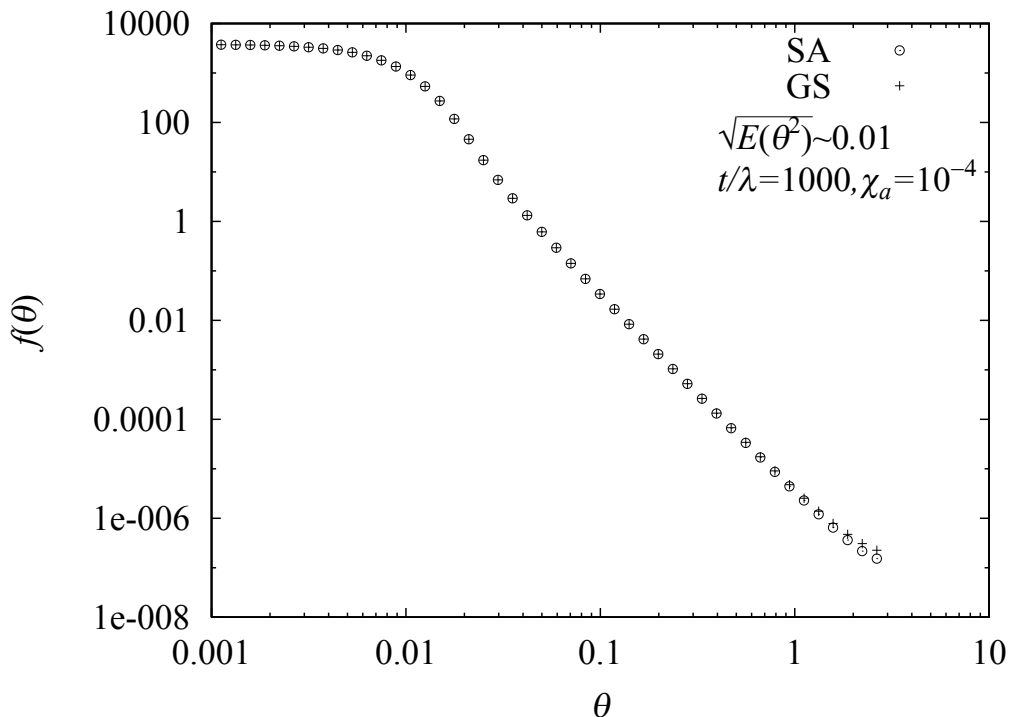
Figure 4: The multiple scattering angular distribution f_{SA} (open circle) and f_{GS} (cross) for $t/\lambda = 1000$ and $\chi_a = 10^{-4}$.
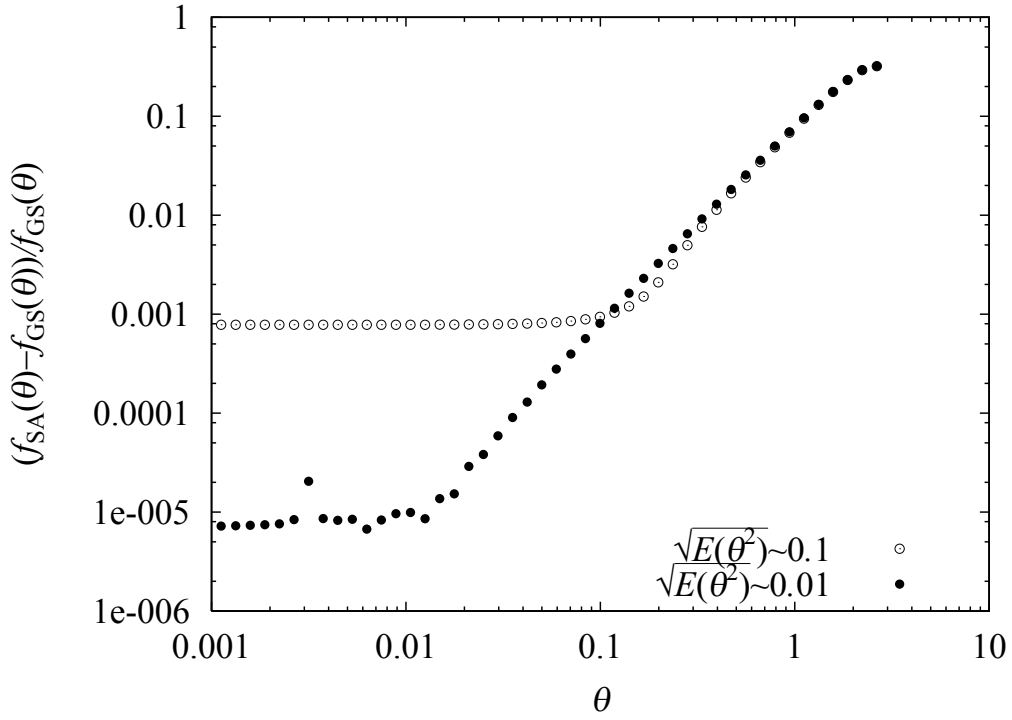
Figure 5: The relative error of f_{SA} for $\sqrt{E(\theta^2)} \sim 0.1$ ($t/\lambda = 1000$ and $\chi_a = 10^{-3}$, open circle) and $\sqrt{E(\theta^2)} \sim 0.01$ ($t/\lambda = 1000$ and $\chi_a = 10^{-4}$, solid circle).
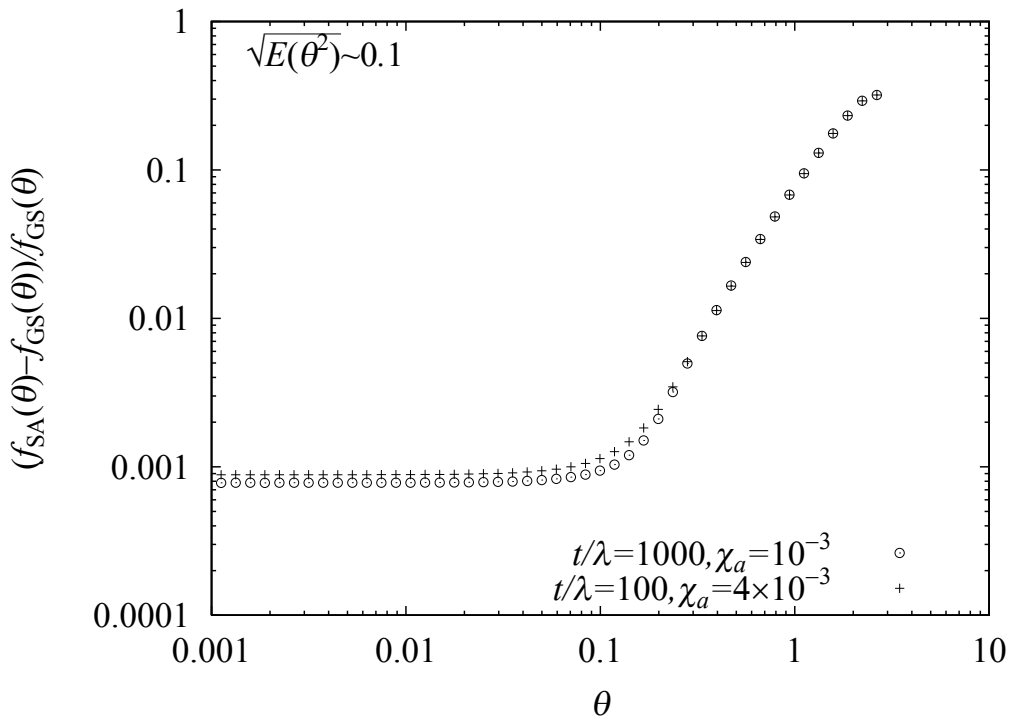
Figure 6: The relative error of f_{SA} for $\sqrt{E(\theta^2)} \sim 0.1$. open circle: $t/\lambda = 1000$ and $\chi_a = 10^{-3}$, cross: $t/\lambda = 100$ and $\chi_a = 4 \times 10^{-3}$.

5 Conclusion

We have studied the small angle approximation of the Goudsmit-Saunderson multiple scattering angular distribution. It was found that the relative error of the small angle approximation is less than 1 % for $\theta \lesssim 0.03$. Furthermore, f_{SA} can be computed relatively fast by using a sophisticated numerical integration method, such as DE method. Therefore the small angle approximation would provide faster computation of the multiple scattering distribution without significant loss of accuracy.

References

[1] S. Goudsmit and J. L. Saunderson, *Phys. Rev.* **57**, 24 (1940)

[2] S. Goudsmit and J. L. Saunderson, *Phys. Rev.* **58**, 36 (1940)

[3] H. W. Lewis, *Phys. Rev.* **78**, 526 (1950)

[4] D. R. Yennie, D. G. Ravenhall and R. N. Wilson, *Phys. Rev.* **95**, 500 (1954)

[5] K. Okei and T. Nakatsuka, *Proc. 17th EGS Users' Meeting in Japan*, KEK Proceedings 2010-9, 1 (2010).

[6] G. Molière, *Z. Naturforsch.* **2a**, 133 (1947).

[7] G. Molière, *Z. Naturforsch.* **3a**, 78 (1948).

[8] H.A. Bethe, *Phys. Rev.* **89**, 1256 (1953).

[9] W. T. Scott, *Rev. Mod. Phys.* **35**, 231 (1963).

[10] T.Ooura and M.Mori, *Journal of Computational and Applied Mathematics* **38**, 353 (1991).

[11] T.Ooura and M.Mori, *Journal of Computational and Applied Mathematics* **112**, 229 (1999).

[12] M. Mori and M. Sugihara, *Journal of Computational and Applied Mathematics* **127**, 287 (2001).

[13] K. Okei and T. Nakatsuka, *Proc. 13th EGS Users' Meeting in Japan*, KEK Proceedings 2006-4, 28 (2006).

EFFECTS OF SCATTERING ON THE RECONSTRUCTION OF DUAL-ENERGY X-RAY CT

Kenta Tokumoto, Yoichi Yamazaki, Naohiro Toda

Information and Computer Sciences, Aichi Prefectural University

Abstract

We analyze the influence of scattered radiation on the dual energy(DE) method in X-ray computed tomography(CT) by carrying out a Monte Carlo simulation implemented in EGS5. In principle, the DE method can extract the energy dependency of the attenuation coefficient of the object and avoid the effect of beam hardening. However, the effects of scattered radiation on DE reconstruction have not been investigated thus far. In this study, we show that scattered radiation may produce large artifacts in the DE reconstructed image when a cone beam geometry is used.

1 Introduction

X-ray computed tomography (CT) has been enhanced in many ways since its invention in the early 1970s, and today, it is indispensable in medical treatments[1, 2]. Standard medical CT devices (or scanners) use an X-ray tube that radiates polychromatic X-rays with spectral energy in the range of 10 to 200 keV. Within this energy range, the linear attenuation coefficients of common substances decrease with increasing energy. This tendency varies among the substances; hence, each substance has its own characteristic color. The extraction of this energy-dependent nature of an object in the reconstruction process may be beneficial to medical diagnoses. Standard CT devices reconstruct tomographical images under the assumption that polychromatic X-rays can be approximated by monochromatic X-rays with a single effective energy; hence, these devices disregard the energy-dependent information about the objects.

Alvarez et al.[3] found that the linear attenuation coefficient of a common substance can be approximated by the linear combination of the photoelectric effect and Compton scattering. Accordingly, they proposed the extraction of information on the energy characteristics by carrying out measurements using two X-ray beams with different spectra. This method is called the dual-energy (DE) method. The DE method does not require any prior knowledge of the object in the scan field, and it can be used to estimate the attenuation coefficient of unknown materials. Further, the images reconstructed by the DE method are, in principle, free from beam-hardening artifacts.

However, the DE method has not been adopted in clinical CT examinations because the influence of scattered radiation in cone beams has not been investigated thus far. Because of the growing popularity of cone beam CT, in this paper, we investigate the effects of scattered radiation on DECT reconstruction using a Monte Carlo simulation implemented in EGS5.

2 Method

2.1 The Dual-Energy Principle

The spatial distribution of the linear attenuation coefficients at an energy ε [keV] in the cross section of the object can be written as a function of these variables, namely $\mu(\boldsymbol{x}, \varepsilon)$. Here, $\boldsymbol{x}$ denotes a position vector in a three-dimensional objective space. At a scanning position τ, the measured intensity of the X-rays that have passed directly through the object is modeled as

$$I_m(\tau) = \int_{\varepsilon_\ell}^{\varepsilon_\ell} I_e(\tau, \varepsilon) \exp\left(-s(\tau, \varepsilon)\right) d\varepsilon, \tag{1}$$

where ε_ℓ (> 0) and ε_u ($> \varepsilon_\ell$) are the minimum and maximum energies, respectively. $I_e(\tau, \varepsilon)$ is a positive bounded function that denotes the intensity of the emitted X-rays, including the effects of filters and the energy dependency of detectors. $s(\tau, \varepsilon)$ is a projection that is given by a line integral

$$s(\tau, \varepsilon) = \int_{\mathcal{L}_\tau} \mu(\boldsymbol{x}, \varepsilon) d\ell, \tag{2}$$

where $\mathcal{L}_\tau$ denotes a projection line whose ends lie at the X-ray source and the detector at a scanning position τ.

The reconstruction problem of CT is to determine $\mu(\boldsymbol{x}, \varepsilon)$ from a given set of measured $I_m(\tau)$. (1) and (2) result in a nonlinear integral equation, which is solved by standard CT devices via brute force, i.e., by assuming that polychromatic X-rays can be approximated by monochromatic X-rays with an effective energy. However, this assumption not only ignores the energy-dependent information about the objects but also produces beam-hardening artifacts. Therefore, the extraction of energy-dependent information requires a different strategy.

Alvarez et al.[3] found that the energy-dependent linear attenuation coefficient $\mu(\varepsilon)$ of common substances can be expressed by a linear combination of two components,

$$\mu(\boldsymbol{x}, \varepsilon) = a_1(\boldsymbol{x}) X_1(\varepsilon) + a_2(\boldsymbol{x}) X_2(\varepsilon), \tag{3}$$

where $X_1(\varepsilon)$ and $X_2(\varepsilon)$ are basis functions representing the energy dependencies. If they are linearly independent of each other, an arbitrary function pair can be adopted. In this study, the functions of cross section of the photoelectric effect and Compton scattering are used as the basis function pair. Conventional CT is treated as a special case of (3) by imposing a restriction $X_1(\varepsilon) = 1.0$ and $a_2(\boldsymbol{x}) = 0$. Here, $X_1(\varepsilon)$ is assigned to the photoelectric effect as

$$X_1(\varepsilon) = \frac{1}{\varepsilon^3}, \tag{4}$$

and $X_2(\varepsilon)$ is assigned to Compton scattering according to the Klein-Nishina function as

$$X_2(\varepsilon) = \frac{1+\alpha}{\alpha^2} \left(\frac{2(1+\alpha)}{1+2\alpha} - \frac{1}{\alpha} \log(1+2\alpha) \right) + \frac{1}{2\alpha} \log(1+2\alpha) - \frac{1+3\alpha}{(1+2\alpha)^2}, \tag{5}$$

where $\alpha = \dfrac{\varepsilon}{510.975}$ [keV]. $a_1(\boldsymbol{x})$ denotes the pointwise coefficient of the photoelectric effect and $a_2(\boldsymbol{x})$ denotes that of Compton scattering. Alvarez et al.[3] showed that an adequate fitting technique can reduce the errors inherent in the approximation of (3) to less than 1%. This method is called the dual-energy (DE) method.

Substituting (3) into (2) yields

$$
\begin{aligned}
s(\tau, \varepsilon) &= \int_{\mathcal{L}_\tau} (a_1(\boldsymbol{x}) X_1(\varepsilon) + a_2(\boldsymbol{x}) X_2(\varepsilon)) d\ell \\
&= s_{a_1}(\tau) X_1(\varepsilon) + s_{a_2}(\tau) X_2(\varepsilon),
\end{aligned} \tag{6}
$$

where $s_{a_1}(\tau)$ and $s_{a_2}(\tau)$ are the projections of the components given by

$$s_{a_1}(\tau) = \int_{\mathcal{L}_\tau} a_1(\boldsymbol{x}) d\ell \quad \text{and} \quad s_{a_2}(\tau) = \int_{\mathcal{L}_\tau} a_2(\boldsymbol{x}) d\ell. \tag{7}$$

Using s_{a_1} and s_{a_2}, the measured intensity of the X-rays (1) becomes

$$
\begin{aligned}
I_m(\tau) &= \int_{\varepsilon_\ell}^{\varepsilon_u} I_e(\tau, \varepsilon) \exp\left(-s_{a_1}(\tau) X_1(\varepsilon) - s_{a_2}(\tau) X_2(\varepsilon) \right) d\varepsilon. \\
&= \int_{\varepsilon_\ell}^{\varepsilon_u} I_e(\tau, \varepsilon) \exp\left(-s(\tau, \varepsilon) \right) d\varepsilon.
\end{aligned} \tag{8}
$$

The unknown parameters in (8) are s_{a_1} and s_{a_2}; hence, we cannot solve it using data from a single measurement. However, by carrying out two measurements using X-rays with differing spectra, $^1I_e(\tau, \varepsilon)$ and $^2I_e(\tau, \varepsilon)$, we get

$$
\begin{cases}
{}^1I_m(\tau) = \displaystyle\int_{\varepsilon_\ell}^{\varepsilon_u} {}^1I_e(\tau, \varepsilon) \exp\left(-s(\tau, \varepsilon)\right) d\varepsilon \\[3mm]
{}^2I_m(\tau) = \displaystyle\int_{\varepsilon_\ell}^{\varepsilon_u} {}^2I_e(\tau, \varepsilon) \exp\left(-s(\tau, \varepsilon)\right) d\varepsilon,
\end{cases}
\tag{9}
$$

which is a simultaneous nonlinear equation. In principle, (9) can be solved numerically using iterative methods such as the Newton-Raphson method. In practice, however, the measured includes the quantum noise because of the limited amount of photons.

Here, we do not employ (9), but an alternative algorithm[4] that is based on the maximum likelihood, which exhibits good statistical stability. In this algorithm, the I-Divergence

$$
I = \sum_{\tau \in T} \int_{\varepsilon_\ell}^{\varepsilon_u} \left(p(\tau, \varepsilon) \log \frac{p(\tau, \varepsilon)}{q(\tau, \varepsilon)} - p(\tau, \varepsilon) + p(\tau, \varepsilon) \right) d\varepsilon
\tag{10}
$$

is minimized as a cost function, where T denotes the set of scanning positions. p and q are determined alternatively using the equations

$$
q(\tau, \varepsilon) = I_e(\tau, \varepsilon) \exp\left(-\sum_{i=1}^{2} \sum_{\boldsymbol{x} \in L(\tau)} a_i(\boldsymbol{x}) \xi(\tau, \boldsymbol{x}) X_i(\varepsilon) \right)
\tag{11}
$$

$$
p(\tau, \varepsilon) = q(\tau, \varepsilon) \frac{I_m(\tau)}{\displaystyle\int_{\varepsilon_\ell}^{\varepsilon_u} q(\tau, \varepsilon) d\varepsilon} ,
\tag{12}
$$

where $\xi(\tau, \boldsymbol{x})$ is a weighting function that indicates the length of the beam line inside the pixel. (11) and (12) are derived from a Poisson random variable.

The values of the combination coefficients are updated by

$$
a_i^{(k+1)}(\boldsymbol{x}) = a_i^{(k)}(\boldsymbol{x}) - \frac{1}{B_i(\boldsymbol{x})} \log\left(\frac{\tilde{b}_i(\boldsymbol{x})}{\hat{b}_i(\boldsymbol{x})} \right),
\tag{13}
$$

where $\tilde{b}_i(\boldsymbol{x})$ and $\hat{b}_i(\boldsymbol{x})$ are given by

$$
\tilde{b}_i(\boldsymbol{x}) = \sum_{\tau \in T} \int_{\varepsilon_\ell}^{\varepsilon_u} X_i(\varepsilon) \xi(\tau, \boldsymbol{x}) p(\tau, \varepsilon) d\varepsilon
\tag{14}
$$

$$
\hat{b}_i(\boldsymbol{x}) = \sum_{\tau \in T} \int_{\varepsilon_\ell}^{\varepsilon_u} X_i(\varepsilon) \xi(\tau, \boldsymbol{x}) q(\tau, \varepsilon) d\varepsilon.
\tag{15}
$$

Once the values of the combination coefficients a_i are determined by (13), $\mu(\boldsymbol{x}, \varepsilon)$ in (3) is obtained. Therefore, we can obtain the reconstructed tomographic image at an arbitrary energy.

2.2 Evaluation of Scattering using Monte Carlo Simulation

Because the algorithm mentioned in the previous section includes a model for statistical fluctuation of intensity, it exhibits good performance when few photons are detected. However, scattering is ignored in the algorithm.

In general, the number of scattered photons increases with increasing width of the X-ray beam. Recently, CT devices have been witnessing a transition from fan beam methods to cone beam

methods. Consequently, even if a new algorithm is employed, the existence of scattered radiation may hinder good DE reconstruction in cone beam CT. In order to determine this effect beforehand, we have to solve a radiative transport equation. In this study, we carry out a Monte Carlo simulation implemented in EGS5.

We set the geometry as shown in Figure 1. A virtual third-generation CT device is constructed. An X-ray tube and detectors are arranged such that they face each other, and they rotate around the iso-center simultaneously. The distance between the X-ray focus and the iso-center is 42[cm], which is equal to the distance between the detectors and the iso-center. The tube voltage is set to 140[kVp], and we extract two different spectrum-type X-ray beams by placing two absorption filters in front of the X-ray tube. One filter consists of a 1[mm]-thick layer of copper, and the other filter consists of 2[cm]-thick layer of aluminum and a 1[mm]-thick layer of copper. The spectra are shown in Figure 2. The X-ray tube radiates a cone beam whose fan angle and cone angle are 35[deg] and 5[deg], respectively, as shown in Figure 1. 512 NaI detectors are arranged along an arc of 35[deg] at equal intervals.
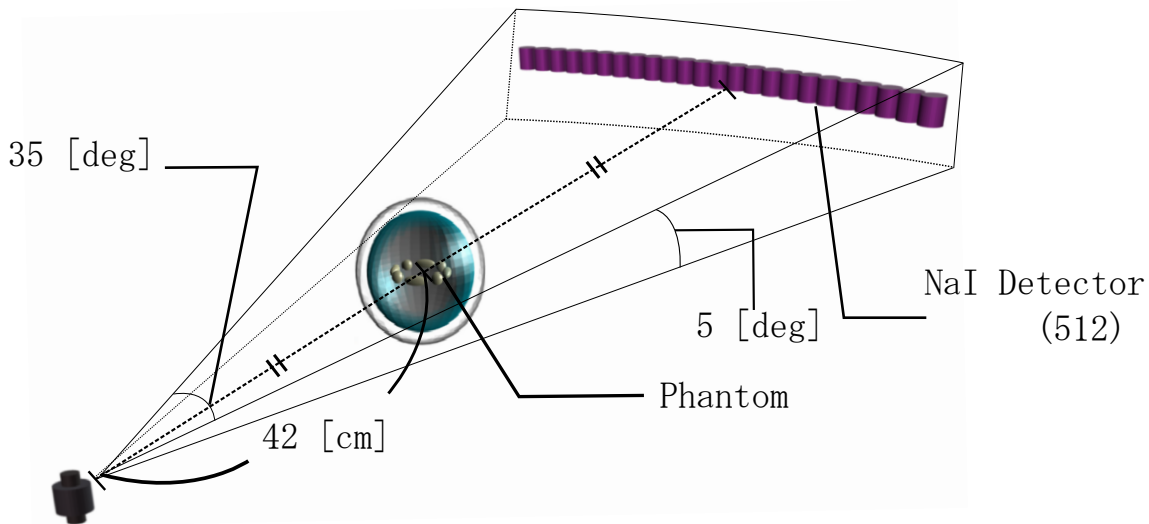

Figure 1: Geometry

The prepared phantom shown in Figure 3 is a sphere having a diameter of 24[cm]. The PMMA(acrylic) spherical shell that forms the outermost part of the phantom has a thickness of 2[cm], and the inside of the shell is filled with water. The ellipsoids having a major axis length of 4[cm] and spheres having a diameter of 2[cm] are composed of bone tissue, and they are arranged in the water.

The intensities of the X-ray projections are detected at every 1[deg]-rotation over a complete 360[deg] scan. For DE reconstruction, this scan is performed once for each X-ray spectrum. The number of photons that pass through an NaI detector is set to 10^7. We carry out a Monte Carlo simulation implemented in EGS5 on a parallel computer having 256 CPUs.

3 Results

3.1 Reconstructed Tomographic Image

In order to emphasize the influence of scattering, we prepare two sets of projection data: one includes scattered radiation, whereas the other does not. For each data set, tomographic images are reconstructed using conventional CT and the DE method.
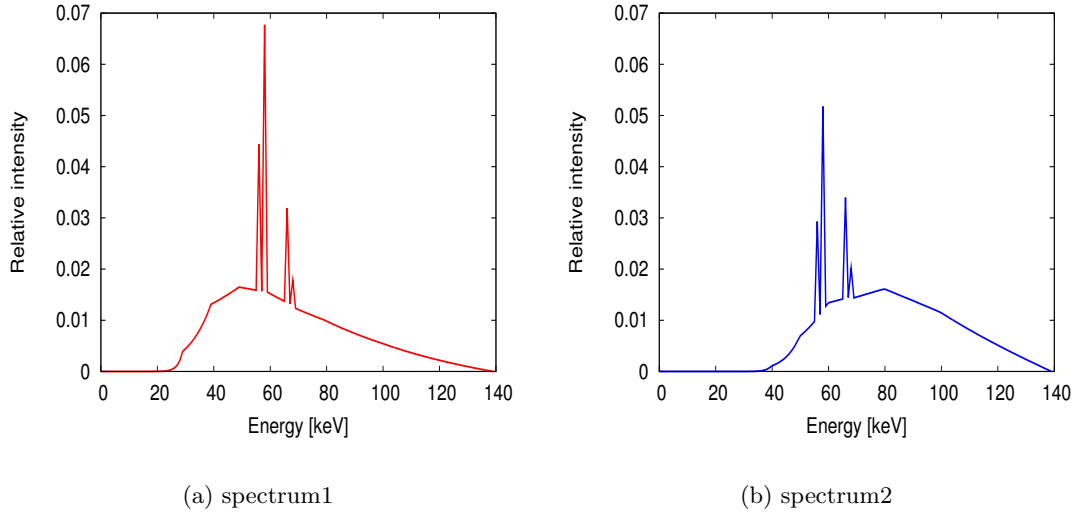
(a) spectrum1

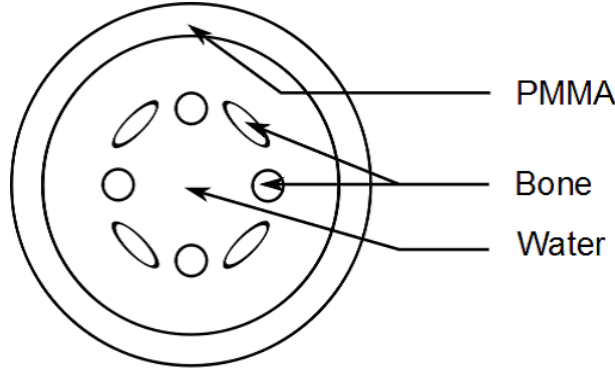(b) spectrum2

Figure 2: X-ray spectra

Figure 3: Component of phantom

Figure 4 shows the images at 87[keV] reconstructed by conventional CT (a) without scattering and (b) with scattering. Figure 5 shows the images also at 87[keV] reconstructed by the DE method (a) without scattering and (b) with scattering. In the case without scattering, few artifacts are recognized in the image(Figure 5(a)) reconstructed by the DE method, whereas artifacts appear around the center of the image (Figure 4(a)) reconstructed by conventional CT. We believe that these artifacts are beam-hardening artifacts. However, as shown in Figure 4(b) and Figure 5(b), in the case with scattered radiation, artifacts occur in both conventional CT and the DE method. In particular, the quality of reconstruction in the DE method is significantly influenced by scattering.

3.2   ErrorAnalysis

We evaluate the quality of the reconstructed images quantitatively. The root-mean-square error of tissue k ($k \in Ts = \{\text{water, bone, PMMA}\}$)
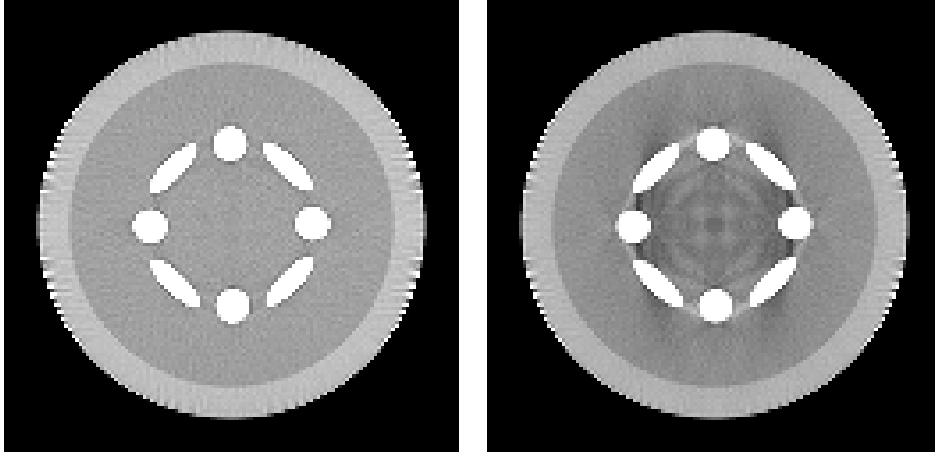
$$E_k(\varepsilon) = \sqrt{\frac{1}{N_k} \sum_{\boldsymbol{x} \in R_k} \left(\mu_k^*(\varepsilon) - \widehat{\mu}(\boldsymbol{x}, \varepsilon) \right)^2} \tag{16}$$

11
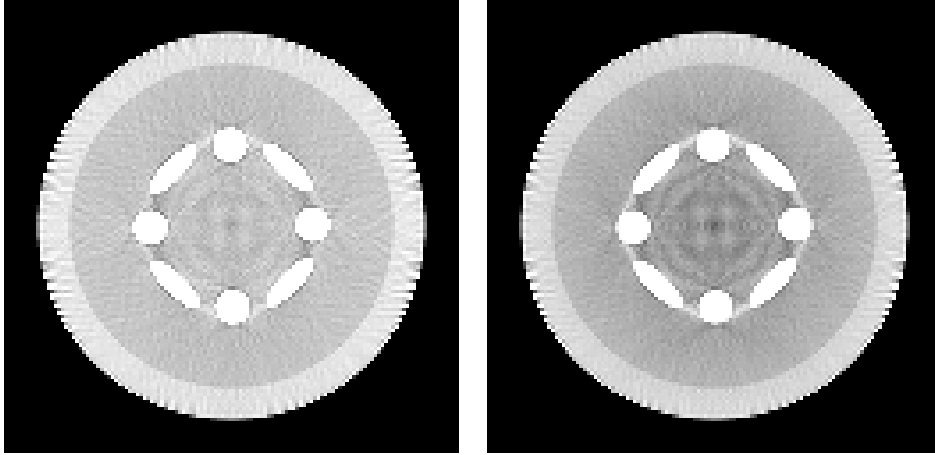
(a) without scattering   (b) with scattering

Figure 4: Images reconstructed by conventional CT

(a) without scattering   (b) with scattering

Figure 5: Images reconstructed by the DE method

and the error of the whole image

$$E_{whole}(\varepsilon) = \sqrt{\frac{1}{\sum_{k \in Ts} N_k} \left(\sum_{k \in Ts} N_k E_k^2(\varepsilon) \right)} \tag{17}$$

are employed as quality criteria, where, $\mu_k^*(\varepsilon)$ denotes the true attenuation coefficient of tissue k, $\widehat{\mu}(\boldsymbol{x}, \varepsilon)$ denotes the estimated attenuation coefficient at position $\boldsymbol{x}$, R_k denotes the region where the tissue k exists, except for the boundary, and N_k denotes the number of pixels in the region R_k.

Figure 6 shows these errors as functions of energy ε. Figure 6(a) shows the error of the whole image, given by equation(17), with and without scattering. Figure 6(b), (c), and (d) show the errors of the specific tissues, $E_{water}(\varepsilon)$, $E_{bone}(\varepsilon)$, and $E_{PMMA}(\varepsilon)$, respectively. From these figures, it is seen that the error increases when scattering exists.
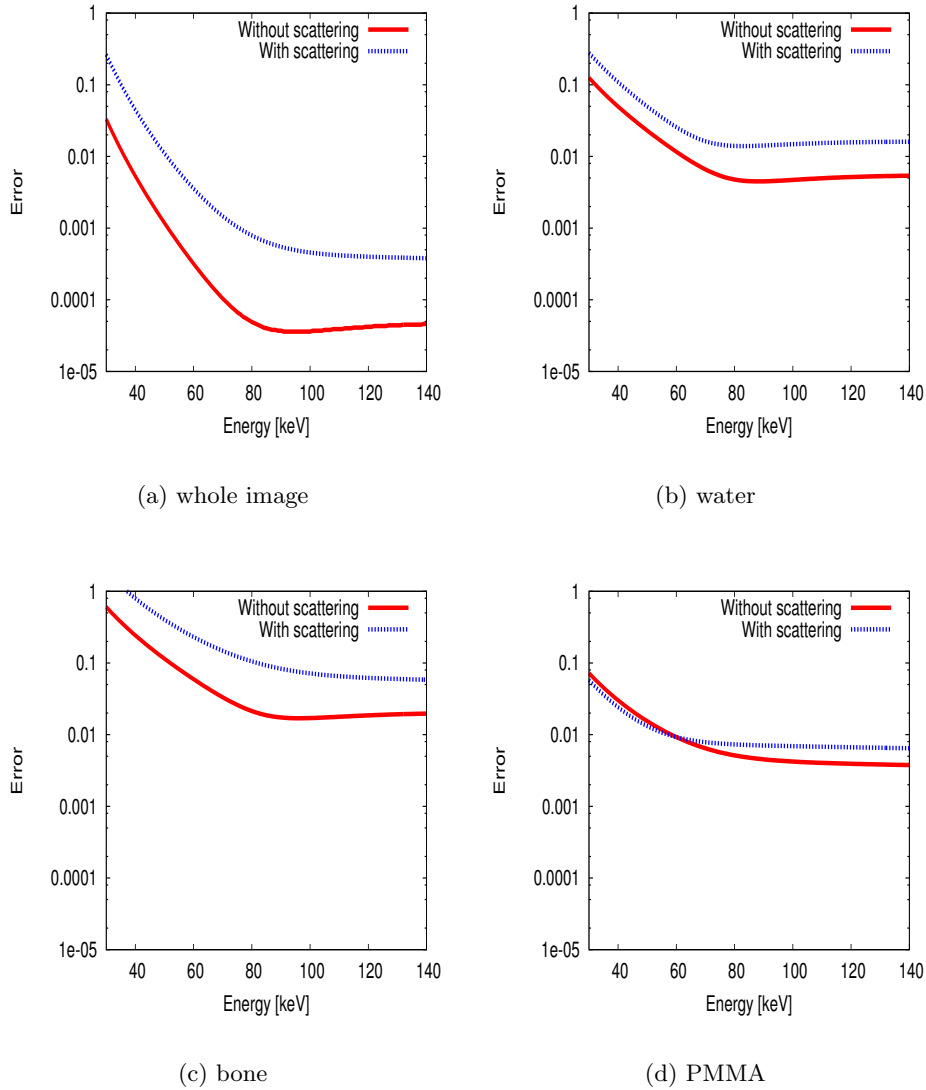
(a) whole image

(b) water

(c) bone

(d) PMMA

Figure 6: Root-mean-square errors of reconstructed images

3.3 Distributions of combination coefficients

We evaluate these reconstructions from the viewpoint of tissue characterization. In tissue characterization, a feature space is clustered. Because every substance has its own inherent position in the two-dimensional space(plain) of combination coefficients (a_1, a_2) of the basis functions, we assume that the feature space is selected to be this plain. In general, the estimated coefficients are distributed around the inherent position owing to the quantum noise or various types of artifacts. Smaller bias and variance in these distributions yield high clustering performance.

Figure 7 shows the distributions of the estimated combination coefficients; (a), (b), and (c) correspond to the regions R_{water}, R_{bone} and R_{PMMA}, respectively. The bold dots denote estimated combination coefficients in, the case without scattering, and the crosses denote the case with scattering.

In all the cases, it is found that the scattered radiation causes a large bias in the distribution. As mentioned above, this means that the presence of scattered radiation makes clustering difficult. Therefore, a method is required to eliminate the effect of scattering.
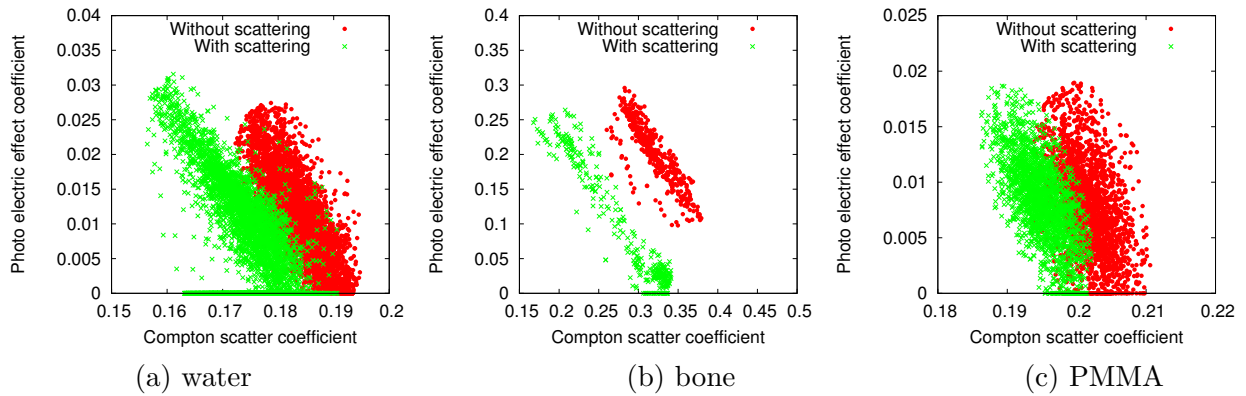
Figure 7: Distributions of coefficients

4　Conclusion

We analyzed the influence of scattered radiation on the DE method by carrying out a Monte Carlo simulation implemented in EGS5. The following problems were identified: (1) Scattered radiation produces large artifacts and errors in the reconstructed image. (2) In the presence of scattered radiation, large biases arise in estimating the combination coefficients of basis functions of energy dependency. Therefore, a method is required to overcome such problems caused by scattered radiation.

References

[1] Natterer, Frank and Ritman, Erik L., "Past and future directions in x-ray computed tomography (CT), " International Journal of Imaging Systems and Technology, Vol.12, No.4, pp.175–187,2002.

[2] J. Hsieh,"Computed Tomograph: Principles, Design, Artifacts and Recent Advances, " SPIE Press, Bellingham, 2003.

[3] R. E. Alvarez and A. Macovski, "Energy-selective reconstruction in X-ray computerized tomography, " Phys. Med. Biol., Vol.21, No.5, pp.733-744, 1976.

[4] J.A. O'Sullivan and J. Benac, Olternating minimization algorithms for transmission tomography," IEEE Trans. Medical Imaging, Vol.26, No.3, pp.283297, 2007.

Accuracy validation of dose evaluation for dual energy CT

D.Hayashi[1], S.Koyama[1]

[1]*Department of Radiological Technology, Graduate School of Medicine, Nagoya University*
1-1-20 Daikou-Minami, Higashi-ku, Nagoya, Japan
e-mail: hayashi.daiki@g.mbox.nagoya-u.ac.jp

Abstract

In dual energy computed tomography (DECT), computed tomography dose index (CTDI) is measured using same method as the measurement method of Single Energy CT (SECT) and used as reference of human dose. The purpose of this study is to calculate the CTDI and human dose in SECT and DECT using Monte Carlo simulation and to make comparison between the two relationships. The CTDI was calculated using cylindrical PMMA phantom (equivalent to the phantom for CTDI measurement) and human dose was calculated using cylindrical water phantom (equivalent to the human body) in the simulation. As a result, the relationship between the CTDI and the human dose in DECT was slightly different to that of SECT, and that the human dose in DECT was overestimated by 4.5%.

1. Introduction

Recently, dual energy computed tomography (DECT) is widely used in clinical practice. Single energy CT (SECT) uses single X-ray tube voltage (typically at 120 kV). DECT uses low and high x-ray tube voltages (typically at 80 and 140 kV, respectively). At present, computed tomography dose index (CTDI) for DECT is measured using same method as the measurement method of SECT and used as reference of human dose. It was thought that if the relationship between CTDI and human dose in DECT is different from that in SECT, human dose estimated by CTDI measured by traditional method is inadequate. The purpose of this study is to calculate CTDI and human dose in SECT and DECT using Monte Carlo simulation and to make comparison between those two relationships.

2. Materials and Methods

2.1 Overview

In this study, all simulations were performed using the Electron Gamma Shower ver.5 (EGS5) which is one of the Monte Carlo codes. In the simulation, we used geometric condition of a non-helical x-ray CT unit TCT-300 (Toshiba Medical Systems, Tochigi, JAPAN).

2.2 Simulation Geometry

Figure 1 shows simulation geometry. The x-ray fan beam angle was 38 degree and the slice thickness was 1cm. The source-isocenter distance was 60cm. The x-ray tube was rotated 360 degrees around the phantom at intervals of 1 degree. The x-ray tube voltages were 80kV, 120kV and 140kV. 120kV applied for SECT. 80kV and 140kV applied for DECT. Three incident energy spectra were calculated using Tucker's formula [1]. For fair comparison between SECT and DECT, each spectrum was calculated using same inherent filtration (=11.72 mmAl). In DECT, dose allocation

15

between 80kV and 140kV were must be decided. We thought that the photon number of 80kV and that of 140kV reaching CT detectors must be same to make good dual energy image. To equalize the photon number of 80kV and that of 140kV reaching CT detectors, the dose allocation was calculated using Monte Carlo simulation. As a result of the simulation, the dose allocation was 80kV:140kV=69.4%:30.6%.

Figure 2 shows phantom geometry. In the simulation, two cylindrical phantoms (32 cm in diameter and 15 cm thick) were used. One of these phantoms was made from polymethylmethacrylate (PMMA). PMMA phantom is equivalent to the phantom for CTDI measurement. There were five holes at center and peripheral (0°,90°,180°,270°) position in the PMMA phantom for CTDI measurement. Four peripheral holes were positioned at 1cm depths from the phantom surface. The four holes except for the hole as measurement region were filled by PMMA rods. Another phantom was made from water. We assumed that water phantom is equivalent to human body.

2.3 Calculation of absorbed dose

In the simulation, evaluation regions of two phantoms were 10cm long center hole and same long peripheral hole along the phantom axis. Imparted energy in the evaluation regions were deposited in unites of MeV in EGS5. Therefore, absorbed dose converted from imparted energy by

$$D = \frac{E \times 1.6 \times 10^{-13}}{V \times \rho} \quad (1)$$

where D (in Gy) was the absorbed dose. E (in MeV) was imparted energy which acquired in the simulation. V (in m^3) was the volume of measurement region. ρ was the density of water (in 1000 kg/m^3) or air (in 1.293 kg/m^3).

2.4 Validation the difference of relationship between CTDI and human dose between SECT and DECT

To calculate the relationship between CTDI and human dose, the absorbed dose ratio (R_{ad}) was defined as

$$R_{ad} = \frac{D_w}{D_p} \quad (2)$$

where D_W was absorbed dose in WATER phantom. D_P was absorbed dose in PMMA phantom. R_{ad} was calculated at five (center and four peripheral) positions for SECT and DECT, respectively. Human dose can be estimated by multiplying CTDI by R_{ad}.

3. Results

Figure 3 shows the comparison of R_{ad} between SECT and DECT at each position. In the center position, the R_{ad} of SECT (=1.414) was higher than one of DECT (=1.351). In the peripheral position, averages of R_{ad} for both CT were about the same (SECT's R_{ad}=1.367 DECT's R_{ad}=1.371).

We also investigated changes of R_{ad} due to varying the dose allocation of 80kV and 140kV for DECT. The dose allocation varied from 80kV:140kV=59.4%:40.6% to 80kV:140kV=79.4%:20.6% at intervals of 5%. **Figure 4 (a)** shows the changes of R_{ad} in the center position of the phantom. As the dose of 80kV increased, R_{ad} decreased from 1.362 to 1.331. **Figure 4 (b)** shows the changes of R_{ad} in the peripheral position of the phantom. As the dose of 80kV increased, R_{ad} increased slightly from 1.356 to 1.377.

4. Discussion

The results show that R_{ad} between SECT and DECT was slightly different in the center position of the cylindrical phantom. The R_{ad} of SECT (=1.414) was higher than that of DECT (=1.351). When human dose were estimated from R_{ad} of SECT, human dose in DECT was overestimated by 4.5%.

The results also show that the changes of R_{ad} in the center position of the cylindrical phantom were decreased with the dose of 80kV increased. In order to discuss the reason of this result, additional simulations were performed with variation of the incident x-ray tube energy every 10kV from 80kV to 140kV. The spectrum for each tube voltage was calculated using Tucker's formula [1] and using same inherent filtration (=11.72 mmAl). For more detailed discussion, the absorption dose was divided primary x-ray component and scattering x-ray component. The changes of absorbed dose in the water phantom are shown in **figure 5 (a)** and in the PMMA phantom are shown in **figure 5 (b)**. In the both phantoms, total absorbed dose was increased with an increase in the tube voltage and the scattering x-ray component contributed largely to the increase in absorbed dose. But the increasing range of the total absorption dose differed between water phantom and PMMA phantom. In the water phantom, the total absorbed dose varied from 3.29 (100%) to 4.74 (144%). As for the PMMA phantom, the total absorbed dose varied from 2.46 (100%) to 3.30 (134%). Thus, the changes of R_{ad} in **Figure 4 (a)** were caused by difference of the increasing range of absorbed dose from scatter x-ray component between water and PMMA phantom with an increase in the tube voltage.

5. Conclusions

In this study, we calculated the relationship between CTDI and human dose for SECT and DECT using Monte Carlo simulation and made comparison between the two relationships. As a result, the relationship of DECT was slightly different to the one of SECT. This study shows that human dose in DECT was overestimated by 4.5% when human dose were estimated from traditional CTDI evaluation method.

References

1) Douglas M. Tucker, Gary T. Barnes and Dev P. Chakraborty, Semiempirical model for generating tungsten target x-ray spectra, Med. Phys. 18, 211-218 (1991)
2) Baojun Li, Girijesh Yadava and Jiang Hsieh, Quantification of head and body $CTDI_{VOL}$ of dual-energy x-ray CT with fast-kVp swiching, Med. Phys. 38 2595-2601 (2011)
3) Lifeng Yu, Andrew N. Primak, Xin Liu, and Cynthia H. McCollough, Image quality optimization and evaluation of linearly mixed images in dual-source, dual-energy CT, Med. Phys. 36, 1019-1024 (2009)
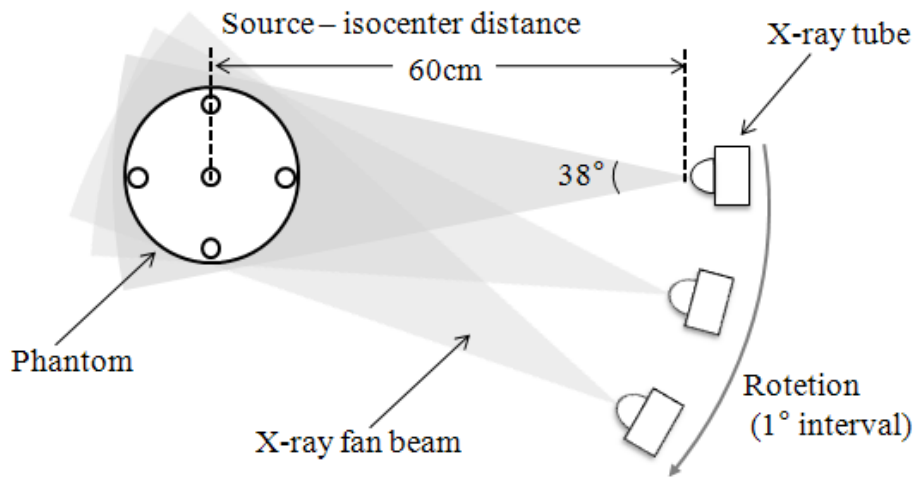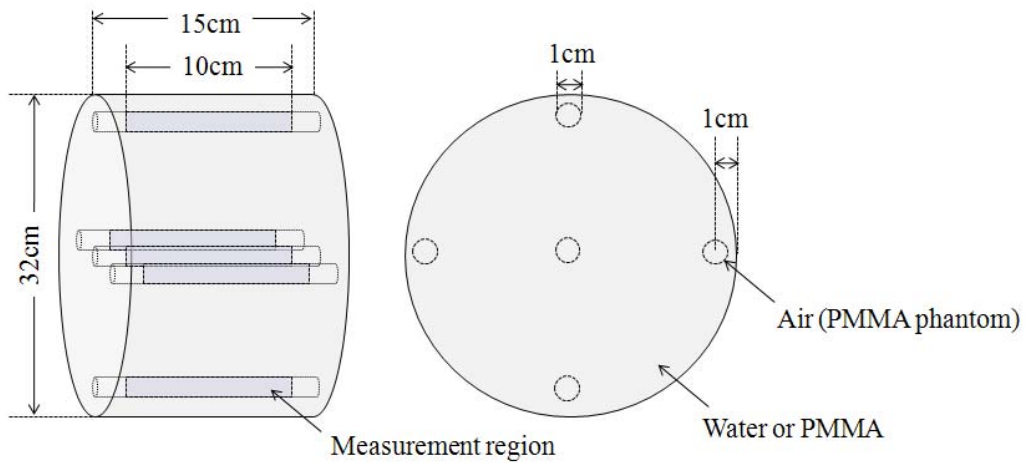
Figure 1. Simulation geometry

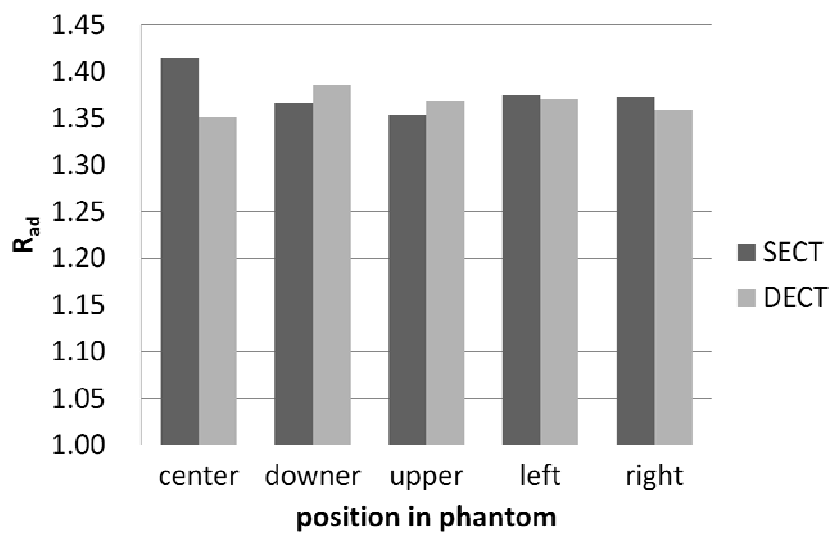**Figure 2.** Phantom geometry: In PMMA phantom, the four holes except for measurement region were filled for PMMA.

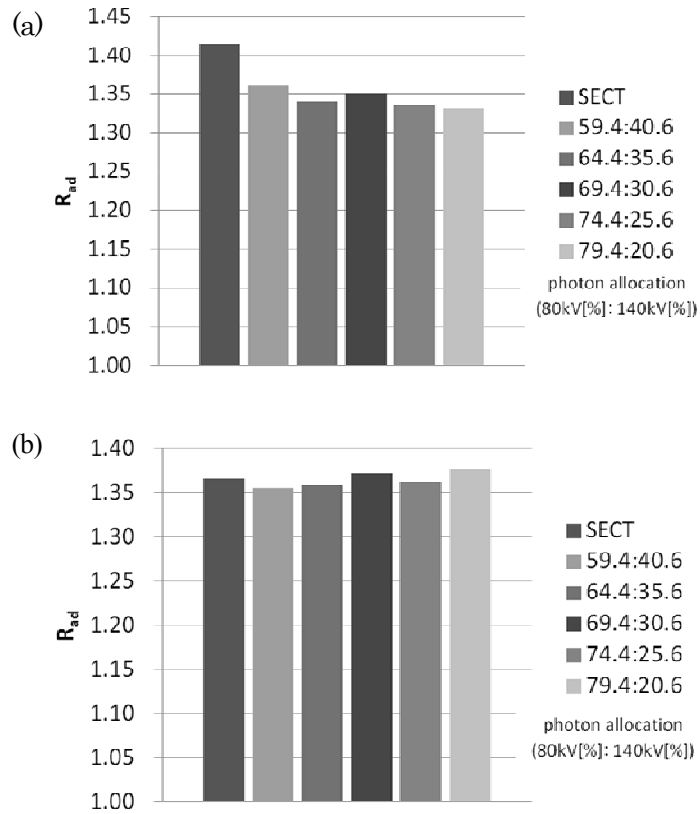**Figure 3.** Comparison of R_{ad} between SECT and DECT at each position in phantom

Figure 4. Changes of R_{ad} by a variance of dose allocation. (a) At center position in the phantom. (b) At peripheral position in the phantom.
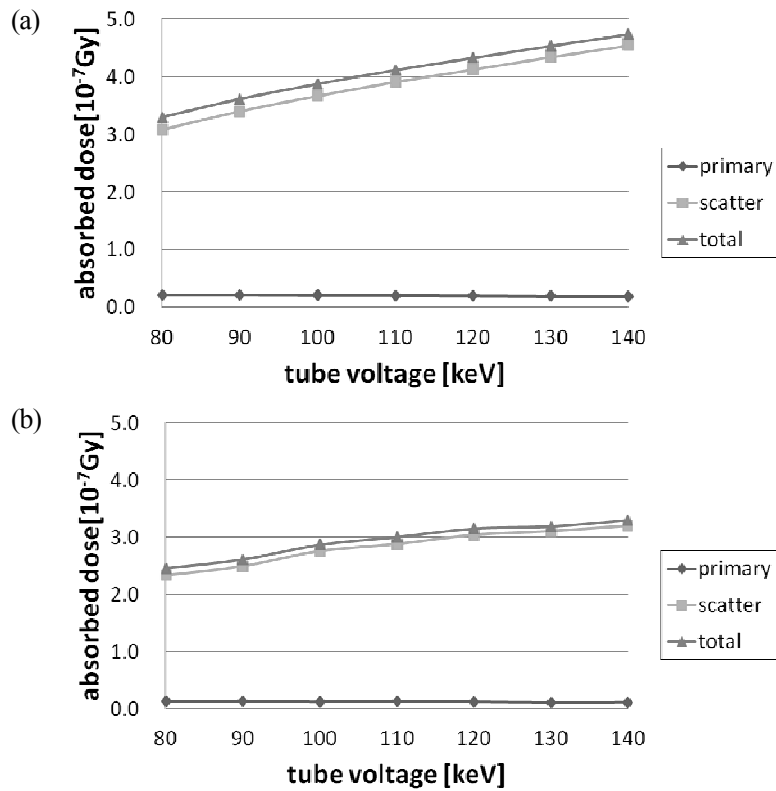

Figure 5. Changes of absorbed dose of the center of the phantom caused by variation of tube voltage. (a) Water phantom. (b) PMMA phantom.

A response study with combination of particle transport and optical transport calculation for scintillation detector

M. Hayashi[1], H. Nishizawa[1], H. Nakajima[1] and M. Nakanishi[2]

[1]*Advanced Technology R&D Center, Mitsubishi Electric Corporation, Hyogo, 661-8661, Japan*
[2]*Energy Systems Center, Mitsubishi Electric Corporation, Hyogo, 652-8555, Japan*
e-mail: Hayashi.Masateru@ct.MitsubishiElectric.co.jp

Abstract

The β ray responses for plastic scintillators have been studied by a combination of particle transport and optical transport calculations. The detector output corresponding to the deposit energy contains the light collection efficiency that depends on the scintillation point due to the geometrical shape. Additionally, the scintillation point changes along the particle tracks in the scintillator. We considered the positional dependency of the light collection efficiency within the particle transport calculation. We confirmed the validity of our present method with experimental measurements, and the simulation results reproduced measured detector responses.

1   Introduction

Plastic scintillators are widely used for β ray measurements, and their light output responses have been studied well [1]. However, the spectrums and absolute responses are difficult to estimate especially for large or light guide mounted ones, due to the complexity of the optical transport of scintillation lights.

Generally, the output charge of scintillators Q_{Tot} for an incident source particle is described

$$Q_{Tot} = \Delta E \times \epsilon \times F_{optical} \times f_Q \times G \times e, \tag{1}$$

where ΔE is the deposit energy to the scintillator, ϵ is the scintillation efficiency defined as the light production from the deposit energy, $F_{optical}$ is the light collection efficiency defined as the ratio of scintillation lights that enter the PMT (Photomultiplier tube) photo cathode to the produced scintillation lights, f_Q is the quantum efficiency of the PMT photo cathode, G is the PMT gain, and e is the elementary charge.

If there is no light attenuation inside the detector, or the light attenuation stays constant for any scintillation points, the detector output is proportional to the deposit energy. However, the light attenuation for each optical path is different, since the total path length and number of reflections are different for each optical path. Therefore, considering the positional dependency of the scintillation light collection is important for scintillator design, especially for a large scintillator. Several ways have been developed to evaluate scintillation light collection. Absolute scintillation photon yield and energy resolution for γ ray spectroscopy using NaI(Tl) scintillators has been studied [2], and scintillation light collection for cosmic ray muon measurement using large plastic scintillation fibers has also been studied [3]. In the present work, we developed a combined method of particle and optical transport calculation to analyze the β ray responses for plastic scintillators.

2   Combination of particle transport and optical transport calculations

A simplified model of the optical transport procedure for scintillators with light guide is illustrated in Fig. 1. The number of scintillation lights produced in the microscopic region is proportional to

the deposit energies in the microscopic region:

$$n = \Delta E \times \epsilon, \tag{2}$$

where ΔE is the deposit energies in the microscopic region and ϵ is the scintillation efficiency. Then the number of scintillation lights that enter the PMT photo cathode becomes

$$n' = \Delta E \times \epsilon \times F_{optical}, \tag{3}$$

where $F_{optical}$ is the light collection efficiency defined by Eq. 1.

The light collection efficiency depends on the light attenuation among the optical paths from the scintillation point to the PMT photo cathode. Two explanations are considered for the light attenuation: (1) self absorption (2) and leaks. The average optical path length and the average number of reflections are the same for identical scintillation points. However, since the scintillation points change along the incident electron track, the optical path length and the number of reflections depend on their geometrical situations. This effect is a strong contributor to the positional dependency for light collection efficiency.
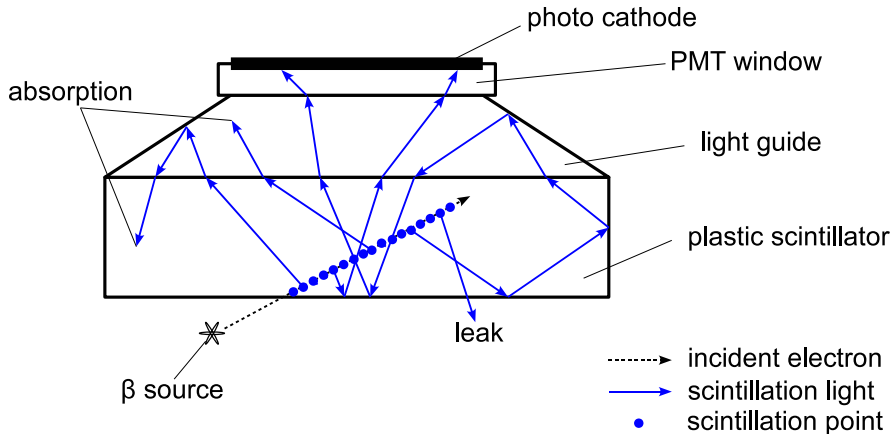

Figure 1: Simplified model of optical transport procedure for scintillators.

The reflective characteristic is also crucial for light collection efficiency. In most cases, the reflecting surfaces are considered specular or perfect diffusion. With a specular surface, the reflections resemble mirrors where the incidence and reflection angles are equal. On the other hand, with a diffuse surface, the reflection angles are independent of the incidence angle and follow Lambert's cosine law:

$$\frac{dI}{d\theta} \propto \cos\theta, \tag{4}$$

where I is the intensity of the reflected light and theta is the angle of the reflection with respect to normal reflection.

In standard EGS calculations, the deposit energy for an incident particle is expressed as a sum of the deposit energies for the microscopic regions with the particle tracks. However, the measured value corresponding to the deposit energy contains the positional dependency of the light collection efficiency discussed above. Therefore, the light collection efficiency is considered the weight for the deposit energies in the microscopic region:

$$M = \sum \Delta E \times \epsilon \times F_{optical}, \tag{5}$$

21

where ΔE is the deposit energy on the microscopic region, $F_{optical}$ is the light collection efficiency at the scintillation point that depends on the detector shape and such reflective characteristics of each component as light guide, reflection paint, and optical cement.

   The calculation procedure of the present method is illustrated in Fig. 2. First, we calculated the light collection efficiency on the grid of the XYZ mesh that covers the whole detector region using optical design software called ZEMAX® [4] with a non-sequential mode. The scintillation points change along with particle tracks ware calculated by EGS code, and the exact value of light collection efficiency corresponds to each scintillation point was calculated with interpolation techniques known as a tri-linear techniques and an inversed distance weighted techniques. In the present work, we have used 3 as a power parameter for the inversed distance weighted techniques.
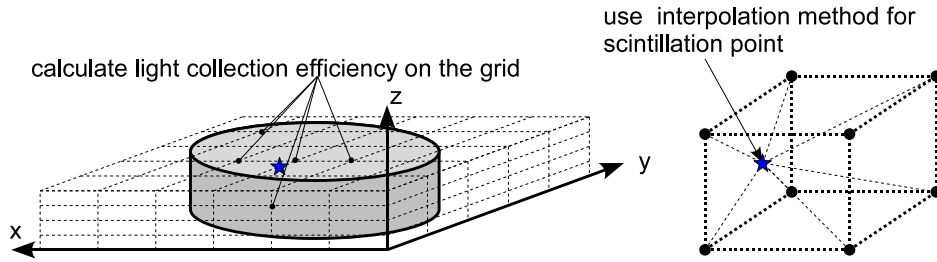

Figure 2: Calculation procedure of present method.

3   Results and discussion

To verify the optical transport calculation, we measured the positional dependence of the light correction efficiency. The experimental setup is illustrated in Fig. 3. The detector consists of a polyvinyl toluene-based plastic scintillator, a light guide, and a PMT. The plastic scintillator has a 100-mm diameter and is 1-mm thick. A light guide made of an ultraviolet transmissive type acrylic resin is tapered to a 46-mm diameter to match the size of the Hamamatsu R1847 photomultiplier tube. The reflective characteristics for the detector surface are shown in Table 1. To restrict the irradiation spots, we used a 1-mm diameter collimator, since in EGS5 analysis, the irradiation spots on the scintillator surface are restricted to less than a 2-mm diameter. The ^{90}Sr source, which was placed in the collimator, is a JRIA 301 type sealed radioactive source.
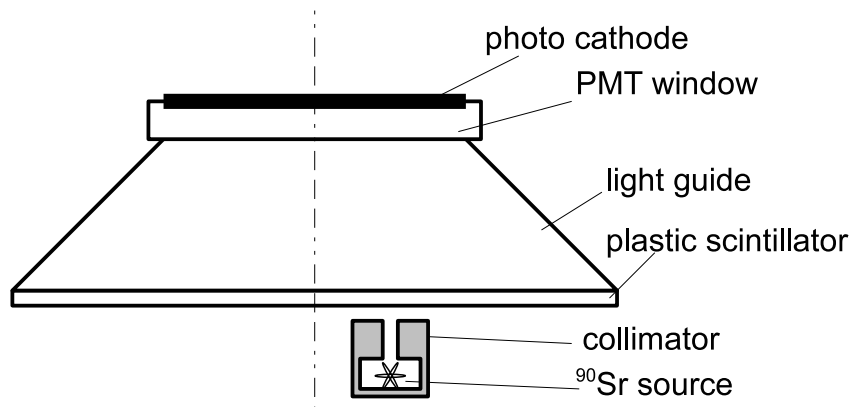

Figure 3: Experimental setup for verifying optical transport calculation.

Table 1: Reflective characteristics of detector surfacess

Surface	Material	Reflective characteristic
scinitllator surface	aluminum mylar foil	specular reflection
light guide	titanium-dioxide paint	diffuse reflection

The electrons from the ^{90}Sr β source pass through a 1-mm thick plastic scintillator, since the range of the ^{90}Sr$-^{90}$Y β ray (average energy is around 1 MeV) exceeds 1 mm. Then the deposit energy remains constant around 200 keV, which does not depend on the irradiation position. From Eq. 1, the detector output is proportional to the light correction efficiency, since ΔE is constant. This means the detector output is proportional to the light correction efficiency.

Figure 4 compares the measured positional dependence of the light collection and calculated efficiencies. The horizontal axis corresponds to the scintillation point, which is equivalent to irradiation position expressed as the distance from the scintillator center. The vertical axis corresponds to the light collection efficiency expressed as a ratio to the scintillator center position. The dot corresponds to the measured data, and the solid line corresponds to the optical transport calculation with diffuse reflection on the light guide. The dashed line corresponds to the optical transport calculation with a specular reflection surface on the light guide.

The measured light collection efficiencies decrease with the distance from the scintillator center to the irradiation position, due to the increasing of number of reflections and the optical path length. The positional dependency of the experimental light collection efficiencies is reproduced by the optical transport calculation with diffuse reflection. From the comparison between the two calculations, ZEMAX® can reproduce the difference of the reflective characteristics.
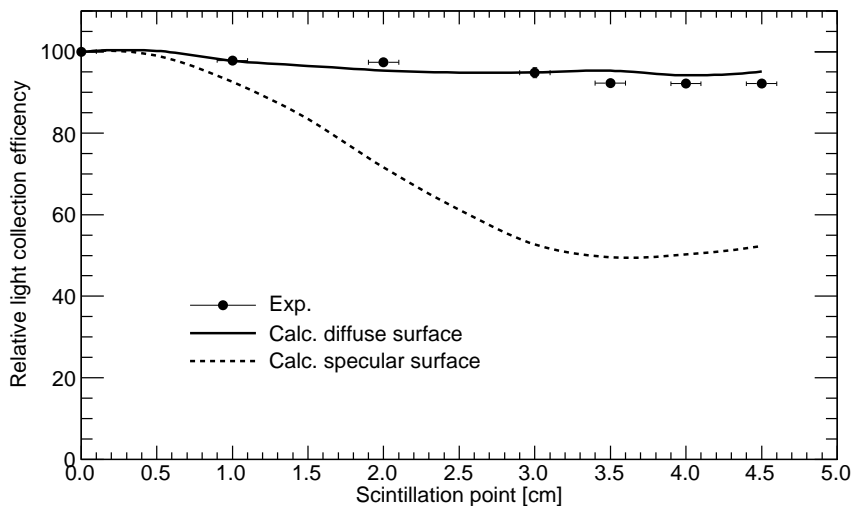

Figure 4: Comparison between measured positional dependence of light collection efficiencies.

Comparisons between the measured β ray spectra and the calculated ones for ^{90}Sr, ^{204}Tl, and ^{137}Cs are shown in Figs 5, 6, and 7, where the horizontal axis corresponds to the deposited energy to the scintillator, and the vertical axis corresponds to the β ray response from the plastic scintillator. The dots correspond to the measured data, the solid line corresponds to the calculation results with the combination method, and the dashed line corresponds to the calculation result without the combination method (only EGS). In the calculation, we considered the configuration of the

23

radioactive source, and the emitted electron energy spectrum from the radioactive nucleus was calculated by the approximation method [5].

In both cases, the spectrums with light collection efficiency were compressed to lower energy. This result reflected the positional dependence of the light collection efficiency shown in Fig. 4. The calculation results with the light collection efficiency were closer to the measured ones than without light collection efficiency, especially at the conversion electron peak of ^{137}Cs. Therefore the calculation results with light collection efficiency reproduced measured detector responses.

However, there are several differences between measured energy spectrums and calculated ones for both cases. This is considered as uncertainty of β energy spectrums. In the calculation, the exact thickness of thin aluminum window on radioactive source exit is not applied, since the window thickness is specified in the 1 to 5 mg/cm^2 range. Then the incident β energy spectrum is different between measurements and calculations.
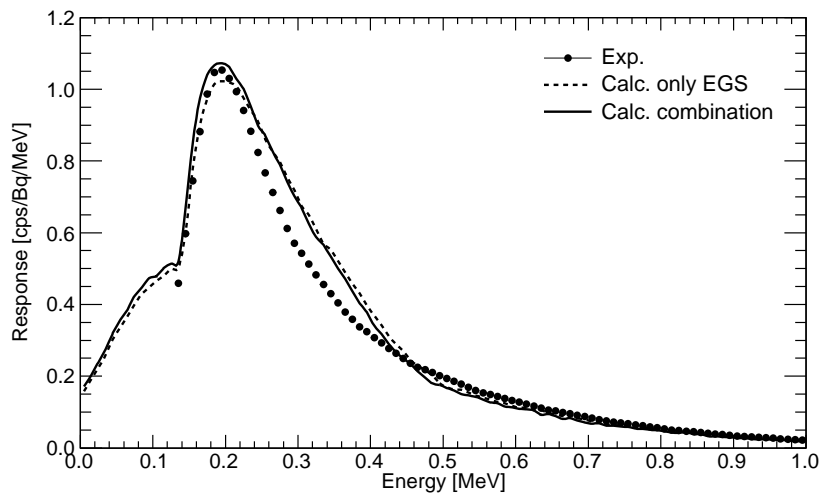

Figure 5: Comparison between measured ray spectra and calculated ones for ^{90}Sr source.
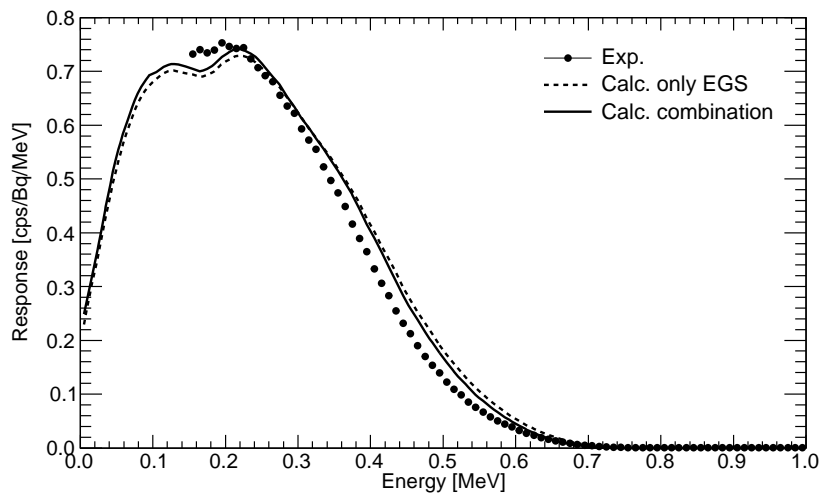

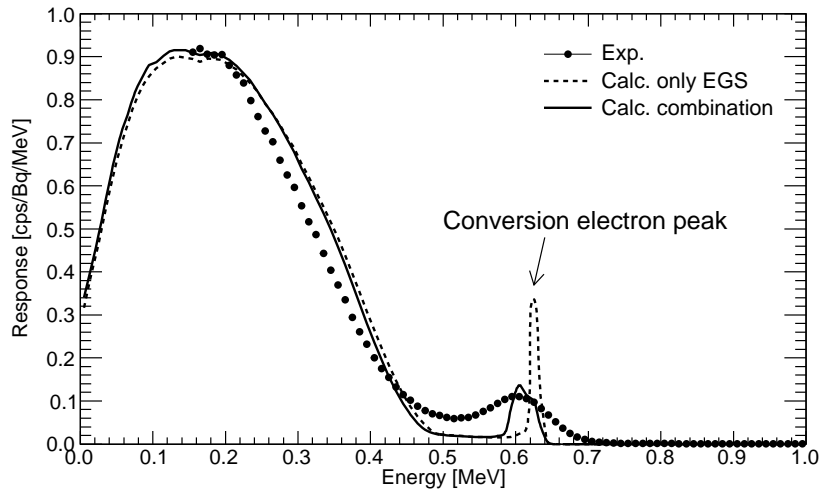Figure 6: Comparison between measured spectra and calculated ones for ^{204}Tl source.

Figure 7: Comparison between measured ray spectra and calculated ones for ^{137}Cs source.

4 Conclusions

The β ray responses for a plastic scintillator were analyzed by a combination of particle and optical transport calculations. A comparison between the measurements and simulations showed the following good agreement:

(1) The results of the optical transport calculation reproduced the measured positional dependency of the light collection efficiency.

(2) The calculation results with light collection efficiency quantitatively reproduced measured detector responses.

In the results, we have established the combined method of particle and optical transport calculation to analyze the β ray responses for large plastic scintillators which have a positional dependency of light collection efficiencies.

The present method will help analyze scintillator responses not only for plastic scintillators but also other inorganic scintillators with complicated light paths.

References

[1] W.R. Leo, ”Techniques for Nuclear and Particle Physics Experiments, Second Revised Edition”, Springer-Verlag, (1994).

[2] H. Tawara, S. Sakai, K. Saito, and E. Shibamura, ”A Monte-Carlo Method for Determining Absolute Scintillation-Photon Yields and Energy Resolution of Scintillators for GammaRays”, KEK Proceedings 2000-20, pp. 152-160, (2000).

[3] S. Riggi, P. LaRocca, E. Leonora, D. LoPresti, G.S. Pappalardo, F. Riggi, and G.V. Russo, ”GEANT4 simulation of plastic scintillator strips with embedded optical fibers for a prototype of tomographic system”, Nuclear Instruments and Methods in Physics Research A 624, pp. 583-590, (2010).

[4] ZEMAXR®, A registered trademark of Radiant ZEMAX LLC.

[5] M.G. Stamatelatos and T.R. England, ”Accurate Approximations to Average Beta-Particle Energies and Spectra”, Nuclear Science and Engineering 60, pp. 204-208, (1977).

Counting Efficiency of Sealed Sheet Sources for Calibration of Whole-Body Counters by Monte Carlo Simulation

R. Kouno[1], N. Ishigure[1]

[1]*Department of Radiological Technology, Graduate School of Medicine, Nagoya University*
1-1-20 Daikou-Minami, Higashi-ku, Nagoya, Japan
e-mail: kouno.ryuji@c.mbox.nagoya-u.ac.jp

Abstract

For internal exposure monitoring, in vivo counters, such as whole-body counters, are sometimes used for direct measurements of radionuclides in human bodies prior dose assessment. We are developing sealed sheet sources for calibration of whole-body counters. Calibration coefficients for a set of the sheet sources (hereafter referred as a sheet phantom) were evaluated by Monte Carlo simulation and compared with those for the BOMAB phantom, the most commonly used bulk phantom for calibration of whole-body counters. The result demonstrated that the differences of them between the two phantoms were negligibly small and therefore that a sheet phantom can be used for calibration of whole-body counters as a surrogate of a bulk phantom with sufficiently good accuracy.

1. Introduction

For internal exposure monitoring, in vivo counters, such as whole-body counters, are sometimes used for direct measurement of radionuclides in human bodies prior dose assessment. Simplified physical bulk phantoms are sometimes used for calibration of whole-body counters.[1,2] But application of bulk phantoms has some problems:

  -the shape and the size are not the same to those of a real human subject,
  -only the homogeneous distribution of radionuclides is available,
  -it is not easy to replace the radionuclides with the other radionuclides,
  -the radioactive solution is likely to leak and contaminate the detection system.

In order to solve these problems, we are developing sealed sheet sources for calibration of whole-body counters. Sealed sheet sources are prepared by mixing radioactive solution with ink of an inkjet printer, printing an image of a section of human body on a sheet of paper with an inkjet printer and sealing it up with lamination films. The method to prepare the sources was reported elsewhere.[3] In the present study calibration coefficients for a set of the sheet sources (hereafter referred as a sheet phantom) were evaluated by Monte Carlo simulation and compared with those for the BOMAB (Bottle Mannequin Absorber) phantom, the most commonly used bulk phantom for calibration of whole-body counters.

2. Materials and Methods

2.1 Calculation geometry

The phantom was composed of two regions of thorax and abdomen. They are both elliptic cylinders: the former

region has a major axis 30cm, the minor axis 20cm, 40cm height, and the later has a major axis 36cm, a minor axis 20cm, height 20cm. The shell of each elliptic cylinder was made of 0.48cm thick polyethylene wall. The material filled in the phantom regions was water.[4]

The detector was composed of 7.62cm diameter $\times$ 7.62cm in length NaI crystal, covered with air of 0.24cm thick and aluminum of 0.05cm thick.   In order to reduce the influence of surrounding natural radiation and scattered radiation by the outermost circumference, it was covered with lead shields of 5cm in thickness.
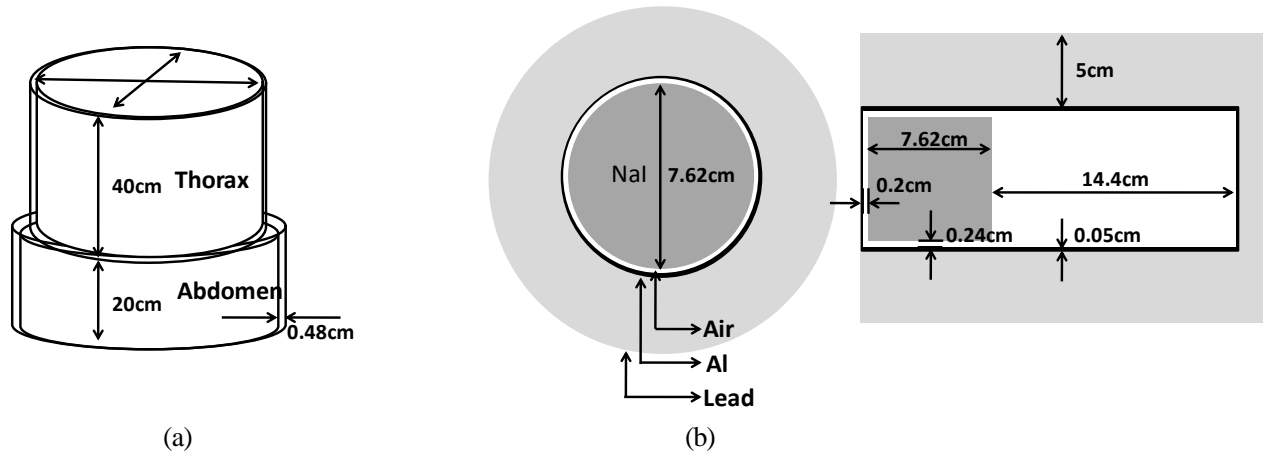
Figure 1.   Calculation geometry:
(a) Simplified physical bulk phantom and (b) NaI detector

Table 1.   Simplified physical bulk phantom dimension

Region	Dimension a (cm)	Dimension b (cm)	Height (cm)	Fill vol. (cc)
Thorax	20	30	40	17000
Abdomen	20	36	20	10000

2.2 Alignment of radioactive source

Alignment of radioactive source had two types.   For a volume source, radioactive source was homogeneously distributed in the phantom.   Sheet sources were inserted in the elliptic cylinders parallel to the plane of the bottom of the cylinder with a fixed interval between them.   The total numbers of histories were set to be the same to each other between the two source alignments (the statistical uncertainty <3%).   The number of histories in each region was calculated by dividing the total number of histories by the volume ratio between them.   The number of histories per sheet was calculated by dividing the number of histories in each region by the seat number.

Table 2.   Sheet source parameter: (a) the number of histories and (b) the position of each sheet source

(a)

Region	Fill vol. (cc)	total histories	histories per region	histories per sheet
Thorax	17000	81000000	51000000	3187500
Abdomen	10000		30000000	3750000

(b)

seat number	Thorax (cm)	Abdomen (cm)
1	-1.25	1.25
2	-3.75	3.75
3	-6.25	6.25
4	-8.75	8.75
5	-11.25	11.25
6	-13.75	13.75
7	-16.25	16.25
8	-18.75	18.75
9		21.25
10		23.75
11		26.25
12		28.75
13		31.25
14		33.75
15		36.25
16		38.75

2.3 Monte Carlo simulation

In the present study, Electron Gamma Shower 5 (EGS5) was used as a Monte Carlo code.   Energy spectrum inside a detector was calculated by simulation.   The number of 662keV photons which imitated γ-rays from Cs-137 (from Ba-137m, in reality) was accumulated.   Counting efficiency was calculated by dividing the accumulated number of 662keV photons by the total number of histories.   Counting efficiency was calculated both for the volume source and the sheet sources.   The detector was fixed at the height of 20cm from the bottom of the abdomen that corresponds to the boundary between the thorax and the abdomen.   Detector-phantom surface distance was determined as 0cm, 2cm, 4cm, 6cm and 10cm.

2.3 Comparison with Visual Monte Carlo in-vivo

Visual Monte Carlo in-vivo (VMC in-vivo) was made by IRD (Institute of Radiation Dosimetry).   VMC in-vivo simulates mathematically the geometry of whole body counter systems, transports photons through this geometry, and finally simulates the detection of the photons.   VMC in-vivo then calculates the calibration coefficient in Bq/cps for the chosen radionuclide, photon, detector type and detector position.   VMC in-vivo also simulates the spectrum as would be obtained by a multi channel analyzer. The program has been extensively validated using comparisons of results of physical phantom with known activities of radionuclides, and also through international intercomparisons.   VMC in-vivo has many phantom types.   Among them ANSI BOMAB phantom was chosen to compare with EGS5 in the present study.   The detector was the same to that used for the simulation with EGS5.   Detector-phantom surface distance to be compared was 2cm only.

3.   Results and Discussion

3.1 Comparison of the volume source and the sheet sources

Figure 2(a) shows the result for the comparison of the counting efficiencies between the volume source and the sheet sources.   Both results agreed very well.   The difference was about 1% at maximum when the detector-phantom surface distance was 6cm.

Figure 2(b) shows the spectrum of energy deposited inside the detector.   A total absorption peak was observed at 663ch.   Moreover, escape peak of iodine, Compton edge, a backscattered peak and the absorption peak of characteristic X-rays of lead were observed at 634ch, 470ch, 180ch and 75ch/85ch, respectively.   We considered that these peaks will not be observed in an actual detector because of its limited energy resolution.
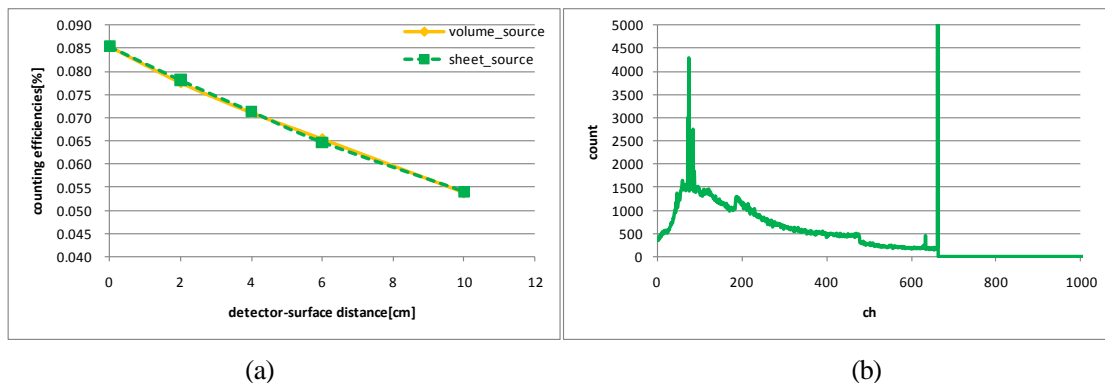

(a)   (b)

Figure 2.   Comparison of the volume source and the sheet sources:
(a) Comparison of the counting efficiency
(b) Energy spectrum inside a detector
(detector-phantom surface distance was 2cm at a seat sources)

3.2 Comparison of EGS5 and Visual Monte Carlo in-vivo

Figure 3 shows the results obtained from the simulation with EGS5 nad from that with VMC in-vivo. The counting efficiencies from the EGS5 simulation were 1.3 times larger than that from VMC in-vivo. Since VMC in-vivo was made by unanalyzable code, the difference between was not analyzed at the moment.
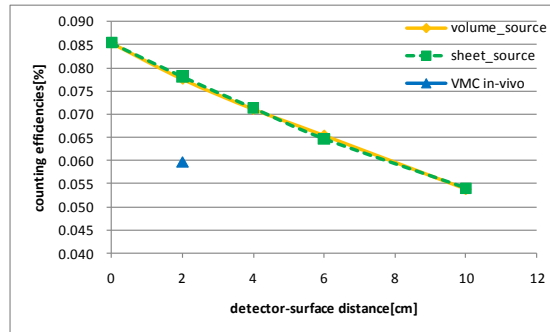

Figure 3. Comparison of the result for EGS5 and VMC in-vivo simulations

4. Conclusion

The present result showed that there was no significant difference in counting efficiencies between the volume source and the sheet sources and therefore that sheet phantom will be used for calibration of whole-body counters as a surrogate of bulk phantom with sufficiently good accuracy. As the next step we will examine how counting efficiency changes depending on the arrangement of sheet sources and on the energy of γ-rays and also we think it necessary to advance the study further in order to demonstrate more the usefulness of sealed sheet sources by carrying out simulations for inhomogeneous distribution of sources in the phantom.

References

1) IAEA, "Intercalibration of in vivo counting systems using an Asian phantom: Results of a co-ordinated research project 1996-1998", IAEA-TECDOC-1334, (2003)
2) IAEA, "safety series: Direct Methods for Measuring Radionuclides in the Human Body", SAFETY SERIES No.114, (1996)
3) MIYAMOTO Mai, ISHIGURE Nobuhito, OGATA Yoshimune, NARITA Norihiko, KAWAURA Chiyo, N, "Development of Sealed Sheet Sources for the Calibration of Whole-body Counters", RADIOISOTOPES Vol.58 No.3, (2009)
4) American National Standard "American National Standard- Specifications for the Bottle Manikin Absorption Phantom", American National Standard N13.35, (1999)

EVALUATION OF SPECIFIC ABSORBED FRACTIONS FOR THYROIDS OF ICRP/ICRU VOXEL PHANTOMS

Masanori KIMURA[1] and Sakae KINASE[1]

[1]Nuclear Safety Research Center, Japan Atomic Energy Agency,
2-4, Shirataka-shirane, Tokai-mura, Ibaraki-ken, 319-1195 Japan
e-mail: kimura.masanori@jaea.go.jp

Abstract

To assess thyroid doses due to intakes of radioiodine in a nuclear accident, it is necessary to evaluate specific absorbed fractions (SAFs) for thyroids in advance.   In the present study, the ICRP/ICRU voxel phantoms were applied to evaluating SAFs for both photons and electrons in thyroids.   The sources were assumed to be monoenergetic in the energy range from 10 keV to 10 MeV.   The radiation transport was simulated using the Monte Carlo code EGS4 in conjunction with an EGS4 user code, UCSAF.   Consequently, it was confirmed that cross-irradiation SAFs evaluated in the present study agreed well with those evaluated by the task group on dose calculations of ICRP Committee 2, except for electrons with low energies.   The cross-irradiation SAF evaluations were found to be subject to the treatment of bremsstrahlung photons and the set cutoff energies in the radiation transport.   The self-irradiation SAFs evaluations for photons and electrons in thyroids will be useful to evaluate the equivalent doses to the thyroid.

1.   Introduction

A Level 3 probabilistic safety assessment (PSA) can be useful for providing a quantitative basis on discussing the effective emergency plan for nuclear facilities.   The OSCAAR (Off-site Consequence Analysis code for Atmospheric Release in Reactor Accident) has been developed as a Level 3 PSA code at the Japan Atomic Energy Research Institute (JAERI, formerly JAEA) [1].   In the OSCAAR, the data on the downwind transport, airborne dispersion and ground deposition of radioactive materials for all sampled weather conditions, and the radiation doses from all relevant pathways such as cloudshine, groundshine and inhalation are calculated.   The off-site consequence of a severe reactor accident in which a plume of radioactive materials is released to the atmosphere can be evaluated.   At the Japan Atomic Energy Agency, dose assessment methods in applying the 2007 Recommendations of the International Commission on Radiological Protection (ICRP) are developed to improve the OSCAAR.

In the 2007 Recommendations of ICRP, the ICRP adopted the computational models for forthcoming updates of organ dose coefficients for both internal and external radiation sources [2].   The ICRP and the International Commission on Radiation Units and Measurements (ICRU) have developed reference computational models i.e. ICRP/ICRU voxel phantoms of the Reference Male and Reference Female for calculations of the protection quantities, such as specific absorbed fractions (SAFs) - the fraction of energy emitted as a specified radiation type in a source organ that is absorbed per unit mass of target organ- for internal exposures.   The task group on dose calculations (DOCAL) of ICRP Committee 2 have evaluated SAFs for selected source and target organs in the ICRP/ICRU voxel phantoms [3]. However, published data on SAFs are limited.

To assess thyroid doses due to intakes of radioiodine in a nuclear accident, it is needed to evaluate SAFs for thyroids in advance.   In the present study, SAFs for both photons and electrons in thyroids of the ICRP/ICRU voxel phantoms were evaluated using Monte Carlo simulations.   First, cross-irradiation SAFs for source region thyroid and target region lungs or stomach wall were evaluated and compared with those evaluated by DOCAL of ICRP Committee

2. Next, self-irradiation SAFs for thyroids were evaluated.

2. Materials and Methods

2.1 ICRP/ICRU voxel phantoms

In the present study, the ICRP/ICRU adult male and female reference voxel phantoms were used.   Figure 1 shows images of the male and female reference phantoms [4].   The voxel phantoms, based on computed tomographic data sets, were developed by DOCAL of ICRP Committee 2 in collaboration with the Helmholtz Zentrum München – German Research Centre for Environmental Health (formerly - GSF) and ICRU.   Table 1 shows characteristics of the adult male and female reference voxel phantoms.   The voxel sizes are $2.137 \times 2.137 \times 8.0$ mm^3 for the adult male voxel phantom and $1.775 \times 1.775 \times 4.84$ mm^3 for the adult female voxel phantom.

2.2 Calculation of Specific Absorbed fractions (SAFs)

The specific absorbed fraction Φ is the absorbed fraction -the fraction of the energy emitted by source organ r_S that is absorbed in target organ r_T- in the target per unit mass of the target m_i.   It can be expressed by the equation:

$$\Phi_i(r_T \leftarrow r_S) = \frac{1}{m_i} \cdot \frac{\text{(i-type radiation energy absorbed in target } r_T)}{\text{(i-type radiation energy emitted in source } r_S)} \tag{1}$$

Specific absorbed fractions for photons and electrons were evaluated for the ICRP/ICRU adult male and female reference voxel phantoms using the Monte Carlo code, EGS4 [5] in conjunction with an EGS4 user code, UCSAF [6]. In the EGS4-UCSAF code, the radiation transport of electrons, positrons and photons in the phantoms is simulated.   In the present study, the sources of photons and electrons were assumed to be monoenergetic in the energy range from 10 keV to 10 MeV and uniformly distributed in a source organ.   The source organ was thyroid.   Photon and electron histories were run at numbers sufficient to reduce statistical uncertainties below 5%.   The cutoff energies were set to 1 keV for the photons and 10 keV for the electrons.   The Parameter Reduced Electron-Step Transport Algorithm (PRESTA) [7] to improve the electron transport in the low-energy region was used.   The cross-section data for photons were taken from PHOTX [8] and the data for electrons were taken from ICRU report 37 [9].

3. Results and Discussion

3.1 Cross-irradiation SAFs

Figures 2 (a) and (b) show cross-irradiation SAFs for photons and electrons in the ICRP/ICRU adult male and female reference voxel phantoms in the energy range from 10 keV to 10 MeV.   The source organ is thyroid and the target organ is lungs.   The cross-irradiation SAFs for photons gradually decrease with an increase in photon energy on the whole.   The cross-irradiation SAF for electrons shows an abrupt increase up to 10 MeV.   In Figs. 2 (a) and (b), the cross-irradiation SAFs published by DOCAL of ICRP Committee 2 are also plotted for comparison.   It can be seen from the figures that the cross-irradiation SAFs evaluated in the present study are in good agreement with those evaluated by ICRP.

Figures 3 (a) and (b) show cross-irradiation SAFs for photons and electrons in the ICRP/ICRU adult male and female reference voxel phantoms in the energy range from 10 keV to 10 MeV.   The source organ is thyroid and the target organ is stomach walls.   The cross-irradiation SAFs for photons increase up to 100 keV and then are almost constant with an increase in photon energy up to 10 MeV.   The cross-irradiation SAF for electrons shows an abrupt increase up to 10 MeV.   Figures 3 (a) and (b) also provide that the cross-irradiation SAFs evaluated in the present study agree exactly with those evaluated by ICRP.   However, it must be emphasized that the cross-irradiation SAFs for electrons with low energies are different from those evaluated by ICRP as shown in Fig 3 (b).   The cross-irradiation

SAFs for electrons with low energies up to 100 keV would be replaced with zero in DOCAL of ICRP Committee 2.　On the other hand, in the present study the cross-irradiation SAFs for electrons up to 100 keV could be evaluated.　These discrepancies are thought to be due to the set of cutoff energies and the treatment of bremsstrahlung photons in the radiation transport.

3.2 Self-irradiation SAFs

Figures 4 (a) and (b) show self-irradiation SAFs for photons and electrons in thyroids of the ICRP/ICRU adult male and female reference voxel phantoms in the energy range from 10 keV to 10 MeV.　The self-irradiation SAF for photons decreases up to 100 keV and is almost constant from 100 keV to 1 MeV and then decreases with an increase in photon energies.　The self-irradiation SAF for electrons shows constancy up to 1 MeV and then a decrease with an increase in photon energy.　The data will be useful to evaluate the equivalent doses to the thyroid.

4.　Conclusions

Specific absorbed fractions for photons and electrons were evaluated for the ICRP/ICRU adult male and female reference voxel phantoms using the EGS4-UCSAF code.　Consequently, it was confirmed that cross-irradiation SAFs evaluated in the present study agreed well with those evaluated by ICRP, except for electrons with low energies.　The set of cutoff energies and the treatment of bremsstrahlung photons should be considered with discretion in the radiation transport. In the present study, the self-irradiation SAFs for photons and electrons in thyroids were also evaluated.　The data will be useful to evaluate the equivalent doses to the thyroid.

References

1) T. Homma, K. Tomita, S. Hato, "Uncertainty and sensitivity studies with the probabilistic accident consequence assessment code OSCAAR," Nuclear Engineering and Technology. 37 (3), 245-258 (2005).
2) International Commission on Radiological Protection, "The 2007 recommendations of the International Commission on Radiological Protection," ICRP Publication 103, Annals of the ICRP 37 (2-4) (2007).
3) International Commission on Radiological Protection, "Adult reference computational phantoms," ICRP Publication 110, Annals of the ICRP 39 (2) (2009).
4) M. Zankl, J. Becker, U. Fill, *et al.*, 2005. GSF male and female adult voxel phantoms representing ICRP Reference Man – the present status. In: The Monte Carlo Method: Versatility Unbounded in a Dynamic Computing World. American Nuclear Society, LaGrange Park, IL (2005).
5) W. R. Nelson, H. Hirayama and D. W. O. Rogers, "The EGS4 Code System," SLAC-265 (1985).
6) S. Kinase, M. Zankl, J. Kuwabara, *et al.*, "Evaluation of specific absorbed fractions in voxel phantoms using Monte Carlo simulation," Radiat. Prot. Dosim. 105, 557 (2003).
7) A. F. Bielajew and D. W. O. Rogers, "Electron step-size artefacts and PRESTA," in Monte Carlo Transport of Electrons and Photons, T. M. Jenkins, W. R. Nelson, and A. Rindi, Eds. Plenum Press, ISBN 0-306-43099-1, New York (1987).
8) "Photon Interaction Cross Section Library," DLC-136/PHOTX, contributed by National Institute of Standards and Technology (1989).
9) "Stopping Powers for Electrons and Positrons," ICRU Report 37 International Commission on Radiation Units and Measurements (1984).

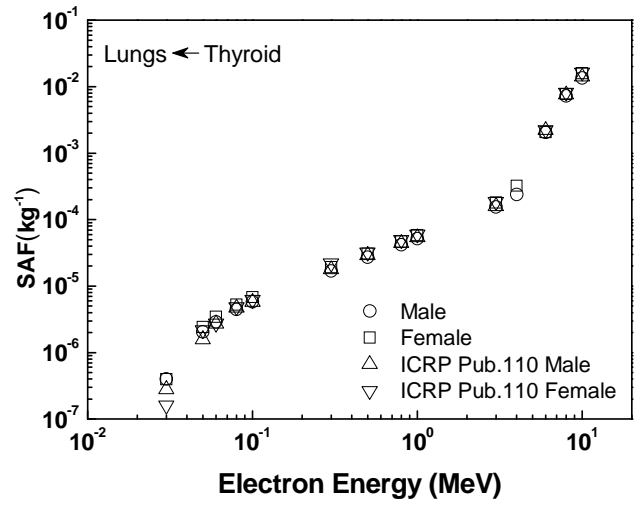**Table 1.** Characteristics of the adult male and female reference computational phantoms

	Male	Female
Property		
Height (m)	1.76	1.63
Mass (kg)	73.0	60.0
Organs		
Thyroid (kg)	2.0×10^{-2}	1.7×10^{-2}
Lungs (kg)	1.2×10^{0}	9.5×10^{-1}
Stomach wall (kg)	1.5×10^{-1}	1.4×10^{-1}

Figure 1. Images of the male (left) and female (right) reference computational phantom [5].
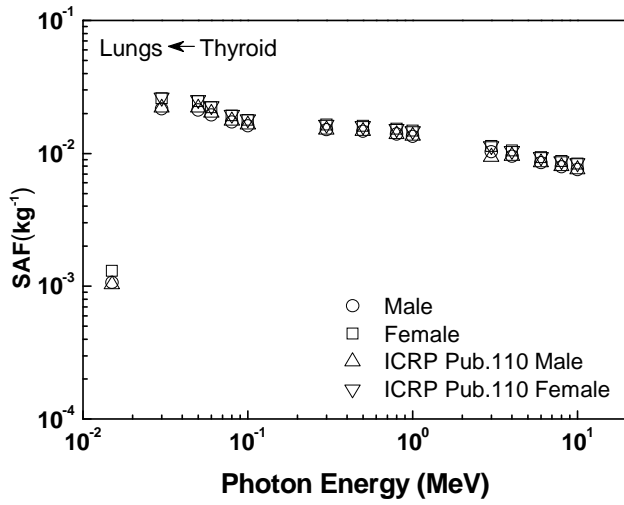
Figure 2.   Specific absorbed fractions for monoenergetic photons (a) and electrons (b) for source organ thyroid and target organ lungs.
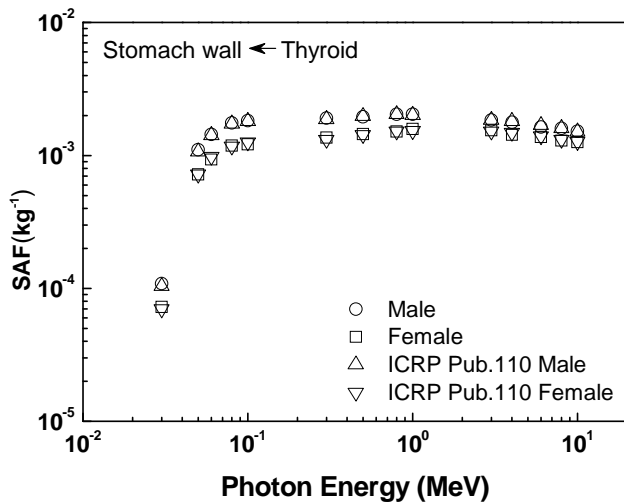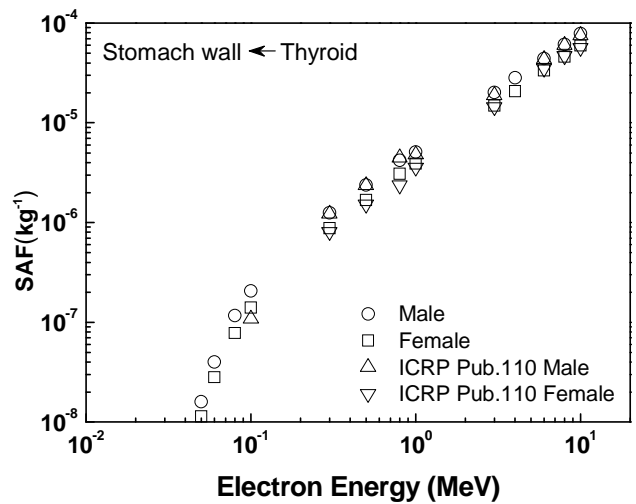
Figure 3.   Specific absorbed fractions for photons (a) and electrons (b) for source organ thyroid and target organ stomach wall.
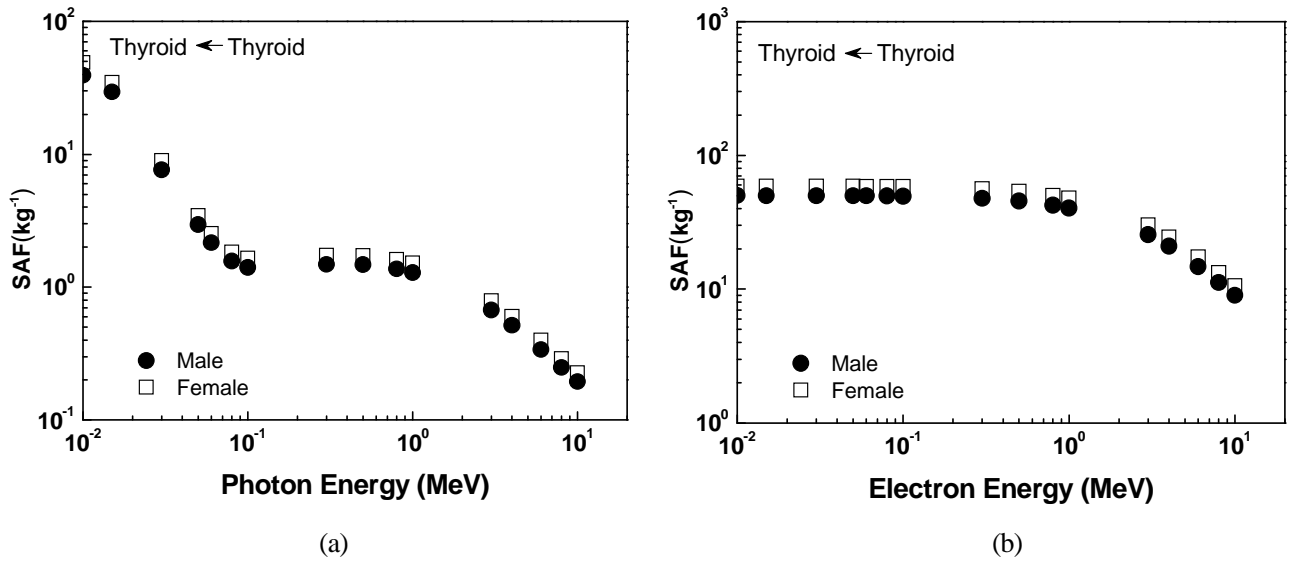
Figure 4. Specific absorbed fractions for photons (a) and electrons (b) for self-irradiation of thyroid.

ABOUT $g(r)$ FUNCTION IN AAPM TG-43

S. TSUJI and N. NARIHIRO[†]

Kawasaki Medical School, Kurashiki 701-0192, Japan
[†]*Kawasaki College of Allied Health Professions, Kurashiki 701-0194, Japan*

Abstract

Treatment plans for high dose-rate brachytherapy are calculated in AAPM TG-43. The formula TG-43 depends on kinds of high dose souses. The formula has some tables for each source. A radiation dose in TG-43 is investigated by measurements or Monte Carlo simulations. The investigation is limited to measure fixed volume in phantom. The dose is different in each phantom volume. We report that $g(r)$ function is different between EGS5 and TG-43 in each phantom volume and indicate the difference of the dose between EGS5 and TG-43.

1   Introduction

The microSelectron-HDR remote afterloading device with high-intensity ^{192}Ir sources is used for brachytherapy. The sources capsuled in a stainless are embedded and irradiate the prostate. A clinical treatment is planned before an actual irradiation in a body. The calculated values of doses are derived from Oncentra clinical planning system. The calculation algorism follows American Association of Physicists in Medicine Task group No.43 Report (AAPM TG-43) [1], and they are based on dose-rate distributions used for clinical implementation and dose-calculation methodologies. AAPM TG-43 is generally the only way of the algorism for brachytherapy in radiology. The accuracy of TG-43 formalism in Oncentra clinical planning system has been validated by investigating the absolute dose [2]. However the absolute dose is investigated in a liquid water phantom with a specified shape and volume. Some paper reports that $g(r)$ function in TG-43 changes in phantoms with different shapes and volumes [3, 4, 5]. It is difficult to measure and summarize doses using in various phantoms. Investigating complicated electromagnetic scattering in various shapes and volume of phantoms is best to use a Monte Carlo simulation. We report that doses and $g(r)$ functions using in various phantom volumes investigating by Monte Carlo simulation EGS5.

2   AAPM TG-43 and Monte Carlo simulation EGS5

The PLATO brachytherapy planning system calculate based on AAPM TG-43 [1]. The dose-rate equation is following,

$$\dot{D}(r,\theta) = S_k \cdot \Lambda \cdot \frac{G(r,\theta)}{G(r_0,\theta_0)} \cdot g(r) \cdot F(r,\theta), \tag{1}$$

where r denote the distance (in centimeters) from the center of the active source to the point of interest, r_0 denotes the reference distance which is specified to be 1 cm in this protocol, and θ denotes the polar angle specifying the point of interest, θ_0 denotes the reference angle which is specified to be 90° shown as Fig.1. The other parameter S_k, Λ, $G(r,\theta)$, $g(r)$ and $F(r,\theta)$ represent the air-kerma strength, the dose rate constant, the geometry function, the radial dose function and the 2D anisotropy function respectively. S_k is calculated as the source intensity when the treatment starts. Λ is used the value 1.108 cGy/h/U in this planning system. The unit U is defined as the air-kerma strength, 1U=1cGy·cm²/h.
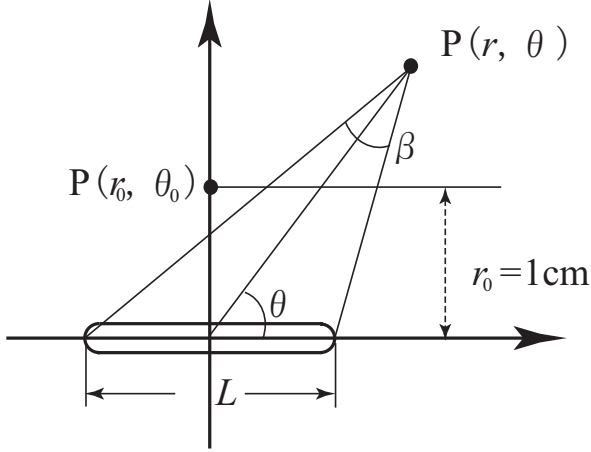
Figure 1: Coordinate system used for brachytherapy dose calculations. $P(r,\theta)$ represents the interesting point. r_0 and θ_0 mean 1 cm and 90° respectively.
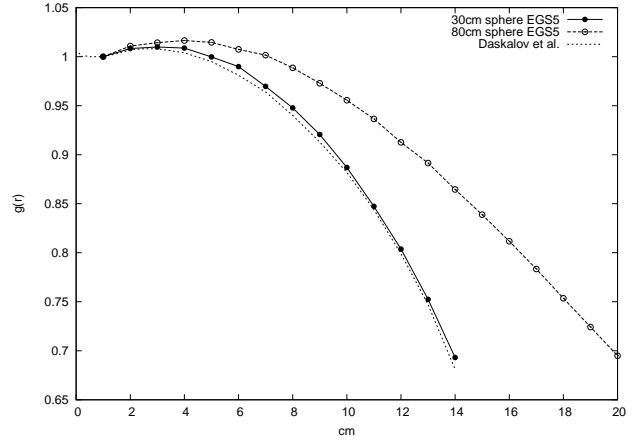
Figure 2: $g(r)$ functions in liquid water phantoms. A solid line and closed circles: $g(r)$ in a 30 cm diameter spherical phantom. A dashed line and open circles: $g(r)$ in an 80 cm diameter spherical phantom. A dashed line: Daskalov et al. results [2].

2.1 Radial dose function

The radial dose function, $g(r)$, accounts for dose fall-off on transverse-plane due to photon scattering and attenuation, and is defined by Eq.(2),

$$g(r) = \frac{\dot{D}(r,\theta_0)}{\dot{D}(r_0,\theta_0)}\frac{G(r_0,\theta_0)}{G(r,\theta_0)}. \tag{2}$$

$G(r,\theta)$ is determined by the geometry of sources. Therefore from Eq.(2), we can get $g(r)$ values from simulating doses in linear positions.

2.2 Monte Carlo simulation EGS5

We simulate doses in some shapes and volumes of phantoms using EGS5. For the EGS5 simulating, the following parameters are considered in various regions or mediums, sampling of angular distributions of photoelectrons, K and L edge fluorescent photons, K and L Auger electrons, Rayleigh scattering, linearly polarized photon scattering, incoherent scattering and Doppler broadening of Compton scattering energies. We continued the simulations until the cut off kinetic energy 1 keV for one track. The number of injected particles from the source is 10^8 per one Monte Carlo simulation. We use liquid water phantoms and ^{192}Ir sources as points or types of microSelectron-HDR v2.

3 Results

3.1 Comparison of $g(r)$ with a 30cm diameter spherical and a 80 cm diameter spherical phantoms

Fig.2 shows point source $g(r)$ functions. A solid line and closed circles show it in a 30 cm diameter spherical phantom. The $g(r)$ is good agreement with it of Daskalov et al [2]. However the $g(r)$ in a 80 cm diameter spherical phantom as shown a dashed line and open circles in Fig.2 is not agreement with it of Daskalov et al [2]. Same results reports some references [3, 4, 5].

3.2 Comparison of $g(r)$ with a spherical and a partial spherical phantoms

We simulate doses in the partial spherical phantom which is cut off up and down parts as shown in Fig.3. The phantom has a 30 cm diameter spherical volume which has only ± 7 cm range from the center. We summarize the dose in only a 1 cm thickness part of a phantom as shown a center plate in Fig.3. The reason is to check whether absence of the top and bottom phantom affects electromagnetic scattering of the central portion. Values of $g(r)$ each distance from the center show in Fig.4.
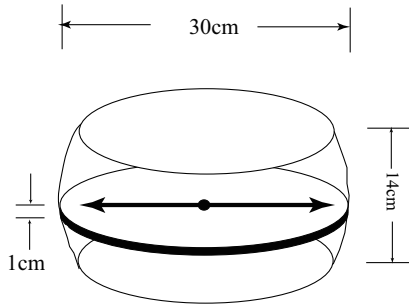
Figure 3: Shape and size of the phantom used in Fig.4. Aggregate area is only 1cm of the black part.
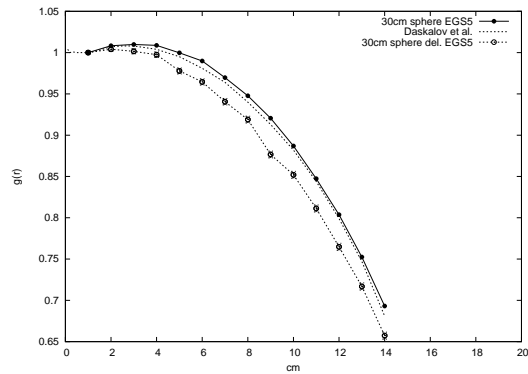
Figure 4: $g(r)$ functions in 2 liquid water phantoms. A solid line and closed circles: $g(r)$ in a 30 cm diameter perfectly spherical phantom. A dashed line and open circles: $g(r)$ in a partial spherical phantom in Fig.3. A dashed line: Daskalov et al [2]. results.

As compare with a complete spherical phantom, $g(r)$ in incomplete spherical phantom falls down. This means $g(r)$ function, in other words, the value of an absolute dose changes by not only size but also shape of a phantom.

## 3.3 Comparison of $g(r)$ with various heights and a 50 cm diameter cylindrical phantoms
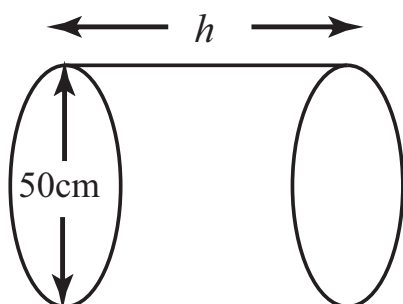
Figure 5: A cylindrical phantom. A diameter is fixed 50 cm. A height is varied from 15 cm to 200 cm.
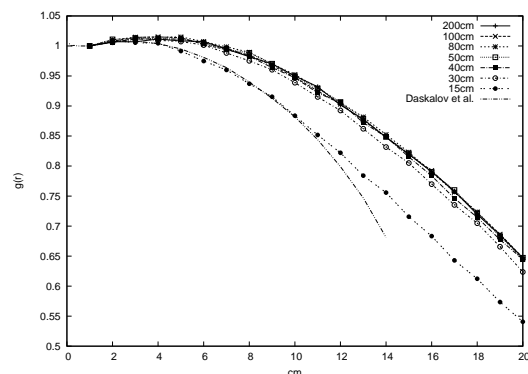
Figure 6: $g(r)$ functions in various cylindrical phantoms in Fig.5. Dashed and 2 dotted line shows Daskalov et al [2]. results.

Later in this chapter, since a circular cylinder roughly close to body shape, we use cylindrical

phantoms for simulations. For the first time, we decide 50 cm diameter of the cylindrical phantoms. We simulate doses to lead $g(r)$ in various heights of cylindrical phantoms as shown in Fig.5. Fig.6 shows $g(r)$ functions in case of phantoms in Fig.5. The horizontal axis of Fig.6 shows the distance from the center of gravity to the circumference. $g(r)$ functions become constant while heights are more than 50 cm.

3.4 Comparison of $g(r)$ with various diameters and a 100 cm height cylindrical phantoms

Under the condition that the cylindrical phantoms are fixed 100 cm height, we simulate doses to lead $g(r)$ in various diameter of the phantoms as shown in Fig.7.
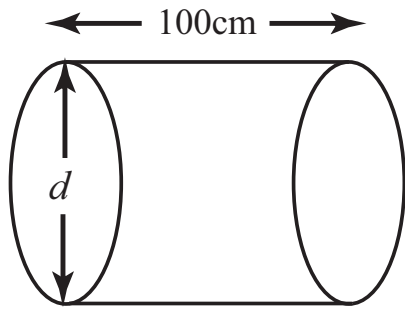
Figure 7: A cylindrical phantom. A height is fixed 100 cm. A diameter is varied from 15 cm to 200 cm.
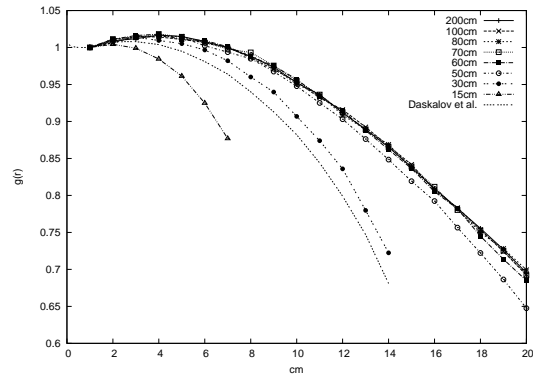
Figure 8: $g(r)$ functions in various cylindrical phantoms in Fig.7. Dotted line (only line without plots) shows Daskalov et al. results [2].

Fig.8 shows $g(r)$ functions in case of phantoms in Fig.5. The horizontal axis of Fig.8 also shows the distance from the center of gravity to the circumference. $g(r)$ functions become constant while diameters are more than 70 cm.
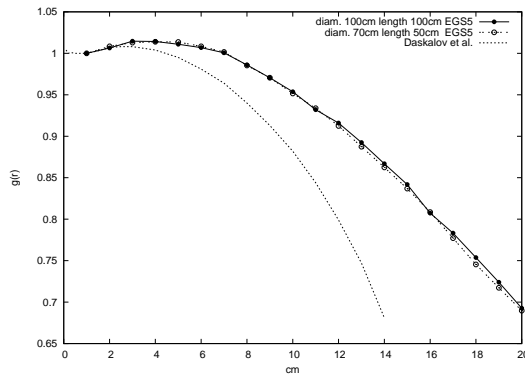
Figure 9: $g(r)$ functions in 2 liquid water cylindrical phantoms. A solid line and closed circles: $g(r)$ in a 100 cm diameter and 100 cm height cylindrical phantom. A dashed line and open circles: $g(r)$ in a 70 cm diameter and 50 cm height cylindrical phantom. A dashed line: Daskalov et al. results [2].

3.5 Confirmation of the height and the diameter of the phantom

We decide on an appropriate diameter in Section 3.3 and an appropriate height in Section 3.4. We check that the phantom which has a 70 cm diameter and a 50 cm height is regards as an enough large cylindrical phantom. The phantom which has a 100 cm diameter and a 100 cm height is regarded as enough large. Fig.9 shows $g(r)$ functions in two phantoms. One has a 70 cm diameter and a 50 cm height and the other has a 100 cm diameter and a 100 cm height. They are good agreement each other. In conclusion, when a dose is measured in a phantom, the cylindrical phantom which has more than a 70 cm diameter and a 50 cm height is regard as an infinity large phantom.

3.6 $g(r)$ functions with simulations using microSelectron-HDR v2

MicroSelectron-HDR v2 ^{192}Ir source has a structure in Fig.10. We compare $g(r)$ functions using this source in two type of phantoms. One has a 70 cm diameter and a 50 cm height and the other has a 100 cm diameter and a 100 cm height. Fig.11 shows $g(r)$ functions. Same the case of using a point souse, it shows good agreement in the case of the microSelectron-HDR v2 source. Therefore the cylindrical phantom which has more than a 70 cm diameter and a 50 cm height is regard as an infinity large phantom using the microSelectron-HDR v2 source.
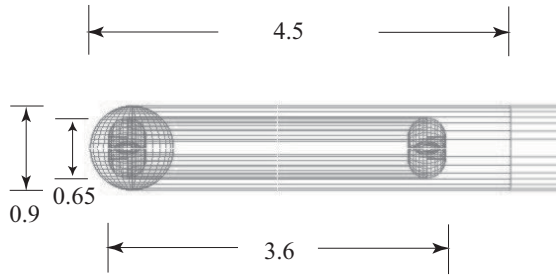

Figure 10: Mechanical design of microSelectron-HDR v2 ^{192}Ir source utilized by EGS5 simulations. The capsule is made of SUS316L. All dimensions are in mm.
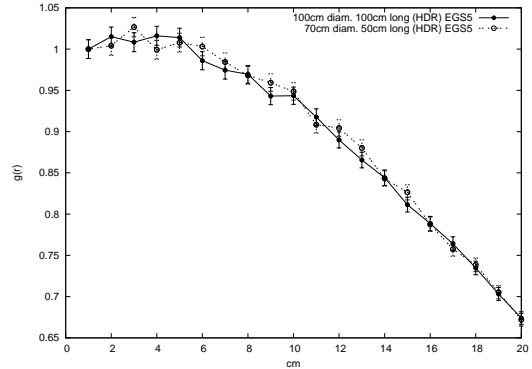

Figure 11: $g(r)$ functions using microSelectron-HDR v2 source in cylindrical phantoms. A solid line and closed circles: $g(r)$ in a 100 cm diameter and 100 cm height cylindrical phantom. A dashed line and open circles: $g(r)$ in a 70 cm diameter and 50 cm height cylindrical phantom.

3.7 Absolute doses using microSelectron-HDR v2 source

Absolute doses of microSelectron-HDR v2 ^{192}I new design type are simulated in 2 type of phantoms. Ir metal density is greater ($=22.4$ g/cm^3). So a survival probability of gamma-ray going from the inside the metal is smaller than 0.9. We check the survival probability using EGS5 Monte Carlo simulation considering with a structure of a ^{192}Ir source and a stainless capsule. The value is 0.88029. We gain the absolute dose also with the emission rate 2.072 following equations,

$$\text{Absolute dose (Gy/sec.)} = \text{Using radioactivity (Bq)} \times \text{Simulation value (Gy/incident)} \times 2.072/0.88029. \tag{3}$$

One type of phantoms is a spherical phantom. The diameter is 30 cm. Simulated absolute doses are compared with Oncentra calculations. They are shown in Fig.12 and Fig.13. They are
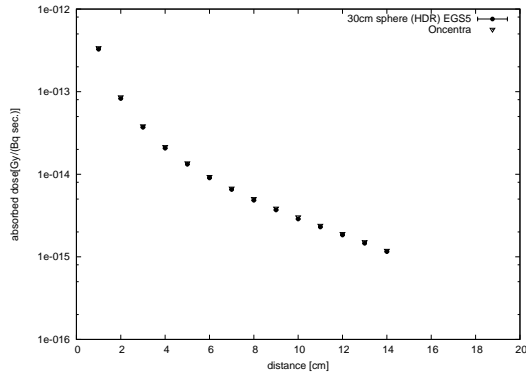
Figure 12: Absolute doses of microSelectron-HDR v2 sources simulated by EGS5 and calculated by Oncentra planning system. EGS5 simulation uses a 30 cm diameter spherical phantom. Closed circles : EGS5. Open triangles : Oncentra.
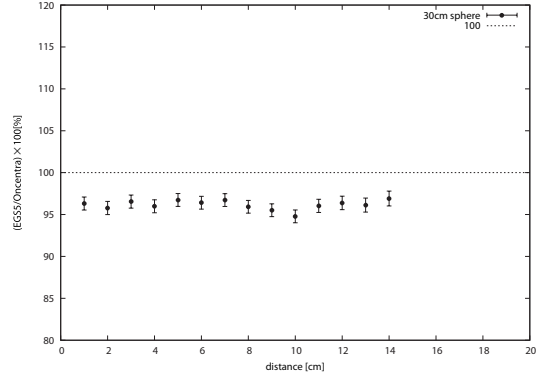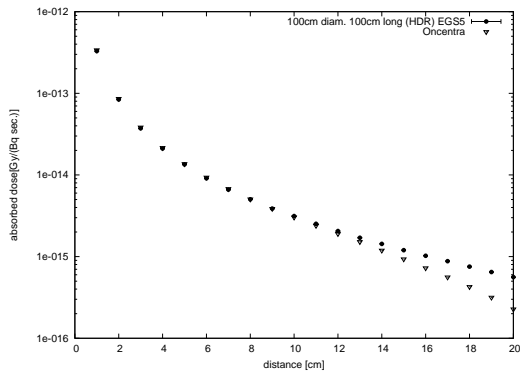

Figure 13: Absolute doses relative error of the EGS5 simulation for the Onsentora calculations. EGS5 simulation uses a 30 cm diameter spherical phantom.

good agreement each other in Fig.12. Fig.13 shows the relative error examined in detail. Errors are constant regardless of the distance. These errors are around 4 % and considered systematical ones between EGS5 simulations and Oncentra calculations.

Figure 14: Absolute doses of microSelectron-HDR v2 sources simulated by EGS5 and calculated by Oncentra planning system. EGS5 simulation uses a 100 cm diameter and 100 cm height cylindrical phantom. Closed circles : EGS5. Open triangles : Oncentra.
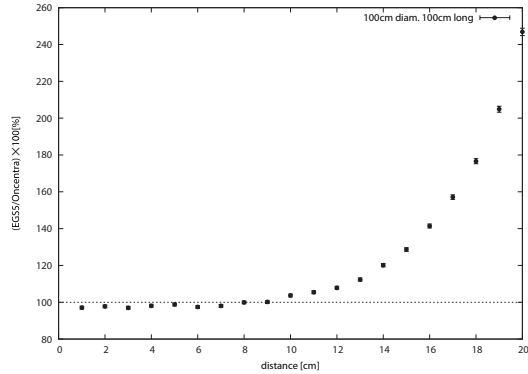

Figure 15: Absolute doses relative error of the EGS5 simulation for the Onsentora calculations. EGS5 simulation uses a 100 cm diameter and 100 cm height cylindrical phantom.

The other type of phantom is a cylindrical phantom which has a 100 cm diameter and a 100 cm height. The phantom is regarded as enough large. Simulated absolute doses are also compared with Oncentra calculations. The Oncentra calculation refers Daskalov's data which is investigated in a liquid water 30 cm diameter spherical phantom [2]. Therefore they are not good agreement over 10 cm as shown in Fig.14. Fig.15 shows the relative error examined in detail. When the distance is more than 10cm, the error is much larger. At the 20 cm, the error is over 240%.

4   Conclusion

We simulate $g(r)$ functions and absolute doses using EGS5. In section 3.1, $g(r)$ with a 30 cm diameter spherical phantom is good agreement with Daskalov's results [2] and it with an 80 cm diameter is larger than with a 30cm diameter. In section 3.2, we conclude that the $g(r)$ function or the absolute radiation dose depend on not only a volume but also a shape of a phantom. In section 3.3, 3.4 and 3.5, a cylindrical phantom with a diameter more than 70 cm and a height more than 50 cm is considered as an infinity large phantom. In section 3.6 and 3.7, we simulate using microSelectron-HDR v2 source. In section 3.6, the phantom with a 70 cm diameter and 50 cm height is also regarded as an infinity phantom in case using microSelectron-HDR v2 source. In section 3.7, we compare the EGS5 simulation and the Oncentra calculation. The Oncentra calculations are investigated with a liquid water 30 cm diameter spherical phantom. Therefore the absolute doses are good agreement with ones simulated EGS5 in case with a 30 cm diameter spherical phantom. On the other hand, the absolute doses calculated the Oncentra are not agreement with ones simulated EGS5 in case with an enough large, 100 cm diameter and 100 cm height cylindrical phantom. At the 20 cm, the error is over 240%. EGS5 simulation shows that the absolute dose changes with a shape and size of the phantom. This means that the Oncentra calculating dose for a very large human body is underestimated at least 10 cm away from an irradiated part.

References

[1] M. J. Rivard et al., Med. Phys. **31** 3,633(2004).

[2] G. M. Daskalov, E. Lőffler, J. F. Williamson, Med. Phys. **25** 11, 2200(1998).

[3] D. Granero et al., Med.Phys. **35** 11,4872(2008).

[4] P. Karaikos, A. Angelopoulos, L.Sakelliou, Med. Phys. **25** 10,1975(1998).

[5] R. E. P. Taylor and D. W. O. Rogers, Med.Phys. **35** 11,4933(2008).

Monte Carlo study of virtual plane source of linear accelerator in radiotherapy

T.Rachi, K.Ota, A.Henmi, Y.Iwamoto, M.Tamura, T.Matsunaga[1], Y.Oribe[2], M.Komori, and Y.Obata

Nagoya University, Graduate School of Medicine
1-1-20 Daikou-Minami, Higashi-ku, Nagoya, Japan
[1]Seirei Hamamatsu General Hospital
[2]Saitama Children's Medical Center
E-mail: rachi.tosiya@e.mbox.nagoya-u.ac.jp

Abstract

In the radiotherapy, the interactions of the high energy electrons are much different from those of the diagnostic imaging. The calculating time of Monte Carlo simulation with EGS5 from the target to the water phantom is very long. Therefore, the practicability is low at the clinical site. In this study, we investigated the calculating time using the method named a variance reduction for improving the practicability.

The structures from the target to the water phantom were made by using CGView with the structural data of CLINAC series of VARIAN. The energy of incident electrons is 4 MeV. For making virtual plane source, we must acquire the fluence map through a flattening filter. The fluence map is sectioned to nine regions because the generation ratio of photon is different at each region. Then we obtained percentage depth dose (PDD) and off center ratio (OCR), and compared those to measured values.

As the results, the calculated PDD almost agreed with the measured PDD. But the penumbra and the edge of the OCR did not agree with the measured OCR. We suppose that the difference is caused by the effect of the scatters which are generated from the primary collimator, the flattening filter and jaws.

1. Introduction

In the radiotherapy, the interactions of the high energy electrons are much different from those of the diagnostic imaging and may have an influence on a normal tissue. Therefore, the high accurate treatment planning using the Monte Carlo (MC) simulation with EGS5 must be made before the irradiation.

To obtain the fractional standard deviation of 1% or less, the incident electrons are assumed to have three billion histories or more. The calculating time of the MC simulation with EGS5 from the target to the water phantom is about 200 days or more with the general personal computer. In this study, we investigated the MC simulation using virtual plane source to reduce the calculating time and to improve the practicability in the radiotherapy.

2.   Materials and Methods

2.1 The modeling of the linear accelerator

The modeling of the linear accelerator from the target to the water phantom was constructed by using CGView with the structural data of CLINAC series of VARIAN.

To reduce the calculating time, a variance reduction method is utilized using the virtual plane source and the phase space file. We assumed that the behaviors of photons and electrons through a flattening filter are constant in spite of the motion of jaws and multi leaf collimators. Therefore we created the virtual plane source between the flattening filter and the upper jaws (y-jaws) and additionally the phase space file on the water phantom to calculate the percentage depth dose (PDD) and the off center ratio (OCR) using these data repeatedly.

For conditions of MC simulation, the incident electron energy is 4 MeV, the irradiation field is 10×10 cm², the under limits of cut off energy is 0.521 MeV for the electron, and 0.01 MeV for the photon.

The obtained PDD and OCR are compared with measured values of CLINAC 21EX (Varian Inc.).

2.2 The fluence map

We need to know the fluence of photons and electrons to design the virtual plane source. The fluence map was acquired by MESH method which creates the virtually divided region between the flattening filter and the upper jaws. The photons or the electrons were counted when entered in the divided region of 0.1 (x-axis)×0.1 (y-axis) cm².

The fluence map of the photons is shown in Figure.1. It shows that the fluence in the central area is fewer because that dependents on the shape of the flattening filter.

2.3 The generation ratios of photons or electrons and the energy spectrums

The obtained fluence map of the photons is rationally sectioned to nine regions because the fluence is different at each region. The generation ratios of the photons and the electrons on the virtual plane source were calculated by dividing the counted number in nine regions into the area of each region. Those of the photons are shown in Table.1. And the energy spectrums of each region are different (Figure.2). However two outside regions are not including in Figure.2 because those regions cannot acquire the photons through the flattening filter. The energy spectrums show that the outside region has more low energy and fewer high energy than the inside region.

The generation ratio and the energy spectrum of the electrons are not separated in each region because those are seemed to homogeneously spread in the virtual regions. The generation of ratio of the electrons is estimated to be 0.8 % from the numbers of the electron in the counted total numbers.

2.4 The directions of photons and electrons from the virtual plane source

The directions of generated photons and electrons from the virtual plane source are determined by a direct-method which releases the generated photons and electrons from the generated points in the virtual source to the opposite direction from the center of the target.

2.5 The scatters from the primary collimator and the flattening filter

We obtained the fluence maps of the photons from the target and from the virtual plane source both under y-jaws and under x-jaws to verify the virtual plane source. Then the fluence map of the photons generated from the target is subtracted by that generated from the virtual plane source. The subtracted image under the y-jaw and that under the x-jaw are shown in Figure.3. It was revealed that the virtual plane source contained very few scatters. The generation ratio of the scatter is calculated by dividing the number of the scatters after subtraction by the total number of the photons under y-jaw. Hence the generation ratio is 8.7 %.

The direction of the scatters was decided by the rejection-method. When the area including the scatter became 16.2 cm×16.2 cm, the penumbra of the calculated OCR almost agreed with measured one.

3. Results

Figure.4 shows the measured and calculated PDD and Figure.5 shows the OCR at each depth.

The calculated PDD and the calculated OCR almost agree with measured those. But the random error is still conspicuous at the edge of the OCR.

4. Discussion

4-1. The virtual plane source

In this study, we sectioned the virtual plane source into nine regions. As the result, the distribution of the photons under the y-jaws was seemed likely to be steps. Therefore, these steps should be corrected by displacing the nine generation ratio of the photon by an approximate function.

4-2. The edge of the OCR

The edge of the OCR was evidently incorrect. However, the event seems to diminish when the number of history for MC is increased.

Two reasons are assumed that the edge is constructed by the scatters more than the center. When the number of the history is few, the effect of the scatter to the edge seems to be larger than to the center. If the number of the history is increased, the absorbed dose of the center will be higher than that of the edge. Therefore, the total absorbed dose will be uniform.

In addition, the energy spectrums show that the outside region has more low energy and fewer high energy than the inside region.

5. Conclusions

In this study, we cannot verify the calculating time using the virtual plane source because of finding the error of the edge of the OCR. However, we found that 60 % ~ 70 % of the total calculating time with the MC simulation from the target to the water phantom are spent until through the flattening filter for obtaining the PDD and the OCR. Therefore, the virtual plane source would help the practicability at the clinical site.

References

1) Rompin Shih, X. Allen Li, James C. H. Chu, Wen-Lin Hsu, "Calculation of head scatter factors at isocenter or at center of field for any arbitrary jaw setting", Med. Phys.26(4),April 1999.
2) Si Young Jang, Oleg N. Vassiliev, H. Helen Liu, Ranhe Mohan, "Development and commissioning of a multileaf collimator model in Monte Carlo dose calculations for intensity-modulated radiation therapy", Med. Phys. 33(3),March 2006.

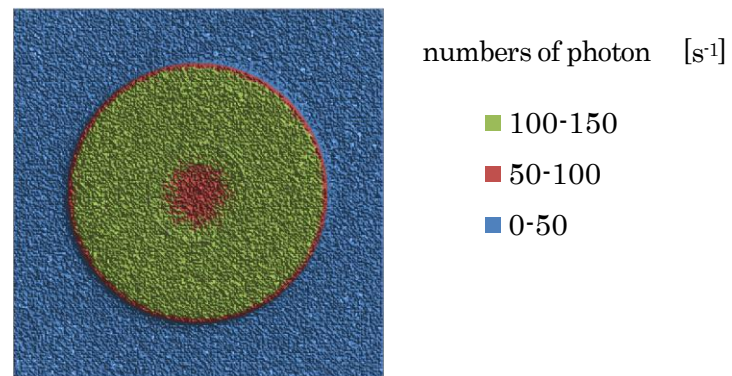| devided region	average	probability (%)
1	70094	1.3
2	273178	5.0
3	321987	5.9
4	730978	13.4
5	1247659	22.9
6	1233537	22.6
7	1044250	19.1
8	357028	6.6
9	180871	3.3
sum	5459582	100.0

Table.1: The generation ratio of photons for the virtual plane source.

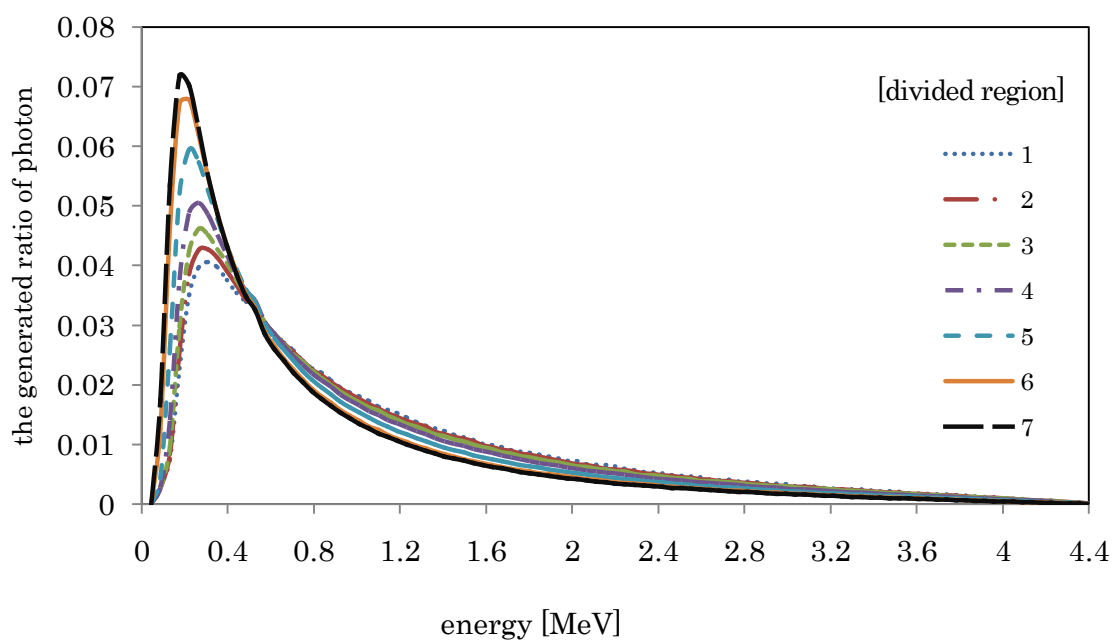Figure.1 : The fluence map of the photons using MESH method.

Figure.2: the generation ratios and the energy spectrums of photon in the each divided region on the virtual plane source.
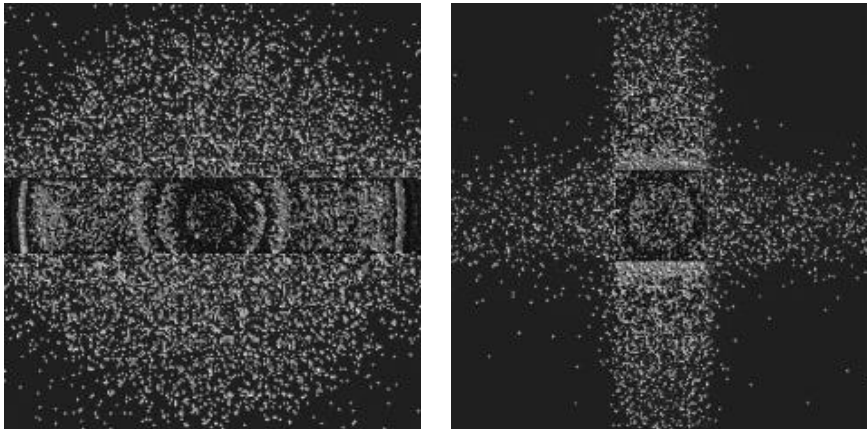
Figure.3: Subtracted images of the fluence map of photon generated from the virtual plane source from that generated from the target. Left : under y-jaw, Right : under x-jaw.
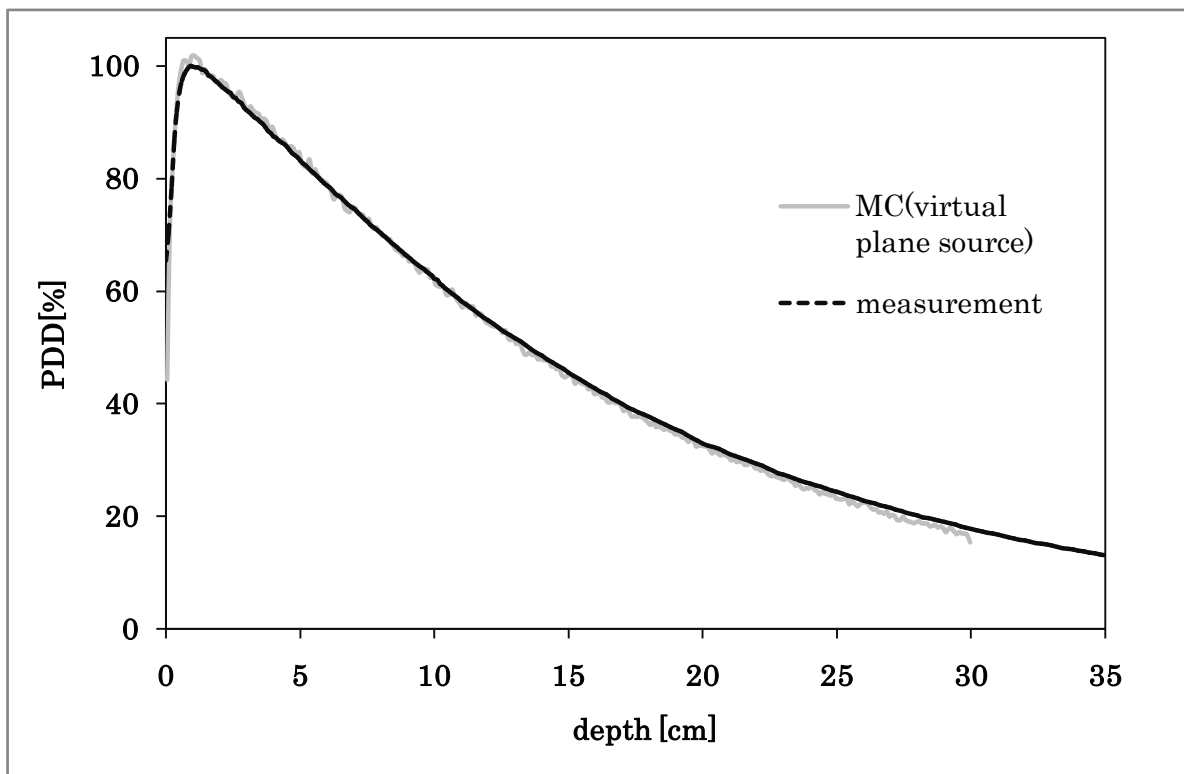
Figure.4: the measured PDD and calculated PDD by MC
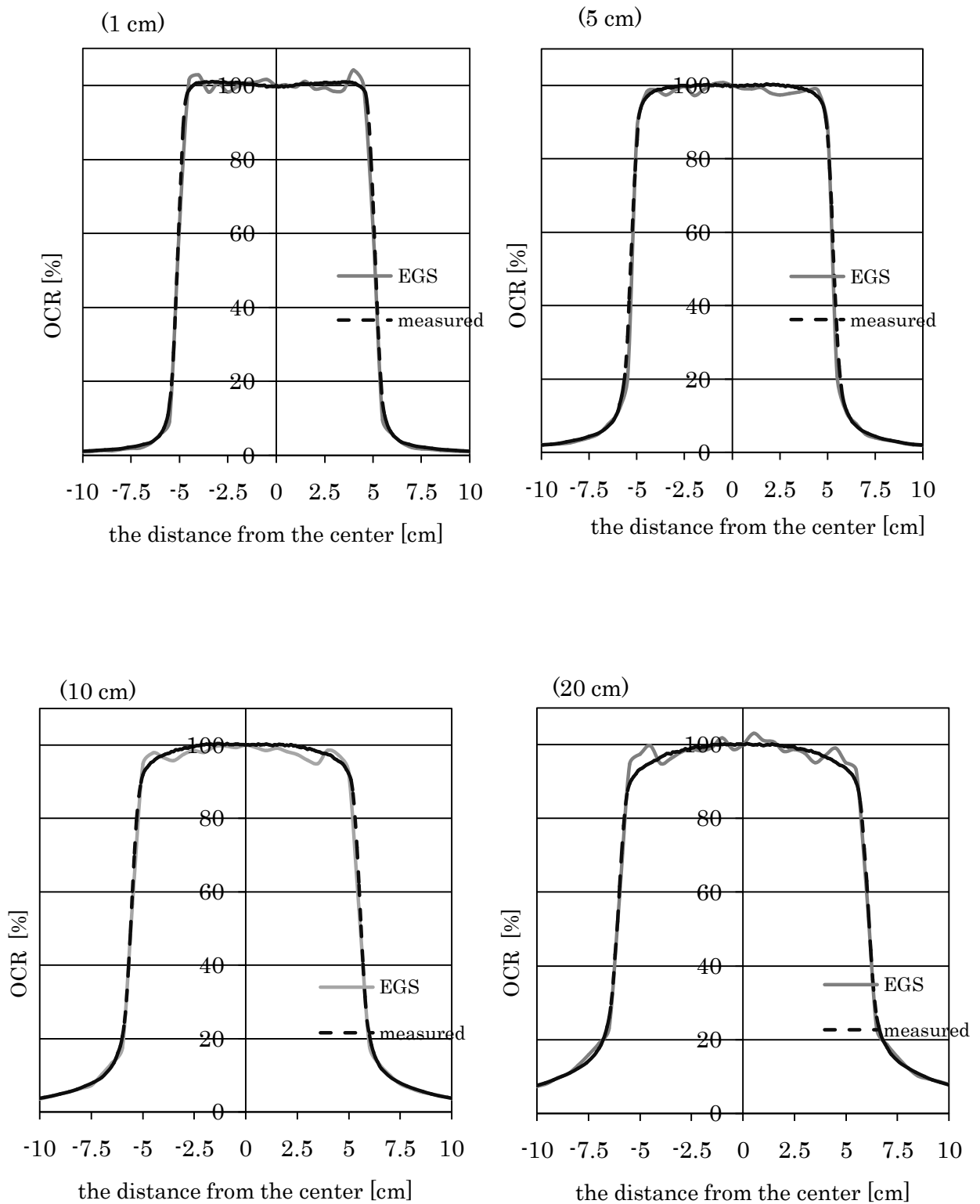
Figure.5: the measured and calculated OCR at each depth

Investigation of the dose distribution in the inhomogenous phantom simulated lung tumor

K. Ota, T. Matsunaga[1], K. Habara[2], K. Yasui[3], K. Aoyama[4], J. Maruchi[5], T. Shimozato, Y. Obata, and M. Komori

Nagoya University，Graduate School of Medicine，Department of Radiological Technology 1-1-20

Daikou-Minami，Higashi-ku，Nagoya，Aichi，Japan

[1]*Seirei Hamamatsu General Hospital*

[2]*Hiroshima Red Cross Hospital & Atomic-bomb Survivors Hospital*

[3]*Health ＆ Welfare Bureau，City of Nagoya*

[4]*Ichinomiya municipal Hospital*

[5]*Nagoya University, school of Health Sciences*

E-mail : ota.kenji@c.mbox.nagoya-u.ac.jp

Abstract

The scattering model of the electrons and photons of a radiation treatment planning system (RTPS) has been generally created in the water phantom with Monte Carlo (MC) simulation. The inhomogeneity correction has been made in each way of the RTPS using CT values. A phantom simulated a tumor in the lung tissue was used in the computational geometry of the inhomogenous region. We calculated the dose distributions of the RTPS and the MC simulation. The result by Pencil Beam Convolution (PBC) algorithm showed no re-build up in the different material. The dose differences of relative dose curves on the central axis between the RTPS result by the Convolution / Superposion (SP) and the MC simulation were within 1.2 ％ at the re-build up part of the tumor and was up to 3.5 ％ at the lung tissue located behind tumor. The result by the Anisotropic Analytical Algorithm (AAA) underestimated 2.4 % in average and up to 3.1％ at the wide region of inhomogenous phantom.

1. Introduction

Each of dose calculation algorithm of a radiation treatment planning system (RTPS) calculate the primary and the scatter components. The scatter components model is obtained from the dose distribution in a water phantom with Monte Carlo (MC) simulation. The inhomogeneity correction of the RTPS varys degrees of scattering according to the different electron density from the water. The inhomogeneity correction methods differ depending on the dose calculation algorithms provided by many companies. In this study, we investigated dose distributions and depth dose curves in the inhomogenous phantom calculated by various dose calculation algorithms and MC simulation.

2. Materials and Methods

2.1 Computational structures and materials

The RTPS calculations and the MC simulations were performed for field sizes of 4×4, 5×5, and 7×7 cm^2 with a constant source-to-surface distance (SSD) of 89 cm for 4 and 10 MV X-ray beam from Clinac21EX (Varian Medical Systems .Inc) linear accelerator (RTPS calculations), and 4 and 10 MV X-ray spectrum source of Varian (MC simulations) [1] respectively. All doses were normalized at the depth of 11 cm on the central axis.

The phantom for the RTPS calculations and the MC simulations was made of PMMA, cork, and polystyrene. The components of each materials are detailed in Table 1. The size and structure are showed in Fig.1.

2.2 RTPS calculations

Eclipse (Varian Medical Systems .Inc) and XiO (ELEKTA .Inc) were adopted for commercial RTPSs. Pencil Beam Convolution (PBC) algorithm, Anisotropic Analytical Algorithm (AAA) (Eclipse), and Convolution / Superposition (SP) (XiO) were applied for the calculation algorithms. Calculation voxel sizes were $0.1 \times 0.2 \times 0.1$ cm^3 (XiO) and $0.25 \times 0.2 \times 0.25$ cm^3 (Eclipse). The calculated dose distributions are showed in Fig.2 (a) – (f). In addition, relative depth dose curves obtained from along the central axis are drown in Fig.3 (a) - (f), the dose profiles at the depth of 11 cm for field size of 7×7 cm^2 are indicated in Fig.4.

2.3 MC simulations

EGS5 [2] code system was used for the MC simulation. The cut-off energies of electron (ECUT) and photon (PCUT) in all simulations were set to 0.521 MeV and 0.01 MeV, respectively. Calculation voxel size was $0.2 \times 0.2 \times 0.1$ cm^3. In order to obtain relative doses, deposited energies at each cubic coordinates boundary space of interest divided by the mass density of each material were computed and normalized at the point of center of phantoms. MC simulated dose distributions are showed in Fig.2 (a) – (f). Also, the relative depth dose curves are plotted in Fig.3 (a) - (f), the dose profiles at depth of 11 cm for field size of 7×7 cm^2 are indicated in Fig.4. Statistical uncertainties were less than 0.6 % at all data acquisition grids.

2.4 Back scatter and mean energy calculation

When back scattering and the mean energy from the polystyrene are calculated for 10 MV and field sizes of 4×4, 7×7 cm^2, the polystyrene was not structured by 4 cm diameter sphere but $4 \times 4 \times 4$ cm^3 cube. The mean energy $\overline{E}$ is calculated as follows [3]

$$\overline{E}(d) = \frac{\sum_{i=E\min}^{E\max} \Phi(E_i(d)) \cdot E_i(d)}{\sum_{i=E\min}^{E\max} \Phi(E_i(d))}$$

where E_i expresses each energy bin divided to 0.01 MeV, $\Phi(E_i)$ expresses the fluence per E_i, and d is depth. The mean energy transition is showed in Fig. 5. The back scatter from the polystyrene to the cork in proportion to the total dose was analyzed by the latch method [2].

3.   Results and Discussions

3.1 Comparison of dose distributions by RTPS and MC

Fig.2 (a)-(f) show the dose distributions for each energy and each field size, the left side of which shows the MC simulation and the right side shows each RTPS. The polystyrene is located in the central circular area. Fig.3 (a)-(f) show the relative depth dose curves at central axis.

For PBC, the relative dose differences (DD) range from -1.1 to 1.6 % at 4 MV in all depth (Fig.3 (a) - (c)), where the relative DD = ((RTPS $_{dose}$ − MC $_{dose}$) / MC $_{dose}$) × 100 (%). And the relative DD are up to 16.9 % in all depth at 10 MV (Fig.3 (d)). PBC curves show no re-build up portion in the materials of different compositons. Since the PBC algorithm does not take account the changing degree of secondary electron scattering by the different electron density of materials.

For AAA, the relative DD range from -3.6 to -1.5 % (average -2.4 %) in front of the polystyrene for 4 MV X-ray (Fig.3 (a)) and from -3.1 to -1.8 % (average -2.4 %) in front of the polystyrene for 10 MV X-ray (Fig.3 (d)). AAA curves indicate the steep reduction of dose in the polystyrene position. The AAA dose is 0.67 % higher than the MC dose at the cork in front of the polystyrene, whereas the AAA dose is 4.8 % lower than the MC dose at the cork in back of the polystyrene. So the AAA algorithm showes excessive changes between different materials and underestimated the dose in the cork comparing with the MC simulation.

For SP, the relative DD range from 0.0 to 1.8 % (average 0.7 ％) in all depth for 4 MV X-ray, field size of 7 × 7 cm^2 and indicates the most difference of 4 MV (Fig.3 (c)). The relative DD are up to 3.5 % at the posterior half of the polystyrene for 10 MV X-ray, field size of 4 × 4 cm^2 and indicate the most difference of 10 MV (Fig.3 (f)). The better accuracy of the dose difference is found for the larger field size for 10 MV. The SP provides the best accurate calculation among the three algorithms.

Fig.4 shows all dose profiles at depth of 11cm. Both AAA and SP dose profiles have no much dose differences. It is difficult to determine the relative merits of these algorithms.

3.2 Transition of the mean energy and the back scattering evaluation from polystyrene

Fig.5 shows the transition of the mean energy.   The mean energy starts reducing 1 cm from in front of the polystyrene. The mean energy reduction and reduction rate from the depth of 8 to 9 cm are 18.0 keV and 0.64 % for the field size of 4 × 4 cm^2, and 24.5 keV and 0.92 % for the field size of 7 × 7 cm^2. Also, the back scatters to 2 mm in front of the polystyrene in proportion to the total dose are 8 % for the field size of 4 × 4 cm^2 and 10 % for the field size of 7 × 7 cm^2. Therefore low energy components are increased to the cork in front of the polystyrene for the larger the field size. And the DD for the different materials result less difference for 10MV (Fig.3 (d) − (f)).

4. Conclusions

The overall evaluation revealed that the SP dose distribution was closest to MC simulation. The AAA dose distribution was also close to MC simulation, but the AAA algorithm showed excessive changes of energy absorbtion between different materials in comparison with MC simulation. As a result, the dose distribution indicated the tendency to good agreements, but the dose of the cork region was underestimated by the normalized point. The PBC algorithm didn't calculate acculately lateral and back scatters. It was not much sensitive to the re-build up and the field size change.

References

1) D.Sheikh-Bagheri and D.W.O. Rogers,"Monte Carlo calculation of nine megavoltage photon beam spectra using the BEAM code," Med. Phys. **29**, 391-402, (2002).

2) H. Hirayama, Y. Namito, A. F. Bielajew, S. J. Wilderman, and W. R. Nelson, "The EGS5 Code System, 2005 - 8, SLAC - R - 730," Radiation Science Center Advanced Research Laboratory, High Energy Accelerator Research Organization (KEK), Stanford Linear Accelerator Center, Stanford, CA, (2005).

3) Faiz. M. Khan, "The Physics of Radiation Therapy, 4th Edition," P. 92 (2010).

Table 1. Element composition and mass density

		PMMA	Cork	Polystyrene
Composition	H	53.3	6.78	50.0
(%)	C	33.3	53.87	50.0
	O	13.3	39.35	
Mass density(g $\cdot$ cm^{-3})		1.06	0.315	0.96
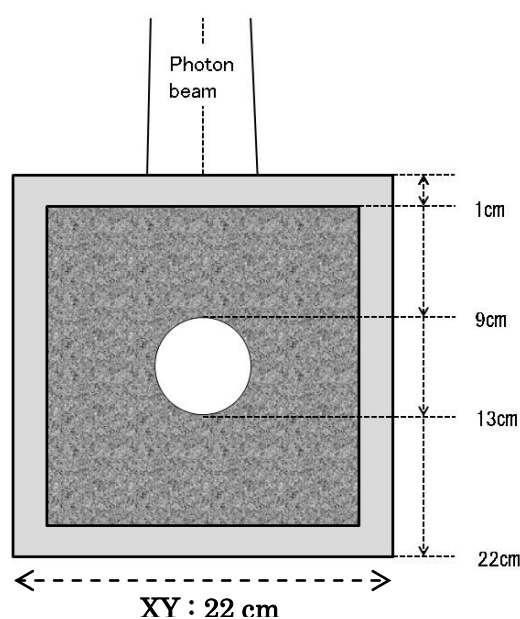
Fig.1. Cross sectional diagram of the phantom used in calculation.
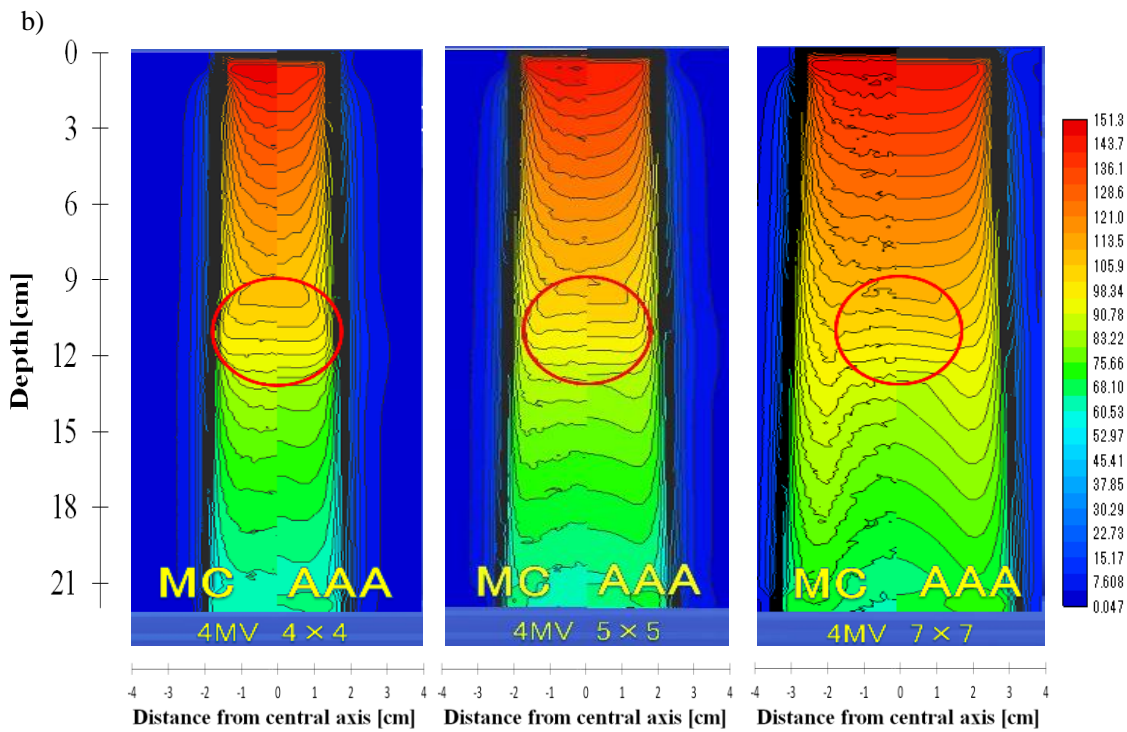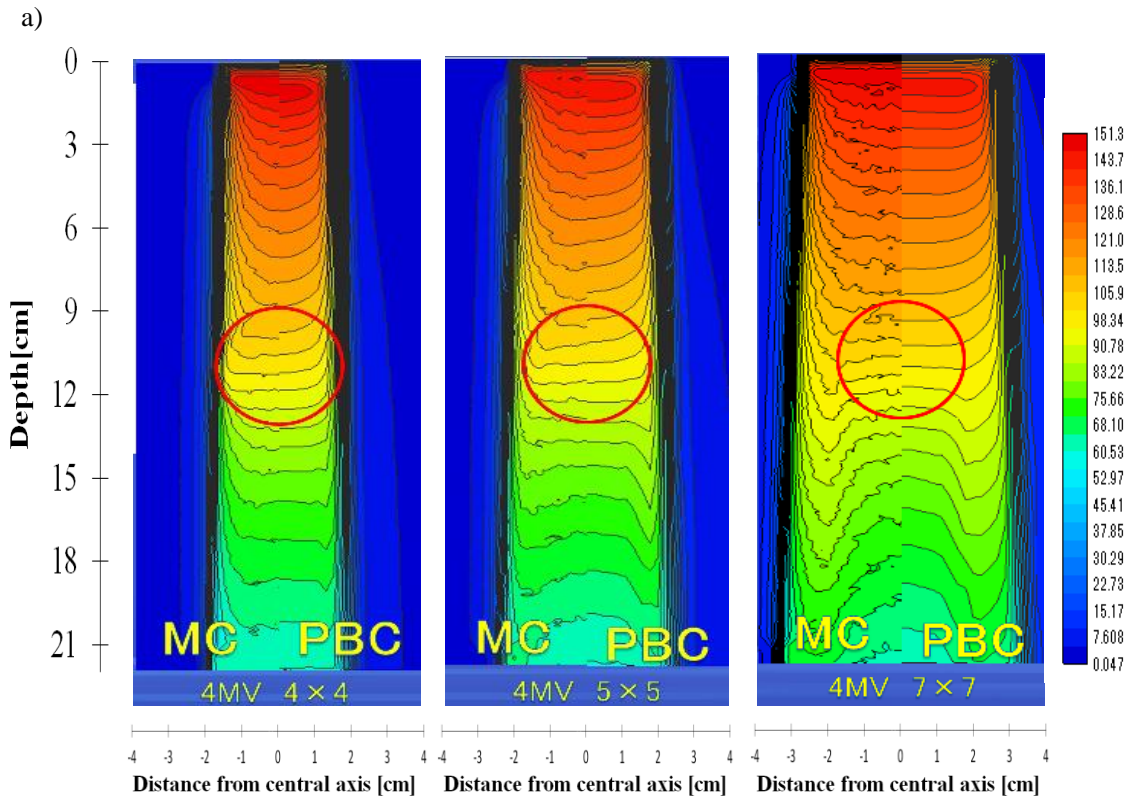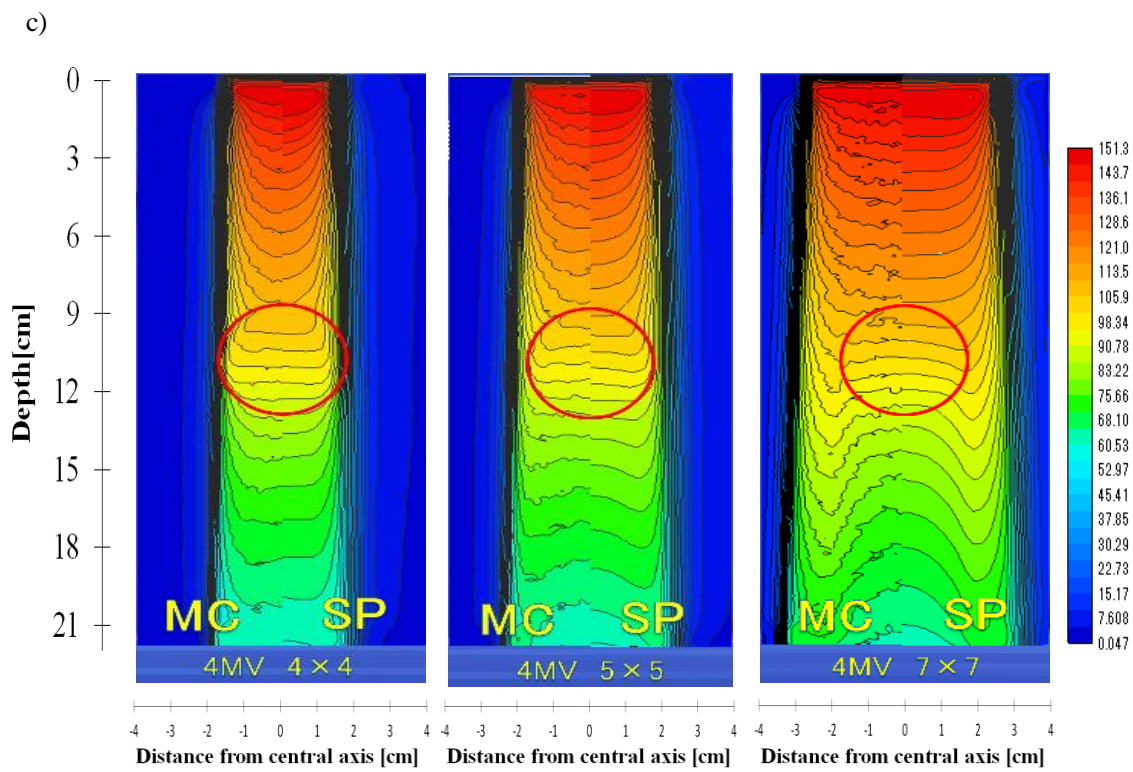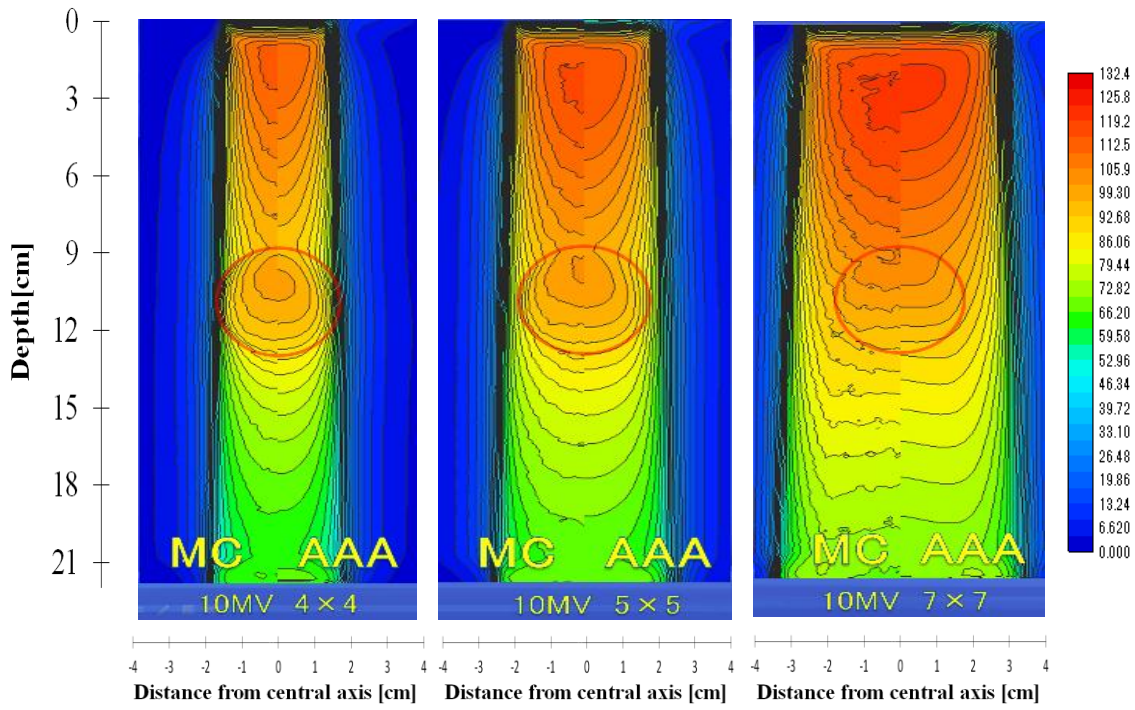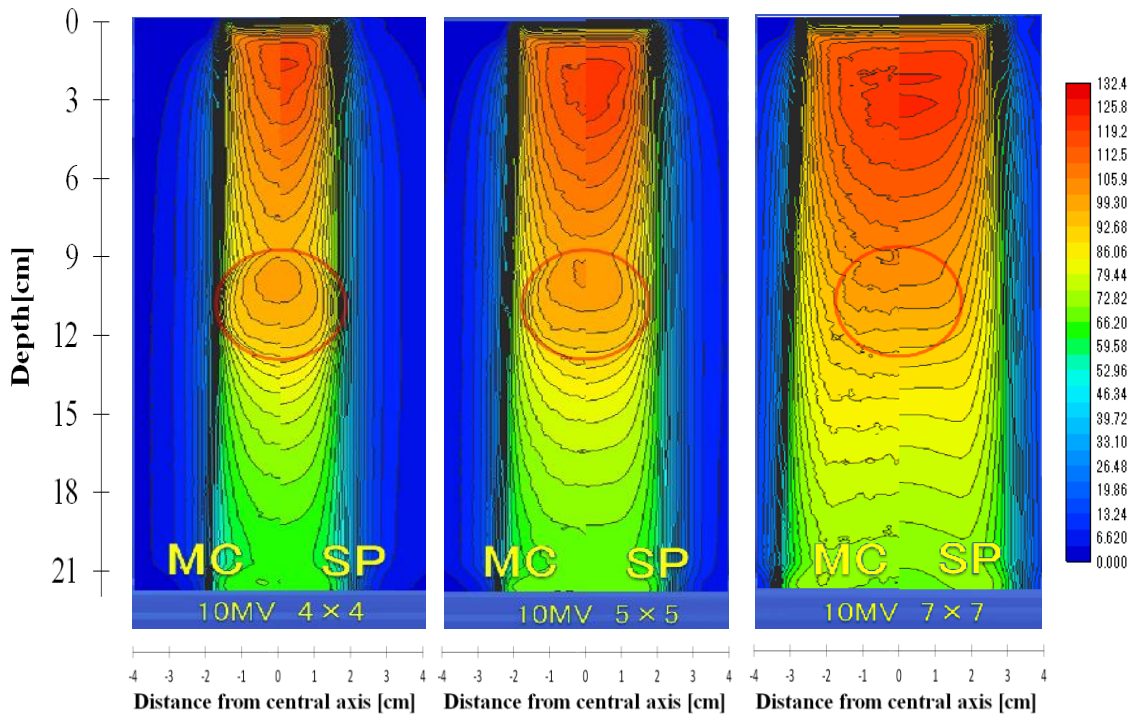
Fig. 2 (a) - (f) . Calculated dose distributions using MC simulation and each RTPS.

c)

d)

54

e)

f)

55
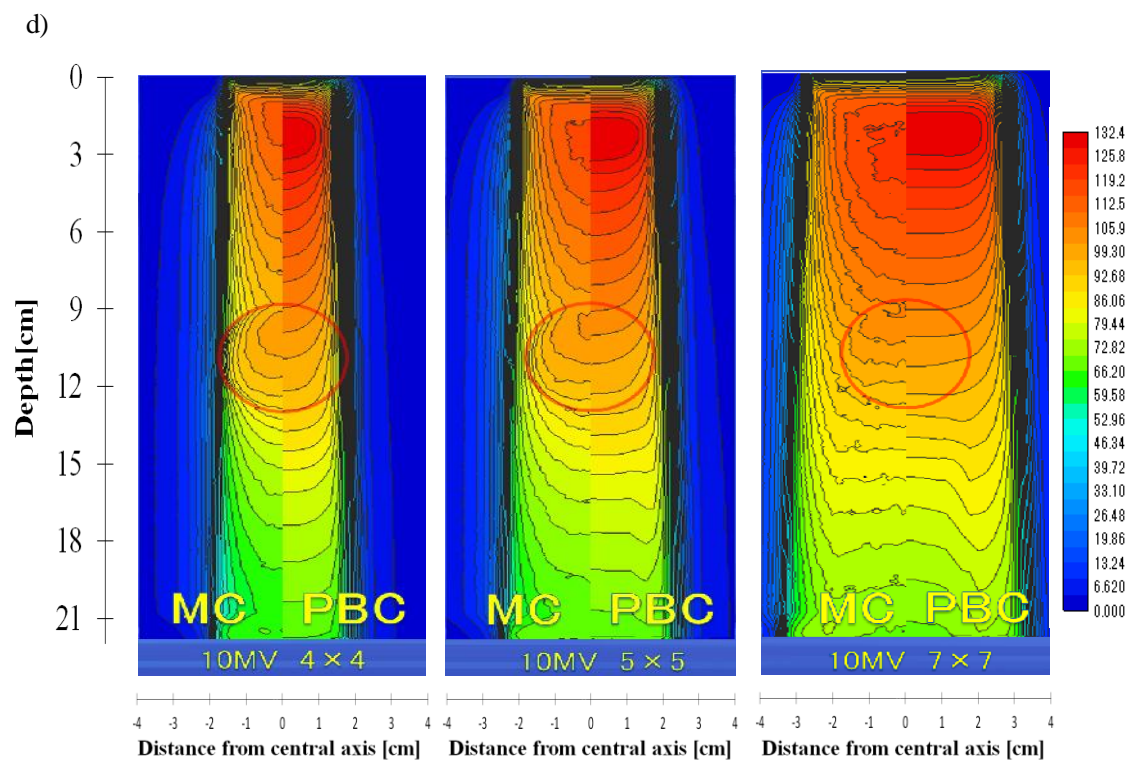
a) Energy : 4MV, Field size : 4×4 cm²
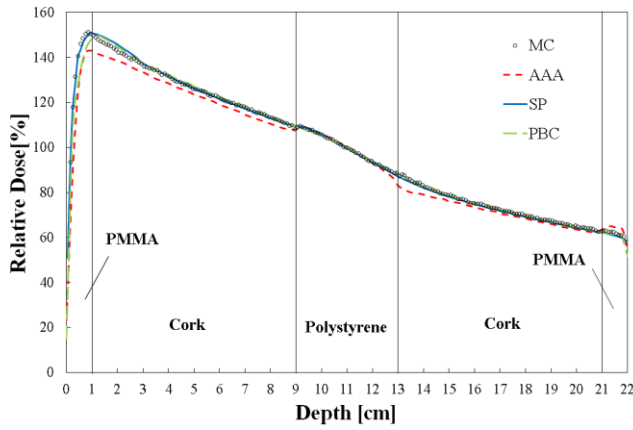
b) Energy : 4MV, Field size : 5×5 cm²
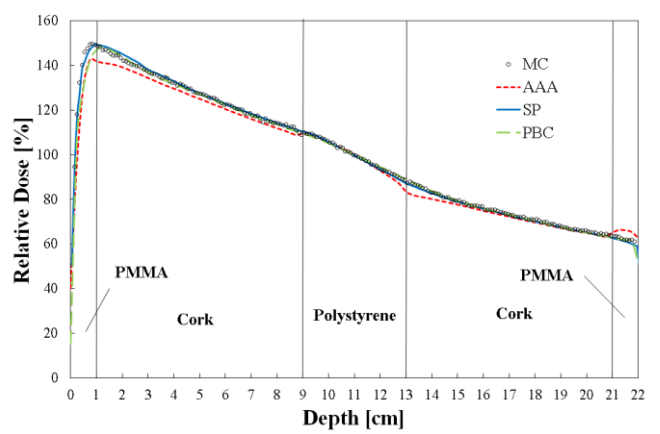
c) Energy : 4MV, Field size : 7×7 cm²
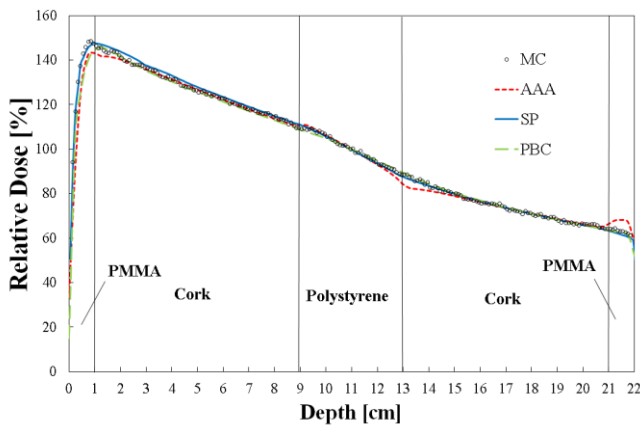
d) Energy : 10MV, Field size : 4×4 cm²
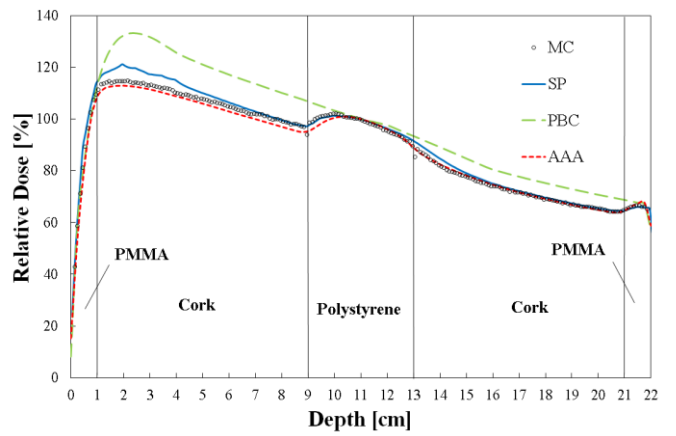
e) Energy : 10 MV, Field size : 5×5 cm²
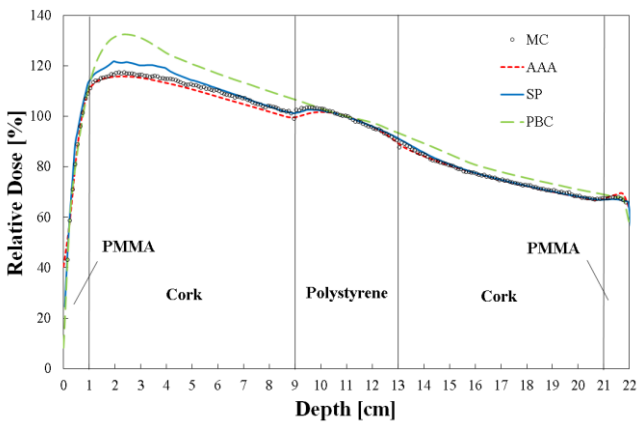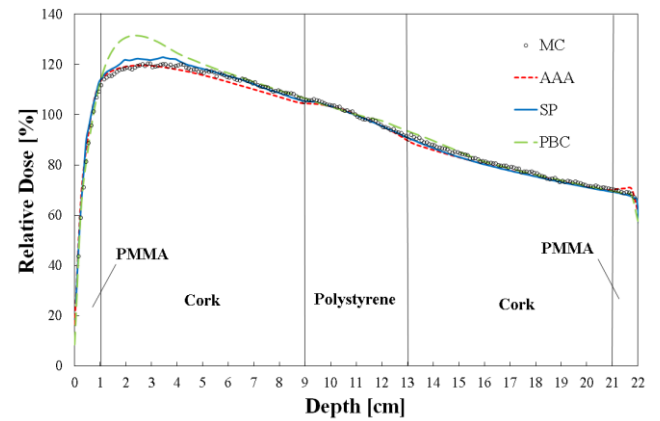
f) Energy : 10 MV, Field size : 7×7 cm²

Fig.3 (a) – (f). Relative depth dose curves for each energy and each field size with MC simulation and RTPS calculations.
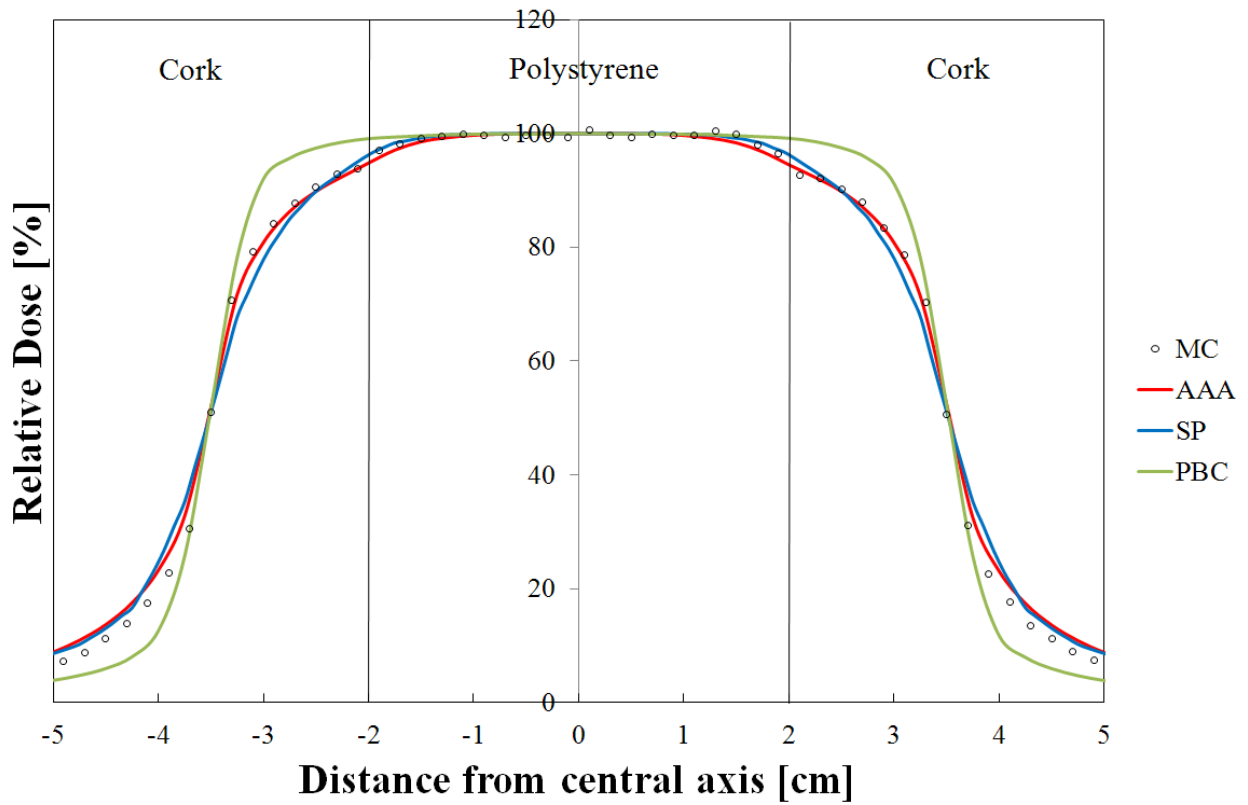
Fig.4. Lateral dose profiles for 10 MV and field size of 7×7 cm^2 with MC and RTPS calculations.

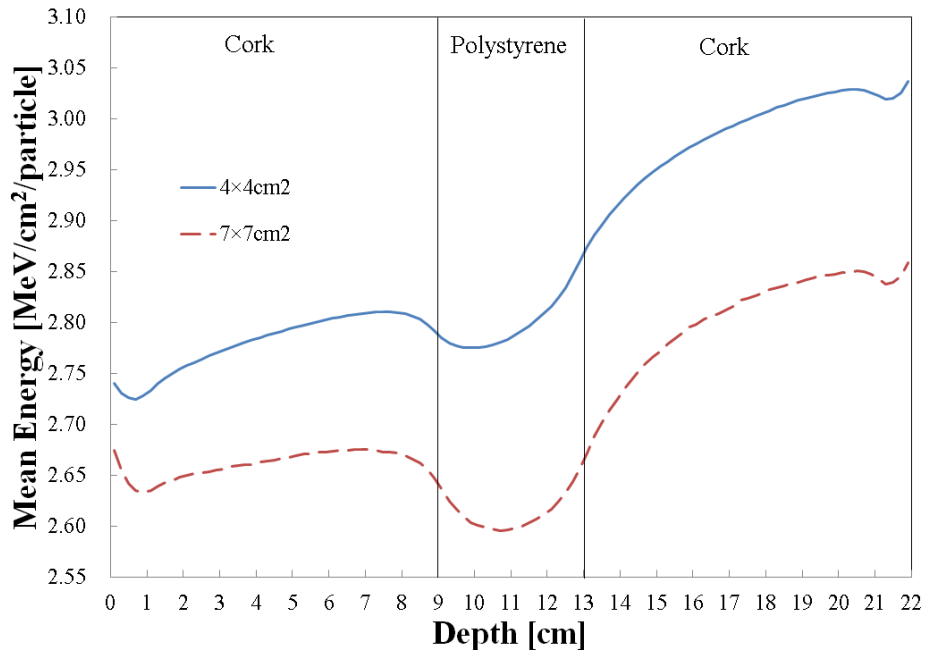Fig.5. The mean energy transition for 10 MV and field sizes of 4×4 and 7×7 cm^2.

Detail analysis of dose distribution in phantom in X-ray CT using EGS5

T. Haba[1], S. Koyama[1]

[1] *Department of Radiological Technology, Graduate School of Medicine, Nagoya University*
1-1-20 Daiko-Minami, Higashi-ku, Nagoya, Japan
e-mail: haba.tomonobu@f.mbox.nagoya-u.ac.jp

Abstract

In this study, the dose distribution in phantom in 320 detector row cone beam CT (CBCT) was analyzed in detail using EGS5. Our results show that maximum dose position is 18 mm depth from the phantom surface, and peak deposit energy is 11 % higher than the phantom surface dose. In the 320 detector row CBCT, peripheral position dose is underestimated using conventional weighted CTDI estimation method.

1. Introduction

X-ray computed tomography (CT) scanners have remarkable progress over the past few years. Quite recently, 160 mm beamwidth, 320 detector row, cone beam CT (320 detector row CBCT) has been used in clinical examination. In 320 detector row CBCT, dose distribution in phantom is complicated because its wide x-ray beamwidth causes more scattering of x-ray. The understanding of detailed dose distribution in phantom is useful for dose estimation in CT scanner. However, the measurement of dose distribution in phantom for kilovoltage x-ray beams is difficult because there are problems related to large gradients in the dose distribution and the large energy dependence of most dosimetry systems [1]. In this study, we calculated dose distribution in CT dose index (CTDI) phantom along the axis perpendicular to the axis of rotation of the x-ray source in 320 detector row CBCT using EGS5.

2. Materials and Methods

2.1 Conformity of EGS5 with measurement

To consider the conformity of EGS5 with measurement, we calculated and measured $CTDI_{100}$ in a Non-helical X-ray CT unit TCT-300 (Toshiba Medical Systems, Tochigi, Japan). The x-ray tube voltage was 120 kV, and Source Center Distance (SCD) was 600 mm. PMMA cylindrical phantom of 300 mm diameter and 150 mm length and CT ionization chamber of 100 mm length were used. In the phantom, there were five cylindrical cavities in different depth along the cylinder axis to insert the CT chamber; The depths were 11, 59, 81, 115, and 150 mm from the phantom surface.

Fig.1 shows measurement geometry. The center of the phantom was placed in the isocenter of the CT unit. The phantom was supported using wooden blocks and the bed was removed from scan area. This is because it is difficult to incorporate the effect of x-ray scattering and attenuation of CT patient bed in the simulation. In addition, it is also difficult to incorporate the effect of x-ray tube rotation overlapping in the simulation because the overlapping angle has not been disclosed. Therefore, a scanogram mode (non-rotating mode) which had 2 mm slice thickness in TCT-300 was used. To be the same as a full scan, the phantom was rotated by 10 degrees up to full circle in a counterclockwise direction and each dose was integrated into a cylindrical cavity.

In EGS5, the simulation geometry was the same as the above measurement geometry. The number of photon was 1.44 billion. Fractional Standard Deviation (FSD) in the center of the phantom was less than 3.0 % to reduce statistical error. Energy spectrums as x-ray source along the fan beam of the CT were generated by Tucker's formula based on AL HVL measured on each angle [2]. The effect of the beam shaping filter was incorporated into the simulation.

2.2 PDD calculated by EGS5 in CBCT

Percentage depth dose (PDD) along the axis passing through the isocenter in a direction perpendicular to cylinder axis on the phantom cross section in 320 detector row CBCT was calculated using EGS5. This CBCT geometry was applied to previous TCT-300 geometry (The x-ray tube voltage was 120 kV, and SCD was 600 mm), but the slice thickness was only changed from 2 mm to 160 mm. **Fig.2** shows CBCT geometry in EGS5. The x-y coordinate plane is parallel to the transverse axis, and the z coordinate axis (z axis) is parallel to the longitudinal axis of cylindrical phantom. The x coordinate axis (x axis) is horizontal to the floor, and the y coordinate axis (y axis) is perpendicular to the floor. Phantom was PMMA cylinder of 320 mm diameter and 600 mm length. The number of photon was 3.6 billion. FSD in the center of the phantom was less than 1.0 % to reduce statistical error. In this condition, one rotating scan was performed.

We calculated PDD along the y axis pass through the isocenter on the phantom cross section. PDD was calculated per 1.0 mm depth. The size of calculation region was 10.0 mm (x), 1.0 mm (y), and 100 mm or 300 mm (z). The size of z direction was on the assumption of 100 mm long or 300 mm long CT chamber. Energy deposition by primary x-ray and Compton scatter x-ray was accounted for separately.

3. Results

3.1 Conformity of EGS5 with measurement

We checked the conformity of EGS5 with measurement (**Table 1**). The depth showed the distance from the phantom surface to the center of CT chamber. Each depth dose was normalized to 11 mm depth dose in the EGS5 and the measurement.

Percent Average Error (PAE) was calculated. PAE is given as follows:

$$PAE = \frac{D_m - D_e}{D_m} \times 100 \quad [\%]$$

where D_m was the normalized measured dose, D_e was the normalized calculated dose.

In the **Table 1**, PAE was within ±2.4 % in all depth.

3.2 PDD calculated by EGS5 in CBCT

Fig.3 shows that PDD which was calculated on the assumption of 100 mm long CT chamber. **Fig.4** shows that PDD which was calculated on the assumption of 300 mm long CT chamber. In both **Fig.3** and **Fig.4**, continuous line indicates total deposition energy (primary and Compton scatter); broken line indicates deposition energy which only came from Compton scattering component of x-ray; and dotted line indicates deposition energy which came from primary component of x-ray. The depth indicated the distance from the upper surface to the lower surface of the phantom. Each deposition energy was normalized to the total deposition energy in the surface region.

In **Fig.3**, peak dose of total deposit energy was 11.0 % higher than phantom surface dose. The position of maximum dose was 18.0 mm depth from the phantom surface. In Compton scatter component of x-ray, maximum dose was 17.0 % higher than the phantom surface dose. The position of maximum dose was 25.0 mm from the surface. In primary component of x-ray, the position of peak dose was on the phantom surface.

In **Fig.4**, peak dose of total deposit energy was 22.0 % higher than phantom surface dose. The position of maximum dose was 30.0 mm depth from the phantom surface. In Compton scatter component of x-ray, maximum dose

was 33.0 % higher than the phantom surface dose. The position of maximum dose was 40.0 mm from the surface.

4.　Discussion

In **Table 1**, PAE is within ±2.4 % in all depth from the phantom surface. This result indicates that there is a good agreement between EGS5 and measurement.

In **Fig.3** and **Fig.4**, detail analysis of energy deposition finds that Compton scattering is contributed largely to maximum dose position shifting. The effect of maximum dose position shifting is greater with the 300 mm long CT chamber than with the 100 mm long CT chamber. This is because the 300 mm length along the direction of z axis covers wide x-ray beamwidth in 320 detector row CBCT and is more deposited Compton scatter component of x-rays. Our results showed that, in the existing CTDI estimation of CBCT, peripheral position of 10 mm depth was different to maximum dose position. We considered that this effect is very important for CTDI estimation. In the International Electrotechnical Commission (IEC) standard, dose estimation in CT scanner is now performing using $CTDI_{100}$ which is derived from measurements of 320 mm diameter, 150 mm long CTDI phantom and 100 mm long CT chamber. In 320 detector row CBCT, however, Geleijns et al. said that $CTDI_{100}$ underestimated $CTDI_{300}$ ($CTDI_{300}$ is derived from measurements of 350 mm long CTDI phantom and 300 mm CT chamber [3,4].) and Mori et al. said that the length of both the CTDI phantom and CT chamber needed to be more than 300 mm for dosimetry of CBCT [5]. In this research, we also thought that it is better to measure CTDI using 300mm CT chamber because maximum dose position shifting is remarkable. The measurement using 300 mm CT chamber is, however, impractical in clinical quality assurance since it is difficult to develop long ionization chamber which has uniform sensitivity and to handle the large and heavy PMMA phantom. Along with the popularization of 320 detector row CBCT, dosimetry of x-ray CT will become even more complex.

5.　Conclusions

In this research, we calculated PDD using EGS5 in order to analyze the dose distribution in the CTDI phantom in 320 detector row CBCT. In previous research, the need of long length CT chamber and CTDI phantom was suggested in CBCT. We thought that it is also important to consider about the measurement depth of peripheral positions in CTDI phantom in 320 detector row CBCT.

References

1)　C L Fletcher, J A Mills, "An assessment of GafChromic film for measuring 50 kV and 100 kV percentage depth dose curves", Phys.Med.Biol. 53 (2008) N209-N218.
2)　Douglas M. Tucker, "Semiempirical model for generating tungsten target x-ray spectra", Med.Phys. 18 (1991)
3)　J Geleijns, M S Artells, P W de Bruin, R Matter, Y Muramatsu, M F McNitt-Gray, "Computed tomography dose assessment for a 160 mm wide, 320 detector row, cone beam CT scanner", Phys.Med.Biol. 10 (2009) 3141-3159.
4)　T B Shope, R M Gagne, G C Johnson, "A method for describing the dose delivered by transmission x-ray computed tomography", Med.Phys. 8 (1981).
5)　S Mori, M Endo, K Nishizawa, T Tsunoo, T Aoyama, H Fujiwara, K Murase, "Enlarged longitudinal dose profiles in cone-beam CT and the need for modified dosimetry", Med.Phys. 32 (2005).
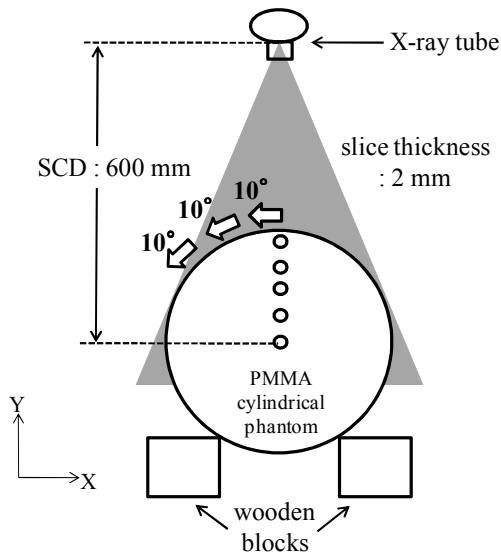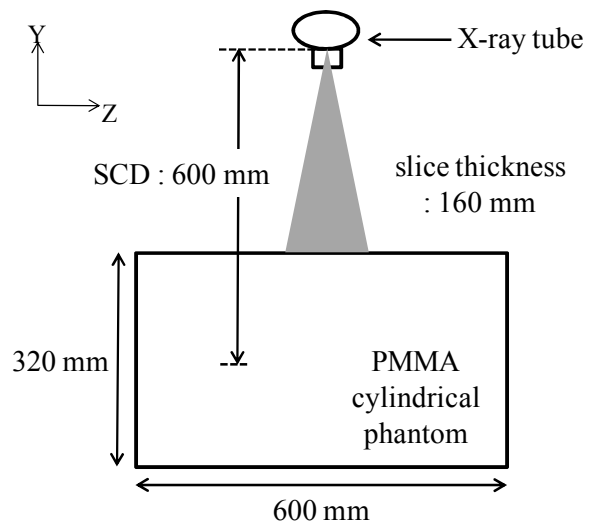
Fig.1   measurement geometry

Fig.2   CBCT geometry in EGS5

Table 1   the conformity of EGS5 with measurement

depth from the phantom surface [mm]	normalized dose		PAE [%]
	EGS5 (De)	measurement (Dm)	
11	1.0	1.0	0.0
59	0.94	0.93	-1.5
81	0.84	0.85	2.2
115	0.77	0.77	-0.3
150	0.71	0.73	2.4
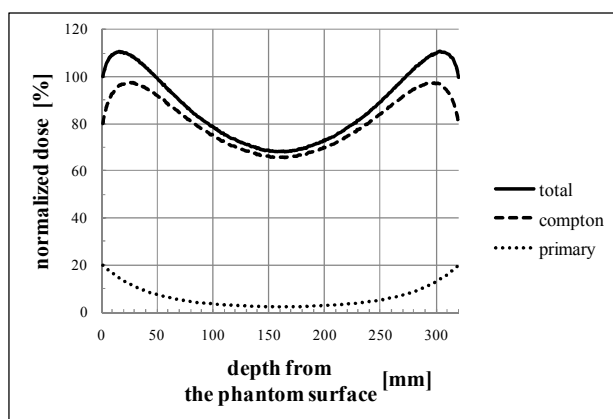
Fig.3   PDD which was calculated on the assumption of 100 mm CT chamber
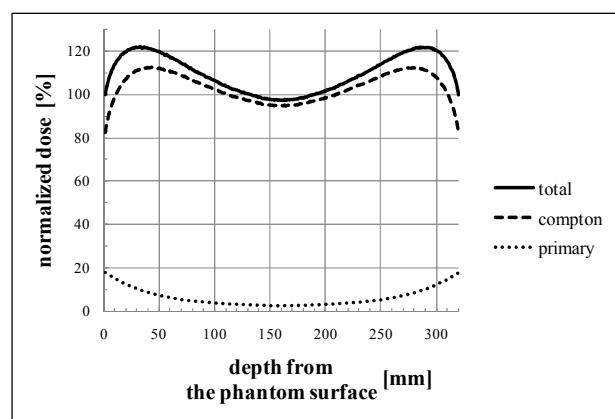
Fig.4   PDD which was calculated on the assumption of 300 mm CT chamber

IN-PHANTOM BEAM QUALITY CHANGE IN X-RAY CT : DETAILED ANALYSIS USING EGS5

S. KONDO[1], S.KOYAMA[1]

[1]*Department of Radiological Technology, Graduate School of Medicine, Nagoya University*
1-1-20 Daiko-Minami, Higashi-ku, Nagoya 461-8673, Japan
e-mail: kondo.shimpei@e.mbox.nagoya-u.ac.jp

Abstract

The aim of this research was to analyze x-ray energy spectrum and effective energy in phantom undergoing x-ray CT scan using Electron Gamma Shower 5 Monte Carlo simulation code. In this calculation code, radiation source of X-ray CT (TCT-300; Toshiba Medical, Tochigi, Japan) was rotated 360 degrees at intervals of 1degree around a phantom, which was water cylinder of 32cm diameter. X-ray CT is generally equipped beam-shaping filter in front of the x-ray tube radiation window. For making x-ray CT simulation more concrete, the effect of beam-shaping filter was incorporated in simulation code. Photon number was counted with respect to each energy bin in small discs in a cylindrical water phantom. That is used for in-phantom x-ray spectrum, and effective energy was calculated from these spectrums. In-phantom effective energy was 55.92 keV at the depth of 1 cm (raised by 3.61 % compared to effective energy of incident x-rays), and was 55.97 keV at the depth of 16 cm (raised by 3.65 %). Little difference existed between incident and in-phantom effective energy. In phantom, effective energy in each depth from the phantom surface also had little difference.

1. Introduction

X-ray entered into a phantom is absorbed and scattered. In-phantom x-ray spectrum has the potential to differ from incident x-ray spectrum when continuous x-ray entered into object. We have small semiconductor dosimeters, which are very useful to measure doses in phantom. The semiconductor dosimeters have large energy dependence and, output values of them are influenced by changes in beam quality. It is important to measure x-ray energy spectrum and effective energy in phantom to know appropriate calibration factor, because calibration factor for the semiconductor dosimeters is required to estimate correct absorbed dose. It is, however, practically difficult to measure x-ray energy spectrum with spectrometer or half-value-layer with ionization chamber in phantom.

In this study, in-phantom x-ray energy spectrum and effective energy were analyzed by using Monte Carlo simulation which has the advantage of being able to calculate energy spectrum in difficult measurement situation.

2. Materials and Methods

X-ray energy spectrum and effective energy in a phantom undergoing x-ray CT scan were analyzed by Electron Gamma Shower 5 (EGS5) Monte Carlo simulation code.

2.1 Monte Carlo Simulation Geometry

X-ray-focus isocenter distance was 60 cm. The cylindrical phantom consisted of water, 32 cm in diameter and 20 cm in length. Twenty five small water discs of 1 cm diameter were put inside the phantom, along x (horizontal) and y (vertical) axis of an axial plane at 0.2 cm intervals. Locations of each of four small discs nearest the phantom sueface

were placed at 0.7, 1.0, 1.3, and 1.6 cm from the phantom surface. This geometry was created with HOWFAR, and in this simulation code, subroutine for determining distance from a particle to cylinder wall (subroutine cylndr and subroutine cyl2) was rewritten to move cylinder axis on x-y plane arbitrarily. Central axis of cylinder usually was put on z axis and unmoving on x-y plane. Figure 1 shows geometry of this calculation and Figure 2 shows geometry of the cylindrical water phantom. X-ray CT has a fan beam, and the form of incident fan beam was incorporated in this calculation. Focus of x-ray tube was rotated 360 degrees at intervals of 1 degree around the phantom. The fan beam angle was 38 degrees and beam width was 0.5 cm.

2.2 Beam-shaping filter incorporated in simulation

X-ray CT is generally equipped with beam-shaping filter in front of the x-ray tube radiation window. By the beam-shaping filter, incident x-ray emitted from the target is adjusted to certain energy at CT detector after passing through object. Figure 3 indicates basic concept of beam-shaping filter and fan beam. Dose distribution and beam quality of x-rays originally emitted from the target are changed by the beam-shaping filter. For making x-ray CT simulation more concrete, the effect of beam-shaping filter that is contributed to x-ray attenuation and beam hardening, must be incorporated in incident fan beam. Figure 4 shows effective energy and dose distribution based on measurement data from x-ray CT (TCT-300; Toshiba Medical, Tochigi, Japan), which were incorporated in incident fan beam of our simulation code.

To take into account the effect of beam-shaping filter, incident fan beam was divided into 7 parts (0-4, 4-5, 5-6, 6-7, 7-8, 8-9, and 9-18 degrees) on the half side of the fan beam and seven different spectrums were used in each part. Effective energy of the energy spectrums were 54, 57, 59, 62, 64, 72, and 73 keV from the center part to the outer part, respectively, and the number of photon corresponding to dose distribution data was used in each degree (0-18 degrees) of fan beam.

2.3 Obtaining in-phantom spectrum and effective energy

The photons passing through the small discs inside the phantom were counted with respect to each energy bin, and those were used for calculating in-phantom energy spectrum and effective energy along x axis and y axis of an axial plane of the phantom. The total number of photon source was 1.44×10^{9}. Statistical error was less than 1.0 %.

3. Results

Figure 5 shows two x-ray spectrums with the lowest and highest effective energy (55.92 keV and 56.28 keV) in the phantom, and Figure 6 shows incident spectrum (effective energy:Eeff = 54 keV) and in-phantom energy spectrum with the highest effective energy.

Change of effective energy in the phantom is shown in Table 1 and Figure 7. The in-phantom effective energy is 55.92 keV at the depth of 1 cm (raised by 3.61 % compared to effective energy of the incident x-rays), and 55.97 keV at the depth of 16 cm (raised by 3.65 %). The spread between the lowest and highest in-phantom effective energy is less than 1 keV.

4. Discussion

One would think that continuous x-ray entered in phantom is absorbed, and beam quality becomes just harder. That is true in looking at only primary x-ray, but not true with the scattered x-ray. In this research, little difference existed between incident and in-phantom effective energy. In the phantom, effective energy in each depth from the phantom surface also has little difference. At the point of each depth, low energy component of the x-ray spectrum was reduced by beam hardening effect. In contrast, low energy x-rays generated in another area by Compton scattering were

absorbed to the point, and they were contributed to low energy component of the spectrum. The proportion between beam hardening and Compton scattering is important component of changing process of effective energy. Figure 8 shows change of in-phantom effective energy for each energy spectrum of seven parts of the fan beam. The graph indicates that in-phantom effective energy increase with increasing depth when incident x-ray effective energy is less than about 60 keV, decrease with increasing depth when incident x-ray effective energy is larger than about 60 keV. In the former, Compton scatter have a much greater impact on in-phantom x-ray spectrum than beam hardening effect, and the latter, opposite effect was observed.

In figure 7, the fluctuation of the effective energy was caused by the border of seven types of energy varied with the angle of fan beam. With using single type of energy spectrum for the fan beam, the fluctuation of the effective energy was not appeared.

X-ray CT also has complex factors of changing in-phantom effective energy, which are the effects of beam-shaping filter and rotating fan beam. Projected figure in each rotating angle is shown in Figure 9. Only the isocenter disc is exposed by single energy spectrum beam, but the other part discs are exposed by spectrum beams of 2 to 7.

As stated above, many factors of changing in-phantom effective energy exist in a complicated situation undergoing x-ray CT. The proportion of between beam hardening and Compton scattering was changed with depth of phantom surface and incident effective energy. Thus, in-phantom beam quality is not just harder.

Figure 10 shows the energy dependence of small semiconductor dosimeter owned Nagoya University. The difference of sensitivity of semiconductor dosimeter between incident and in-phantom effective energy is shown in Table 2. Relatively small changing of effective energy in phantom had little effect on calibration factor for the semiconductor dosimeter.

5. Conclusions

In-phantom x-ray spectrum and effective energy were analyzed by using Monte Carlo simulation (EGS5). Little difference exists between incident and in-phantom effective energy.

References

1) T. Aoyama, S. Koyama, C. Kawaura, "An in-phantom dosimetry system using pin silicon photodiode radiation sensors for measuring organ doses in x-ray CT and other diagnostic radiology," Med. Phys. **29**, 1504-1510 (2002)

2) R. Birch, M. Marshall, "Computation of Bremsstrahlung X-ray Spectra and Comparison with Spectra Measured with a Ge (Li) Detector," Phys Med Biol **24**, 505-517 (1979)

3) M. Tucker, G. Barnes, D. Chakraborty, "Semiempirical model for generating tungsten target x-ray spectra," Med. Phys.**18**, 211-218 (1991)

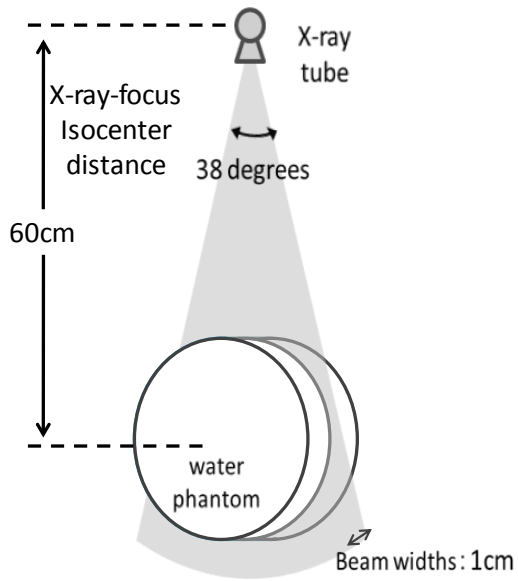4) J. Athertont, W. Huda, "CT doses in cylindrical phantoms," Phys Med Biol **40**, 891-911 (1995)

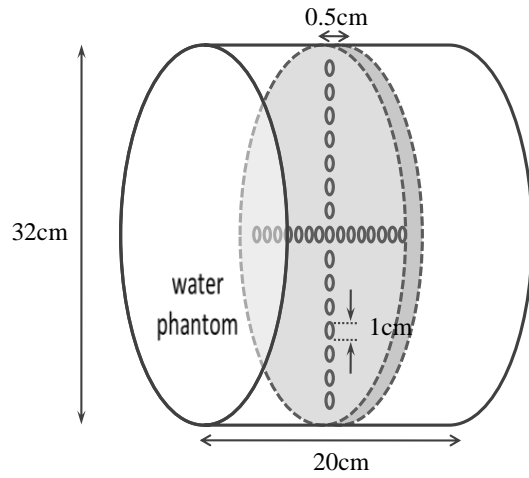**Figure 1.** Geometry of calculation code undergoing x-ray CT.

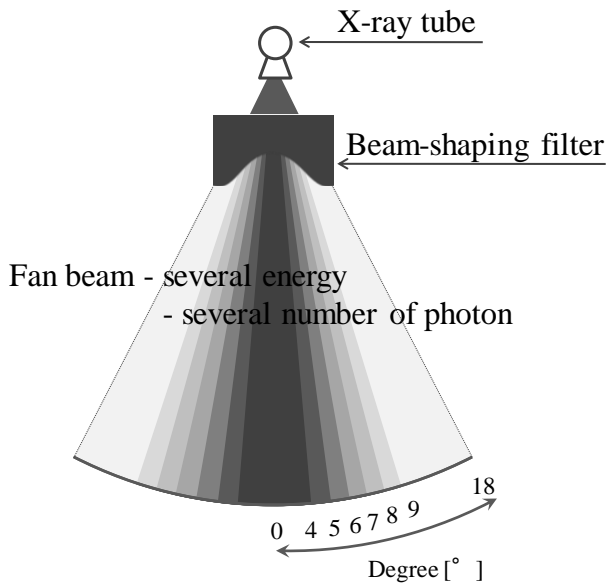**Figure 2.** Geometry of cylindrical water phantom.

Figure 3. Fan beam of x-ray CT after passing through beam-shaping filter.
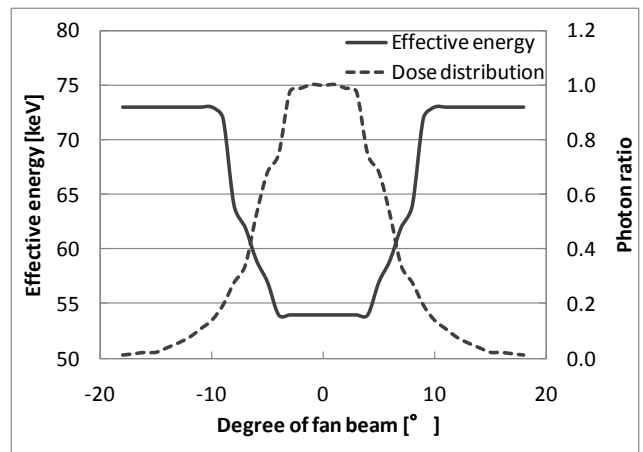

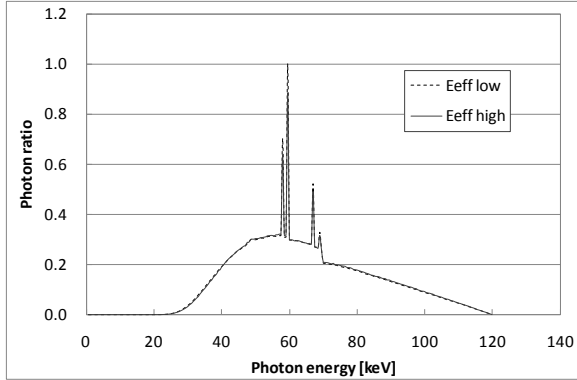**Figure 4.** Effective energy and dose distribution data.

Figure 5. Comparison of spectrums of lowest effective energy x-rays with highest effective energy x-rays in phantom. The dashed line indicates spectrum with the lowest in-phantom effective energy (55.92 keV), and the solid line indicates spectrum with highest in-phantom effective energy (56.28 keV).
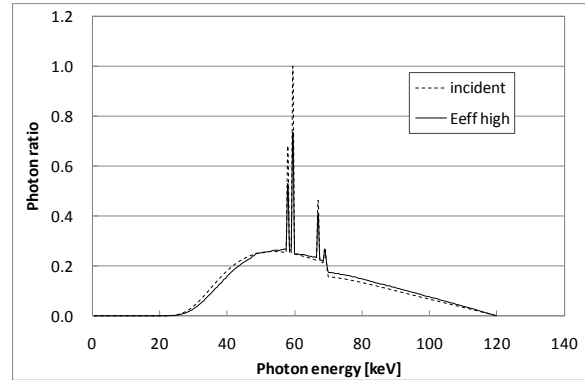

Figure 6. Comparison of spectrums of highest effective energy x-rays with the incident x-rays. The dashed line indicates incident x-ray spectrum with effective energy (54.0 keV), and the solid line indicates spectrum with the highest in-phantom effective energy (56.28 keV).
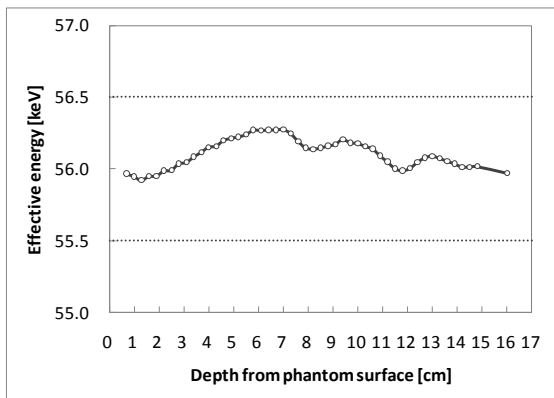

Figure 7. Change of in-phantom effective energy in each depth from the phantom surface.

Table 1. Summary of the calculated results.

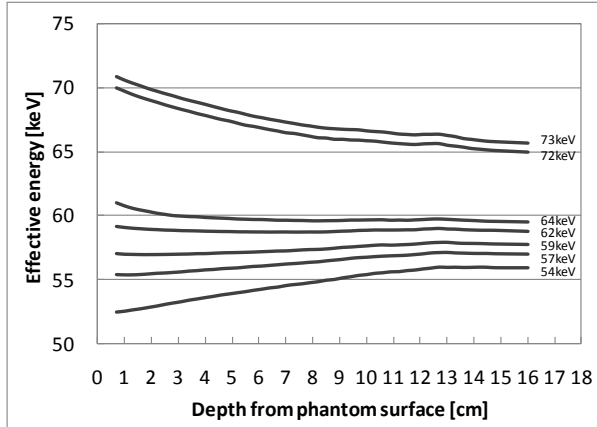| Depth from phantom surface	Effective energy	Difference for incident E$_{eff}$	
[cm]	[keV]	[keV]	[%]
0.0 (incident)	54.00	-	-
1.0	55.95	+ 1.95	+ 3.61
1.3	55.92(low)	+ 1.96	+ 3.56
7.0	56.28(high)	+ 2.15	+ 4.22
16.0	55.97	+ 1.97	+ 3.65

Figure 8. Changing of in-phantom effective energy in using single type of energy for the fan beam. Each energy value corresponding with solid lines is effective energy of incident x-ray spectrum, the dashed line is similar to the line showed in Fig.7.
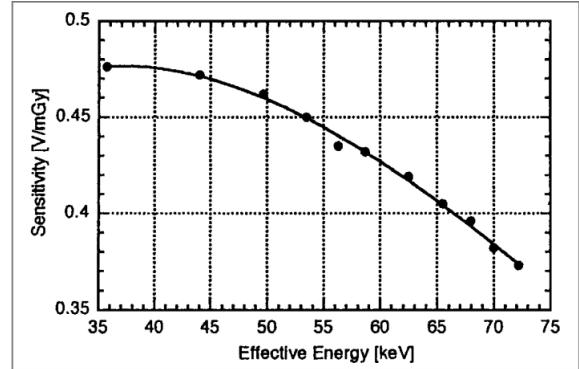

Figure 10. Energy dependence of semiconductor dosimeter (made by T Aoyama; Nagoya University 2002)[1].
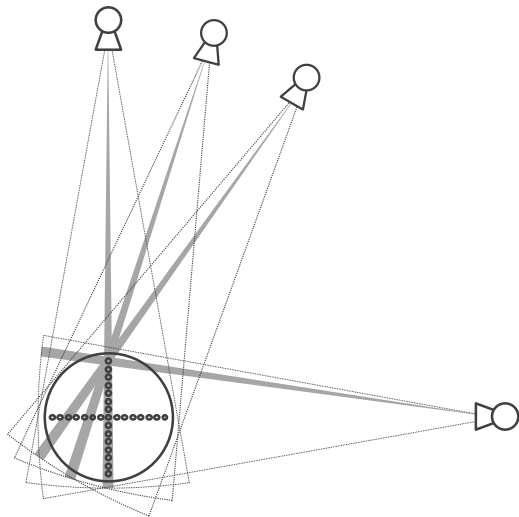

Figure 9. Photon counting part was projected in each rotating angle.

Table 2. Difference of sensitivity of semiconductor dosimeter for effective energy.

	Effective energy [keV]	Sensitivity [V/mGy]	Difference for incident E$_{eff}$ [V/mGy]	[%]
incident	54.00	0.448	-	-
in-phantom	55.92(low)	0.440	-0.008	-1.79
	56.28(high)	0.441	-0.007	-1.56